UNIVERSITÀ DEGLI STUDI DI PADOVA

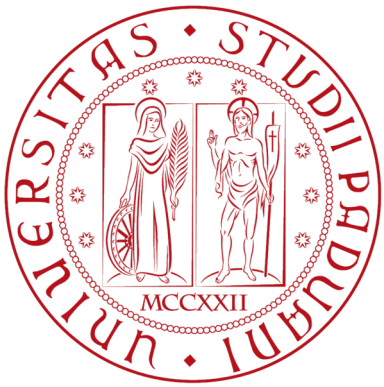

Dipartimento di Fisica e Astronomia
Corso di Laurea Magistrale in Astrophysics and Cosmology

ON THE RELATION BETWEEN MHD TURBULENCE AND ELECTRON ACCELERATION IN MAGNETIZED PLASMAS

Monia CALCAGNO
Matr. n. 2062890

Relatore: Giovanni CARRARO
Correlatore: Nicola VIANELLO

— ANNO ACCADEMICO 2023/2024 —

Abstract

The thesis investigates the process of electron acceleration in magnetized plasmas and its relation with electrostatic and magnetic turbulence. Electron acceleration is a mechanism observed both in laboratory and astrophysical plasmas, of whom some examples are the solar wind and the magnetosphere. The thesis initially offers an overview about the most relevant theoretical concepts regarding plasmas, magnetohydrodynamics, magnetic reconnection and turbulence, in addition to information about the devices which collected the data for the analysis, which are two complementary Reversed Field Pinch toroidal devices: TPE-1RM20, which gathers data with insertable probes combining magnetic coils and Electron Energy Analyzer (EEA), and RFX-mod which provides the time evolution of the parallel currents.

The electron acceleration phenomena consist in bursting events which emerge out of the time series of the signals, and they are likely to be associated with magnetic reconnection. First of all, the intermittent nature of these events has been confirmed, by verifying the non self-similar behaviour of the Probability Distribution Function of the magnetic fluctuations. The events responsible for the deviation from self-similarity have been selected using the Local Intermittency Measurement method. It is to be mentioned that TPE-1RM20 is particularly affected by an intense MHD activity at low frequency which affects the study of the spectrum in the higher frequency range, whereas RFX-mod is not limited from this point of view. The statistics have initially focused on the conditional average of single shots of signal which has provided the average fluctuating structure whose amplitude can be computed in relation to the scale. Later, the same analysis has been applied to multiple signals. The behaviour of the fluctuations of the EEA current and parallel current, of the magnetic and electric fields has been checked at the same instant of time, in order to detect any kind of possible correspondence. Successively, the waiting time distribution has been analyzed, in order to verify if it satisfied some particular relation with the frequency scale. The final step has been to prove the existence of a correlation between the minima present in the time trace of the reversal parameter indicating reconnection and the detected events. In the end, the proposed link between electron acceleration and magnetic reconnection is confirmed, as deduced by the associated magnetic fluctuations, whose shape is consistent with the typical structure of current sheets.

Contents

1 Introduction **2**

2 Preliminary concepts **4**

2.1 Magnetohydrodynamics and plasma theory 5

2.1.1 Fundamental equations and definitions 5

2.1.2 Magnetic confinement and RFP plasmas 9

2.2 Magnetic Reconnection 15

2.2.1 Theoretical description 15

2.2.2 Experimental evidence 18

2.2.3 RFP framework 23

2.3 Turbulence 28

3 Current experimental results and procedures **32**

3.1 Superthermal electron flows 32

3.2 MHD turbulence and intermittency 37

4 Data Analysis **46**

4.1 Diagnostics 46

4.1.1 TPE-1RM20 device 46

4.1.2 RFX-mod RFP device 49

4.2 Available data and signals 50

4.3 Data analysis and discussion 54

4.3.1 LIM method and probability distribution function 54

4.3.2 Conditional average sampling 57

4.3.3 Study of the distribution of the waiting times 70

4.3.4 Correlation with the reversal parameter 72

4.4 Results 77

5 Conclusion **78**

Chapter 1

Introduction

Humans are struggling to find new methods for energy production, efficient enough to sustain the current needs and affecting less the environment. Nuclear fusion is a very valuable option, since it is possible for us to replicate the reactions occurring in stellar interiors in laboratory plasmas which are magnetically confined. Analogously to what occurs in some astrophysical systems, also in experiments intermittent bursts of energy have been observed in the past years, and the cause is not currently completely understood, and it is plausible that it is related to phenomena involving the magnetic field and particle acceleration. It is a fact that magnetic fields permeate the universe, from the smaller scales, involving for example the solar corona or the magnetosphere, till the largest scales of the galactic magnetic fields and interstellar medium [89]. Such magnetic fields are turbulent and it is possible to study their dynamics with the Magnetohydrodynamic (MHD) theory. In particular, physical processes occur, like magnetic reconnection, which change the field lines topology and also cause a conversion of magnetic energy into thermal energy. So, studying the relation between the burst phenomena and magnetic reconnection is not only useful for laboratory purposes, but also to understand key processes involving a wide cut of the universe.

Therefore, this thesis proposes to study the electron acceleration in MHD turbulent plasmas and see how it is correlated to the magnetic field, focusing on the framework of laboratory plasmas to later understand more universal physical laws. Simultaneously to the electron acceleration, precise fluctuations of the magnetic field are expected. Inside Reversed Field Pinch plasmas, which are toroidal magnetic configurations where the field reverses at the edge, the magnetic field has a toroidal and poloidal component (see figure 2.2), and obeys to a very specific profile which changes from the core to the boundary region (as paragraph §2.1.2 will explain) and the detection of fast electrons is specifically localized in the edge region, which hosts the formation of poloidal current sheets, associated to a general increase of toroidal flux, which is typical for magnetic reconnection. The data analysis is based on these concepts and intends to provide further evidence of the simultaneous occurrence of these phenomena. To do so, a first analysis has been carried out on the data obtained with the RFP device TPE-1RM20 (described in §4.1.1) which is able to monitor effectively the electron current thanks to the Electron Energy Analyzer (EEA), which is also associated to a coil system, and provides signals in form of time series of various quantities, such as the plasma current, magnetic fields, electron potential, or reversal parameter (defined in 2.30). Then, the achieved statistical results

have been compared to those obtained out of the signals gathered with a complementary RFP device, RFX-mod (see §4.1.2), which on its turn is able to measure the parallel currents, and see how they vary in the same conditions (during reconnection phenomena) as in the case of TPE-1RM20. The analysis is performed at different temporal scales to verify the influence of macro and micro instabilities on the signals, and exploits advanced statistical tools as wavelet transforms, Probability Distribution Functions, Local Intermittency Measurement method, and waiting times distributions.

However, before starting with the out-and-out data analysis, chapters 2 and 3 follow hereafter with the aim to offer an overview exhaustive enough to build a basis to address all the topics involved in this work. The overview concerns the MHD theory, magnetic reconnection, turbulence (also in the MHD framework), and, finally, a dissertation about the diagnostics and operation of the two devices which gathered the data used in the analysis.

Chapter 2

Preliminary concepts

Nuclear fusion is a process occurring in the interiors of stars, when two positively charged nuclei come close to each other overcoming their Coulomb repulsion. If they are close enough the attractive strong nuclear force is able to bind them together. This can happen only if their kinetic energy is high enough, so thermonuclear reactions take place only at high temperatures and densities at whom the gas becomes ionized, namely in the state known as plasma. Hot plasmas cannot be contained inside ordinary material, which would be burnt for the very high temperature and density, nevertheless, if the plasma is not kept hot enough, the Brehmsstrahlung radiation emitted by the collisions between the particles increases, and so does the heat loss.

The fusion process involves the union of two light nuclei which form a heavier one. In stars the nuclear energy usually is produced by the fusion of four atoms of hydrogen forming a helium atom. An example is the proton-proton (PP) chain occurring in the Sun

$$6\,{}^{1}\mathbf{H}^{+} \rightarrow {}^{4}\mathbf{He}^{++} + 2\,{}^{1}\mathbf{H}^{+} + 2e^{+} + 2\nu + 2\gamma$$

with the following steps:

1. Two protons fuse and produce a deuterium atom and release an electron positron and neutrino
2. The deuterium atom reacts with a proton and produces an helium-3 nucleus and a gamma ray
3. The helium-3 nuclei fuse and produce an α particle (helium-4) and release two photons

Nuclear fusion is an exothermic process and so there is an energy release. This is generated by the the mass difference between the reactants and the products which corresponds to the binding energy of the nucleus, and according to the Einstein equation we have the conversion $\Delta E_{binding} = \Delta m c^2$. The PP chain, for example, liberates 26 MeV of energy.

The most promising fusion reaction in laboratory is the following [83]:

$$ {}^{2}_{1}\mathbf{D} + {}^{3}_{1}\mathbf{T} \rightarrow {}^{4}_{2}\mathbf{He} + {}^{1}_{0}\mathbf{n} \tag{2.1}$$

where D and T are deuterium and tritium. The reason concerns the cross section, which plays an important role being directly related to the occurrence of the collisions between the particles

causing the reaction. In the case of the D-T reaction, unlike other reactions such as D-D or D-He^3, the maximum value of the cross section is reached at energies (around 100 keV), which are feasible on the Earth. The energy release of this reaction is 17.59 MeV. The mixture D-T fuses at a temperature of $\sim$ 10 keV with the production rate of α particles:

$$\frac{\partial n_\alpha}{\partial t} = n_D n_T \langle \sigma_F v \rangle \tag{2.2}$$

where n stands for the densities and $\langle \sigma_F v \rangle$ is the fusion reaction rate averaged over the velocity distribution of the particles.

In order to get a sufficient amount of energy (i.e. the output energy must be larger than the input energy) the plasma needs to be confined long enough. The necessary condition for fusion ignition, which is defined as the moment when the power associated to alpha particles is greater than the energy losses, is given, for example, by the fusion triple product [83]:

$$n\tau_E T > 5 \cdot 10^{21} m^{-3} skeV \tag{2.3}$$

where n is the number density of both the ion and electron particles and τ_E is the energy confinement time. According to the usual values for the temperature (8-18 keV) and density ($10^{20}\mathrm{m}^{-3}$), this time scale is of the order of 2-6 s.

2.1 Magnetohydrodynamics and plasma theory

In the following paragraphs the principal concepts of plasma theory and physical laws will be treated, and then the process of magnetic confinement will be discussed, with particular attention to the Reversed Field Pinch configuration, whose dynamics strongly depend on the magnetic reconnection.

2.1.1 Fundamental equations and definitions

A plasma is a collection of neutral and charged particles (electrons and ions) characterized by long range electromagnetic interactions and complex trajectories. Such a ionized gas is globally neutral and it is described by collective properties. In particular, a plasma can be treated as a single fluid, and this model is known as single fluid magnetohydrodynamics (MHD), if it can be assumed that the charge separation is negligible, which happens when considering time scales larger than the inverse of the plasma frequency and length scales larger than the Debye length [14]. The plasma frequency corresponds to the frequency of the wave sustained by the electron fluid (in the case of a uniform homogeneous plasma) as a response to an electromagnetic perturbation:

$$\omega_p^2 = \frac{4\pi n_0 e^2}{m_e} \tag{2.4}$$

with n_0 being the unperturbed number density of the electron fluid. The Debye length is the typical distance over which the electrostatic potential induced by the charge imbalance is screened:

$$\lambda_D = (\frac{k_B T}{8\pi n e^2})^2 \tag{2.5}$$

with n the particle number density and k_B the Boltzmann constant. The solution for the screened potential is:

$$\phi = Q\frac{exp(-r/\lambda_D)}{r}$$

where Q is the potential around a charge. Therefore, since in the MHD regime we consider spatial scales larger than the Debye length, the plasma can be considered charge-neutral because the charge effect is screened: this is a common situation both in laboratory and astrophysical plasmas, where the ratio between the mean free path of the particles and the Debye length is often very large.

The number of particles involved in a simultaneous interaction is $n\lambda_D^3$, and the plasma parameter g can be defined as the inverse of this number:

$$g = \frac{1}{n\lambda_D^3} = \frac{(8\pi)^{3/2}e^3 n^{1/2}}{(k_B T)^{3/2}}, \tag{2.6}$$

and it indicates the competition between the electrostatic interactions and the thermal motion of the particles inside the plasma: if g is small enough, the plasma particles can be considered as non-interacting. Equation 2.6 shows that in low-density plasmas, $g \propto n^{1/2}$ is low too, namely the interactions among particles are weak as mentioned above, but the number of particles interacting collectively $n\lambda_D^3$ is larger. Conversely, if the density is higher, the plasma can be treated as an highly conductive fluid, because the interactions are strong, even if there are only a few particles involved in a simultaneous interaction.

In order to build a single fluid model the following density and velocity are defined:

$$\rho = n(m_i + m_e) \tag{2.7}$$

$$\mathbf{v} = \frac{m_i\mathbf{v}_i + m_e\mathbf{v}_e}{m_i + m_e} \tag{2.8}$$

where the masses and velocities of the ions and electrons are distinguished with a subscript. Starting from the separated equations of motion for the two types of particles, it can be shown [14] that the Ohm's law is obtained:

$$\mathbf{j} = \sigma(\mathbf{E} + \frac{\mathbf{v}}{c} \times \mathbf{B}) \tag{2.9}$$

with σ being the electric conductivity equal to the inverse of the electrical resistivity of the plasma

$$\eta \approx \frac{\pi m_e^{1/2} e^2}{(k_B T)^{3/2}}$$

This simplified version of the generalized Ohm's law [14] shows how the current density $\mathbf{j}$ is related to the electromagnetic fields.

The MHD equations are the following:

$$\frac{\partial \rho}{\partial t} + \nabla(\rho\mathbf{v}) = 0 \tag{2.10}$$

$$\frac{\partial \mathbf{v}}{\partial t} + (\mathbf{v}\cdot\nabla)\mathbf{v} = \mathbf{F} - \frac{1}{\rho}\nabla p + \frac{1}{4\pi\rho}(\nabla \times \mathbf{B}) \times \mathbf{B} + \nu\nabla^2\mathbf{v} \tag{2.11}$$

with $\mathbf{F}$ being the term containing all the external forces, and ν the kinematic viscosity. 2.10 and 2.11 are respectively the continuity and Navier-Stockes equations. In the latter the magnetic body force term $\frac{1}{4\pi\rho}(\nabla \times \mathbf{B}) \times \mathbf{B}$ was added to the hydrodynamic version and it can be seen [14] that it introduces an isotropic pressure term $B^2/8\pi$, plus a tension along the magnetic field lines $-B^2/4\pi$. In addition to these equations an energy equation is not needed because compressibility is assumed to be negligible. Finally, we need an equation for the time evolution of the magnetic field. By combining the Maxwell equation

$$\frac{\partial \mathbf{B}}{\partial t} = -c\nabla \times \mathbf{E}$$

and the 2.9, the induction equation is obtained:

$$\frac{\partial \mathbf{B}}{\partial t} = \nabla \times (\mathbf{v} \times \mathbf{B}) + \lambda \nabla^2 \mathbf{B} \tag{2.12}$$

with $\lambda = \frac{c^2}{4\pi\sigma}$ being the magnetic diffusivity. Starting from this equation and dividing the two terms we can define the magnetic Reynolds number

$$\mathcal{R}_M = \frac{LV}{\lambda} \tag{2.13}$$

where L is the length scale of the system, and V the typical velocity. A particular case of the magnetic Reynolds number is the Lundquist number:

$$S = \frac{Lv_A}{\lambda} \tag{2.14}$$

where v_A is the Alfvén velocity [14]

$$\mathbf{v}_A = \frac{\mathbf{B}_0}{\sqrt{4\pi\rho_0}} \tag{2.15}$$

of the typical homonymous perturbations which move along the magnetic field lines (where $\mathbf{B}_0$ and ρ_0 are the unperturbed magnetic field and density).

In the induction equation 2.12 we can distinguish two regimes. When $\mathcal{R}_M$ is low, the diffusion term $\lambda\nabla^2\mathbf{B}$ is dominant and it indicates that a magnetic field in a laboratory plasma decays due to Ohmic dissipation, if not maintained by driving some external currents. However, at high $\mathcal{R}_M$ the term $\nabla \times (\mathbf{v} \times \mathbf{B})$ in 2.12 becomes the most important, and it implies that:

$$\frac{d}{dt}\int_S \mathbf{B} \cdot d\mathbf{S} = 0 \tag{2.16}$$

which means that in a condition of zero resistivity (so at infinite conductivity), called ideal MHD limit (typical for astrophysical plasmas, for example), the magnetic field is frozen in the plasma, i.e. it is forced to move together with the plasma flows: this is called flux freezing. As a consequence, if a plasma column is bent or twisted, also the magnetic field lines going through it will be modified in the same way. In particular, if two fluid elements are connected by a magnetic field line, they will remain connected by the same line.

A plasma column may be subjected to instabilities, either due to an enhancement of the magnetic pressure or an increase of the magnetic stress $\frac{1}{4\pi}(\nabla \times \mathbf{B}) \times \mathbf{B}$. However, if there is a magnetic field line flowing along the axis of the plasma column, it tends to suppress these

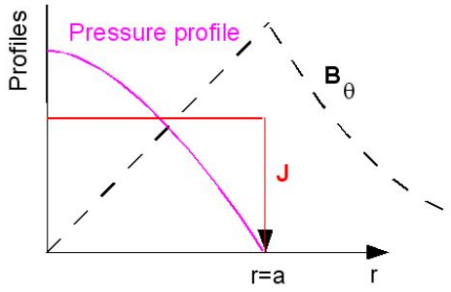

Figure 2.1: Radial profile of the pressure p, azimuthal component of the magnetic field B_θ, and current density $\mathbf{j}$ due to the pinch effect. Image credits: https://images.app.goo.gl/NrngRpjcrDCvnb57A

kinds of instabilities acting oppositely to them [14], making the plasma column stable.

An important parameter is the plasma-β which corresponds to the ratio between the gas pressure and the magnetic pressure:

$$\beta = \frac{p}{B^2/8\pi} \tag{2.17}$$

Interesting is the case of magnetohydrostatics, where the static version of the 2.11 is used. In the particular case of the pressure-balanced field the external forces are negligible, and we have equilibrium between the pressure and the magnetic stresses:

$$\nabla p = \frac{1}{4\pi}(\nabla \times \mathbf{B}) \times \mathbf{B} \tag{2.18}$$

Let us use the cylindrical coordinates and assume there is symmetry, such that nothing varies in θ and z coordinates, but only in the radial direction r. Since $\nabla \mathbf{B} = 0$ we have:

$$\mathbf{B} = B_\theta(r)\hat{\mathbf{e}}_\theta + B_z(r)\hat{\mathbf{e}}_z \tag{2.19}$$

Substituting it in 2.18 we obtain:

$$\frac{d}{dr}(p + \frac{{B_\theta}^2 + {B_z}^2}{8\pi} + \frac{{B_\theta}^2}{4\pi r}) = 0 \tag{2.20}$$

If now we consider a plasma column in which a magnetic field line is produced by driving a constant current $\mathbf{j} = j(r)\hat{\mathbf{e}}_z$ along the column axis, no B_z component will be produced and it can be shown [14] that the azimuthal component of the magnetic field is:

$$B_\theta = \frac{2\pi}{c} jr$$

We obtain the following profile for the pressure:

$$\frac{dp}{dr} = -\frac{2\pi}{c^2} j^2 r \tag{2.21}$$

which gives $p = p_0 - \frac{\pi j^2 r^2}{c^2}$, where p_0 is the pressure at the centre of the column. So it can be seen that, while B_θ grows linearly with r, the pressure decreases with the radius as an effect of the magnetic field, known as pinch effect. This is shown in figure 2.1: there is a radius at

which the pressure goes to zero, and after whom it would acquire a negative value, which is impossible. That is how the magnetic field is able to confine a plasma column. The value of the current I necessary for the pinch effect can be computed knowing the average pressure $\bar{p}$ and the radius of the plasma column a [14]:

$$\bar{p} = \frac{I^2}{2\pi c^2 a^2} \tag{2.22}$$

This suggests that a way to keep the plasma confined by the magnetic field consists in the cylindrical magnetohydrostatic configurations.

2.1.2 Magnetic confinement and RFP plasmas

The magnetic confinement of a plasma is possible thanks to the Lorentz force, which is the force acting on a charged particle moving in an electromagnetic field. If the particle has mass m and charge q, its equation of motion is:

$$m\frac{d\mathbf{u}}{dt} = q(\mathbf{E} + \frac{\mathbf{u}}{c} \times \mathbf{B}) \tag{2.23}$$

If, in a uniform magnetic field $\mathbf{B}$, the particle moves with perpendicular velocity $\mathbf{u}_\perp$ with respect to the magnetic field, then the equation of motion becomes:

$$m\frac{d\mathbf{u}_\perp}{dt} = \frac{q}{c}\mathbf{u}_\perp \times \mathbf{B} \tag{2.24}$$

So, it results that the particle makes circular orbits in the plane perpendicular to $\mathbf{B}$ with a frequency (called cyclotron frequency) equal to

$$\omega_c = \frac{|q|B}{mc}$$

and radius

$$r_L = \frac{mv}{|q|B}$$

called Larmor radius. The magnetic field instead does not affect the parallel component $\mathbf{u}_\parallel$, so that the motion of the particle becomes helical because it is composed also of a uniform translation.

Particles moving in an open trajectory are not well confined, so that a geometrical configuration with closed lines such as the torus is needed. The geometry of the toroidal configuration, visible in figure 2.2, can be properly described by the following coordinates:

1. The major radius R which covers the distance from the origin of the coordinate system to the centre of the section of the torus
2. The minor radius r from the centre of the section of the torus at $r=0$ to its boundary at $r=a$
3. The poloidal angle θ for the short loop of the torus section
4. The toroidal angle ϕ with respect to the central axis of the torus

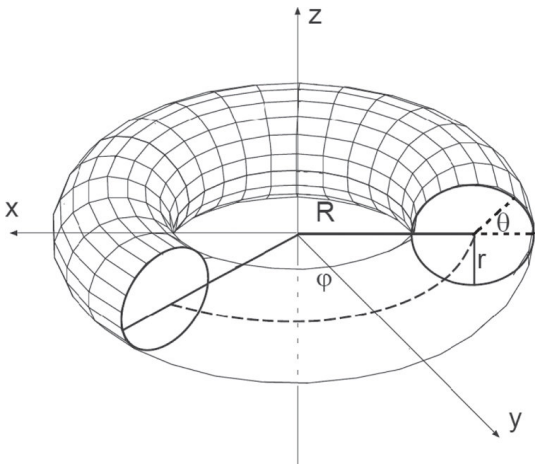

Figure 2.2: Geometry of the toroidal configuration. Image credits: [37]

The aspect ratio is defined as the ratio between the major radius R and the minor radius a.

The Reversed Field Pinch (RFP) is a toroidal axisymmetric configuration in which the plasma is confined by a poloidal magnetic field created by a toroidal plasma current and by a toroidal field created internally and externally [89]. These plasmas are in a force-free magnetic equilibrium with a magnetic field which decreases monotonically with the minor radius and it reverses its direction at the plasma edge [92]. They are also characterized by an ongoing dynamo[1] process which produces the mandatory magnetic field flux needed to sustain the configuration. This consists in a cyclical relaxation mechanism which allows for the maintenance of this configuration for a time longer than the resistive diffusion time (see equation 2.12).

In particular, let us first introduce the magnetic helicity: a measure of the "knottedness" and the "twistedness" of a magnetic field [89], defined as [14]

$$\mathcal{H} = \int \mathbf{A} \cdot \mathbf{B}\, d\mathbf{V} \tag{2.25}$$

where $\mathbf{A}$ is the vector potential ($\mathbf{B} = \nabla \times \mathbf{A}$). According to Taylor's theory of plasma relaxation, in a low-β plasma the magnetic helicity is constant during a relaxation process, while the magnetic energy reaches its minimum value. This can be demonstrated making a Fourier decomposition of the vector potential

$$\mathbf{A(x)} = \frac{1}{(2\pi)^{3/2}} \int \tilde{\mathbf{A}}(\mathbf{k}) exp(i\mathbf{k} \cdot \mathbf{x})\, d^3k$$

and it can be shown [14] that the magnetic energy spectrum roughly goes as $W \approx k^2 \tilde{A}^2(\mathbf{k})$, while the spectrum of the magnetic helicity goes as $\mathcal{H} \approx k\tilde{A}^2(\mathbf{k})$. So the higher wavenumbers have a larger weight on the magnetic energy. This is valid in case of dissipation, so when short spatial scales are considered: the resistive diffusion term in 2.12 increases in those regions where the magnetic field lines approach each other characterized by sharper gradients of the magnetic

[1] A general definition of the so-called *Dynamo process* consists in the process which creates and sustains the large scale structures and magnetic fields of the universe: tiny magnetic fields (produced by statistical fluctuations of plasmas) give rise to large-scale magnetic structures [14].

field (such as current sheets, defined later), and consequently the higher wavenumber modes, dominant in these narrow regions, are more affected by it. The minimum of the magnetic energy can be computed in the case of a system in which the magnetic helicity remains a constant, and the solution [14] is given by:

$$\delta W - \frac{\mu}{8\pi}\delta\mathcal{H} = 0 \tag{2.26}$$

with $\frac{\mu}{8\pi}$ being the Lagrange multiplier. In order to satisfy this condition, we obtain:

$$\mathbf{B} = \mu\mathbf{A}$$

whose curl is

$$\nabla \times \mathbf{B} = \mu\mathbf{B} \tag{2.27}$$

with μ being a spatial constant along and across magnetic field lines [89]. This is the so-called linear force-free field case: the gas pressure is negligible with respect to the magnetic pressure (low β) and, since the magnetic stress cannot be balanced by it, the magnetic field reorganizes itself in such a way to eliminate this stress by itself.

Let us suppose in a cylindrical column of plasma a current I is driven along the axis. The current will lead to the production of a magnetic field component along the θ direction, and, for the plasma column to be stable, it will be necessary to set up also a magnetic field $\bar{B}$ along the axis sending some currents using the external coils. After this perturbation, the plasma will go through relaxation. The pinch parameter Θ can be defined [14]:

$$\Theta = \frac{2I}{ca\bar{B}} \tag{2.28}$$

and it is experimentally proven that at a critical value of Θ the z component of the magnetic field B_z reverses its direction with respect to the input field ($\bar{B}$) one. This is how the RFP configuration is generated. In the limit of large aspect ratios the cylindrical geometry is a good approximation for the toroidal geometry, with the coordinate $z = R\phi$, and any generic function F will satisfy [82]:

$$F(r, \theta, z) = F(r, \theta, z + 2\pi R)$$

The solution to equation 2.27 is given using the Bessel function model:

$$B_z = B_0 J_0(\mu r)$$

$$B_\theta = B_0 J_1(\mu r)$$

$$B_r = 0$$

and the reversal is satisfied for $\mu a > 2.405$. Since the magnetic field is force free, it is completely characterized by the uniform parallel current density at uniform pressure. In fact, an analytical expression for the lagrange invariant parameter μ is [82]:

$$\mu = \mu_0 \frac{\mathbf{j} \cdot \mathbf{B}}{B^2} = \frac{\mu_0 j_\parallel}{B}$$

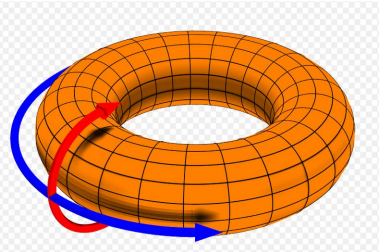

Figure 2.3: Diagram of a toroidal configuration to visualize the poloidal (red) and toroidal (blue) direction, described respectively by the angles θ and ϕ. Image credits: By DaveBurke - Own work, CC BY 2.5, `https://commons.wikimedia.org/w/index.php?curid=1169843`

In particular, if we define

$$\langle B_\phi \rangle = \frac{1}{\pi a^2} \int_0^a B_\phi 2\pi r \, dr$$

Θ (introduced in equation 2.28) can also be written as

$$\Theta = \frac{B_\theta(a)}{\langle B_\phi \rangle}, \tag{2.29}$$

and another key parameter can be defined, the reversal parameter

$$F = \frac{B_\phi(a)}{\langle B_\phi \rangle} \tag{2.30}$$

so we obtain [14]:

$$F = \frac{\mu a}{2} \frac{J_0(\mu a)}{J_1(\mu a)} = \frac{B_z(r=a)}{\bar{B}} \tag{2.31}$$

which, practically, corresponds to the ratio between the magnetic field component B_z at the outer edge (r=a) with respect to its average value, while Θ results to be:

$$\Theta = \frac{\mu a}{2} \tag{2.32}$$

This expression can be obtained also from 2.28 substituting for μ, and its theoretical critical value corresponds to 1.2, which is the value beyond which the field reversal is possible. This, however, is only in partial agreement with the experimental values, both because the radial profile of μ, for example, decreases towards the edge, and there exists a non-zero pressure gradient which does not allow for a complete force-free configuration [82]. There are some more precise equilibrium models (such as MPFM [70] or "μ& P" [60]) which introduce a perpendicular component for the current density in order to account for the presence of the pressure gradient.

The stability of a toroidal configuration is controlled using a parameter called safety factor [27]:

$$q(r) = \frac{r}{R} \frac{B_\phi(r)}{B_\theta(r)} \tag{2.33}$$

which corresponds to the number of poloidal turns for a single toroidal turn of field line [82] (see fig. 2.3 to visualize the two directions). In the RFP the poloidal and toroidal components

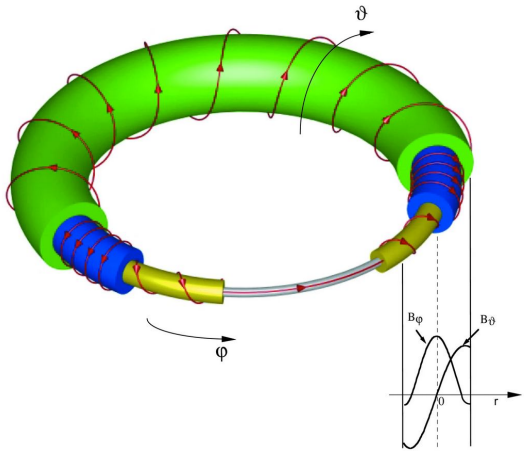

Figure 2.4: Toroidal confinement of the magnetic field in a RFP plasma. Both the spiral can be observed changing its polarity at different surfaces, and the magnetic field profile (toroidal and poloidal component) in the plasma region away from the axis. Image credits: `https://www.igi.cnr.it/en/research/magnetic-confinement-research-in-padova/rfp-configuration/`

of the magnetic field are of comparable magnitude, and the safety factor is characterized by a precise spatial profile which decreases from the inner (where $q(0) << 1$) to the outer regions [56]: the magnetic field lines are almost toroidal in the core, and poloidal at the edge. In fact, they extend only toroidally on the plasma axis, while they extend both toroidally and poloidally in the core plasma region, away from the axis. Therefore the configuration consists in a spiral around the axis, which changes its polarity at the radius where the external region of the plasma begins. This can be better visualized in figure 2.4

As already mentioned, when a plasma is perturbed the magnetic field line is also bent, and the plasma reacts elastically to that instability. However, this stabilizing effect vanishes on the surface where the wavefront of the perturbation is parallel to the magnetic field, which means for

$$\mathbf{k} \cdot \mathbf{B} = 0$$

which in cylindrical coordinates corresponds to:

$$\frac{m}{r} B_\theta + \frac{n}{R} B_\phi = 0 \tag{2.34}$$

where m and n are defined as the poloidal and toroidal wavenumbers. This leads to the expression:

$$|q(r)| = \frac{m}{n} \tag{2.35}$$

Two new definitions are now introduced:

1. The rational surfaces are all those surfaces satisfying $|q(r)| = \frac{m}{n}$
2. The resonant modes are the instabilities given by an (m,n) pair for which $|q(r)| = \frac{m}{n}$ is satisfied

The value of q on axis for a typical discharge in a RFP configuration is smaller than 1: this is fundamental for the dynamics of the reversal condition because it allows for the destabilization

of all the $(m = 1, n > n_0)$ modes, where $n_0 \approx 2R_0/a$ is the inner resonant mode [82]. In particular, the reversal surface is the rational surface where the toroidal magnetic field cancels out, and it corresponds to the limit which separates the central 'core' region from the external one. This surface is unstable to the $m = 0$ modes. We also define the magnetic shear, another important parameter which measures the variation of the field-line inclination [5]:

$$s(r) = \frac{r}{q(r)} \frac{dq(r)}{dr} \tag{2.36}$$

It has a stabilizing effect for the MHD instabilities [27].

The RFP configuration turns out to be very turbulent, since it generates a spectrum characterized by a large amount of MHD modes, and the specific behaviour of the q profile causes the growth of many MHD instabilities: looking at equation 2.35 it can be seen how the q profile presents a large number of resonant modes, resulting as unstable modes composing a large spectrum. Nevertheless, the big advantage is that the RFP configuration is able to reach high values of β and plasma current, and consequently the ignition condition can be achieved thanks to ohmical heating only.

2.2 Magnetic Reconnection

Magnetic reconnection is a very widespread process in the Universe, occurring during phenomena concerning both the magnetized astrophysical plasmas, such as the evolution of solar flares, coronal mass ejection, or interaction of solar winds with the Earth magnetosphere, and laboratory plasmas: in the example of RFP plasmas it occurs during relaxation processes. In principle it consists in the rearrangement of the magnetic field lines configuration by reorganizing macroscopic quantities of plasmas like flows and thermal energy [89].

2.2.1 Theoretical description

In the limit of ideal MHD, as already explained previously with equation 2.16, the magnetic field is completely frozen in the plasma, and if there are two points which are connected by a magnetic field line, they will always be. The field lines frozen in the fluid can be considered as flux tubes of infinitesimal diameter [5]. In these conditions, in addition to the conservation of the magnetic flux, there is also the conservation of magnetic helicity (defined in 2.25), as explained in paragraph §2.1.2. The conservation of both quantities is directly associated with the conservation of the so-called *magnetic topology*, which can be defined as the orientation, linkage and knottedness of the field lines [5]. Basically, magnetic reconnection involves a modification of the magnetic topology leading to a new equilibrium configuration. The condition for the conservation of magnetic topology can be expressed in the following way [5]:

$$\partial_t \mathbf{B} + \mathbf{u}\nabla\mathbf{B} - \mathbf{B}\nabla\mathbf{u} = \sigma\mathbf{B} \tag{2.37}$$

where $\mathbf{B}$ has the dimensions of a velocity, namely the Alfvén velocity $\mathbf{v_A} = \mathbf{B}/\sqrt{4\pi\rho}$, with ρ being the mass density, $\mathbf{u}(\mathbf{x},t)$ is the flow which causes the transport of the field, and σ is an arbitrary function of space and time: the evolution of a magnetic field $\mathbf{B}(\mathbf{x},t)$ is possible if this equation is satisfied. It can be shown that it corresponds to the expression:

$$\partial_t \mathbf{B} - \nabla \times (\mathbf{u} \times \mathbf{B}) = \mathbf{B}(\sigma - \nabla\mathbf{u}) \tag{2.38}$$

where $\nabla\mathbf{B} = 0$ implies:

$$\mathbf{B}\nabla(\sigma - \nabla\mathbf{u}) = 0 \tag{2.39}$$

Now, substituting Faraday's law $\partial_t\mathbf{B} = -c\nabla \times \mathbf{E}$ in equation 2.38, we obtain:

$$\mathbf{E} + \mathbf{u} \times \mathbf{B} = \mathbf{S} \tag{2.40}$$

where

$$\nabla \times \mathbf{S} = \mathbf{B}(\sigma - \nabla\mathbf{u}) \tag{2.41}$$

Therefore, flows $\mathbf{v}$ such that $\nabla\mathbf{v} = \sigma$, i.e. flows satisfying Ohm's law, also conserve magnetic topology. Qualitatively, two magnetic configurations are defined as topologically equivalent if no cutting or pasting of field lines is necessary to pass from one to the other. In particular, if the two configurations of magnetic field lines are such that one of them can be deformed through continuous transformations to obtain the other, then these configurations are said to have the same magnetic topology [14]. Thus, in an ideal magnetofluid (having resistivity

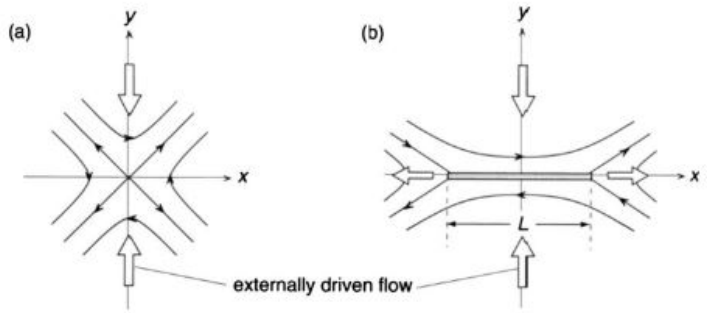

Figure 2.5: Diagrams showing the formation of a current density sheet (b), starting from a neutral X-point (a). The current sheet (b) is caused by the local effect of the magnetic field resistivity. It can be seen that there are magnetic field lines directed in opposite directions above and below the central region. Image credits: [89].

equal to zero), the magnetic topology can never change, and the fluid evolves through different successive configurations characterized by the same topology. At low β-values, such a system is in equilibrium only in the case of the force-free field, defined in 2.27.

Let us introduce the concept of magnetic reconnection starting from the traditional 2D system [5]: the magnetic field lines can be defined as the contour lines of a flux function ψ, i.e. $\psi = const.$ This is derived from the condition $\nabla\mathbf{B} = 0$ which implies:

$$\mathbf{B} = \mathbf{h}\times\nabla\psi + \mathbf{h}f = \mathbf{B}_p + \mathbf{B}_t \tag{2.42}$$

with $\mathbf{h}$ a vector in the symmetry direction, and $\mathbf{B}_p, \mathbf{B}_t$ the poloidal and toroidal components of the magnetic field. Magnetic reconnection is the process whereby the plasma flows across a surface separating regions of topologically different field lines [79]. Such a surface is called separatrix, where different lines join in a X-type neutral point. Outside the 2D case though, no separatrix surface can be identified, because it is not possible to disentangle lines with different topology. Therefore in 3D case, we refer to such points as those where $\mathbf{B} = 0$, which are stable and isolated, and divide space into regions of topologically different field lines. However, reconnection is rarely associated to null points, but rather characterized by sheet-like structures of current density at finite magnetic field. Therefore, the efficient way is to identify reconnection as a violation of the conservation of magnetic topology, namely if some points on a fluid line end up on a different one [68].

As just mentioned above, magnetic reconnection occurs in correspondence of current sheets, which are sheet-like tangential (i.e. aligned with the magnetic field) field discontinuities. In presence of finite resistivity (resistive MHD), although very small, further terms in the MHD equations defined in section §2.1.1 might become relevant: in the Navier-Stockes equation (2.11), the viscosity term $\nu\nabla^2\mathbf{v}$ may become important, and the same applies to the induction equation (2.12) because the resistivity term $\lambda\nabla^2\mathbf{B}$ appears. These terms cannot be neglected when considering a boundary layer characterized by large gradients of both velocity and magnetic field, such as currents sheets, where reconnection occurs. In a toroidal plasma column, they are generated on resonant surfaces (where, as explained in paragraph §2.1.2 the safety factor 2.33 is a rational number). In figure 2.5 the formation of a current sheet is shown after

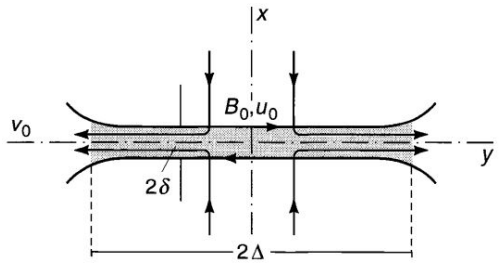

Figure 2.6: Scheme of the Sweet-Parker sheet. Image credits: [5]

the collapse of the magnetic field near an X-type neutral point (shown in 2.5a). It is to keep in mind that the initial X-point configuration is not essential, but, if present, the flow stagnates there with consequent flattening of the configuration and sheet formation [5].

During the thinning of the sheet the growth of the current density saturates because the magnetic flux transport into the sheet is balanced by field diffusion caused by finite resistivity. This leads to the formation of the Sweet-Parker sheet [62], a quasi-stationary resistive current sheet: the magnetic flux is led into the sheet, it is reconnected, and then swept out of the sheet. This process can be visualized in figure 2.5b: the magnetic field lines above and below are flowing towards the central region of the current sheet, and the plasma flow is represented by the big arrows which depict the inward velocity. The central parts of the magnetic field lines near the central region decay (where resistivity is enhanced), while the external parts constitute new lines which are accordingly attracted towards the inner region. Furthermore, the plasma from above and below exerts a pressure against the central region, while consequently the plasma inside the central region is squeezed out sideways [14], whose outflow is represented by the big arrows on the left and on the right in the figure. It is to be emphasized that this happens in small plasma-β regime, in which the magnetic pressure has a crucial impact.

The stationary state depends on the (poloidal) magnetic field B_0 immediately outside the current sheet, the upstream flow u_0 perpendicular to the field, the downstream flow v_0 along the field at the sheet edge, the sheet length Λ and width δ, and the diffusion coefficient ($\lambda = \frac{c^2}{4\pi\sigma}$). This type of configuration can be visualized in figure 2.6, and it can be shown [5] that the equation of force balance across the sheet is $\partial_x(p + \frac{1}{2}B^2) = 0$, so that:

$$\frac{1}{2}B_0^2 = p_{max} - p_0 \tag{2.43}$$

where p_{max} is maximum pressure in the centre of the sheet (where the poloidal field is zero) and p_0 is the upstream fluid pressure. If now the force balance is considered in correspondence of the mid-plane of the sheet (shown in figure 2.6), B_x (so the magnetic force) is negligible and only the pressure force contributes on the acceleration of the fluid along the sheet. As a consequence, we have

$$\frac{1}{2}v_0^2 = p_{max} - p_0 \tag{2.44}$$

which implies that $v_0 = B_0$, meaning that the downstream flow velocity is equal to the Alfvén speed. The reconnection rate can be defined using the Mach number[2] as $M_0 = S_0^{-1/2}$, with S_0

[2]The Mach number corresponds to $M_0 = \frac{u_0}{v_A}$, with v_A the Alfvén speed and u_0 the upstream flow.

the global Lundquist number (2.14). In other words, the incoming velocity gives an estimate for the reconnection rate (Sweet-Parker reconnection rate) which corresponds to [14]:

$$v_i \approx \frac{v_A}{\sqrt{\mathcal{R}_M}}$$

However, it is necessary to say that in the cases where S is very large (for example $S \sim 10^{10}$ in the solar corona), the Sweet-Parker rate actually implies reconnection times much longer than observed. Therefore, more accurate theories and models for current sheets have been later developed: some examples are Syrovatskii's theory [76] which puts together the concept of sheet singularities and ideal MHD, or Petschek's model [63] with the aim to explain the faster timescales observed in space.

The central positive part of a current sheet can be modelled, and its profile results to be a gaussian or a $\mathrm{sech}^2 x$ function [5]. Its internal structure depends mostly on the flow dynamics. The stationary Sweet-Parker model of the current sheet assumes that the small region where the reconnection process is localized has a scale $L < \Lambda$, the system scale. Since the global system (and so the boundary conditions exerted on the subsystem) changes in a timescale $\sim \Lambda/v_A$ whereas the small region changes in a timescale $\sim L/v_A$, the latter can be considered stationary. The small region of the current sheet where resistivity is important is the so-called diffusion region, and it is surrounded by an external region where resistivity is negligible. In the internal regions (in the case of low-resistivity plasmas), the cutting or pasting of the magnetic field lines can occur, while outside the magnetic field is still frozen with the plasma, so the current sheets are the only regions where the magnetic topology is not preserved.

2.2.2 Experimental evidence

Despite the theoretical model illustrated above, it has actually been observed that magnetic reconnection occurs whenever the magnetic field needs to release the excessive energy which has been stored [89], rather than simply occurring in correspondence of well localized regions, like current sheets. More exactly, the process starts with an external force impinging on the system which recovers a new MHD equilibrium by forming current sheets, driving magnetic reconnection, and changing topology. During the process, magnetic energy is converted into kinetic energy causing shocks and viscous dissipation which in turn convert kinetic energy into radiation and lead to the acceleration and heating of charged particles [89]. The energy conversion rate from magnetic to thermal energy results to be much larger than expected from classical dissipation mechanisms. These acceleration processes have been observed both in astrophysical plasmas and laboratory experiments. From the astrophysical point of view, magnetic reconnection has been observed with space satellites which provide high resolution data, and the following is a list of the examples that will be briefly discussed for different types of plasmas [89]:

1. Low β plasmas: solar flares, Earth magnetosphere, and magnetospheres of compact objects;

2. Large β plasmas: the interstellar medium (where actually $\beta \sim 1$), and accretion disks.

Conversely, laboratory fusion experiments recognize reconnection as self-organization phenom-

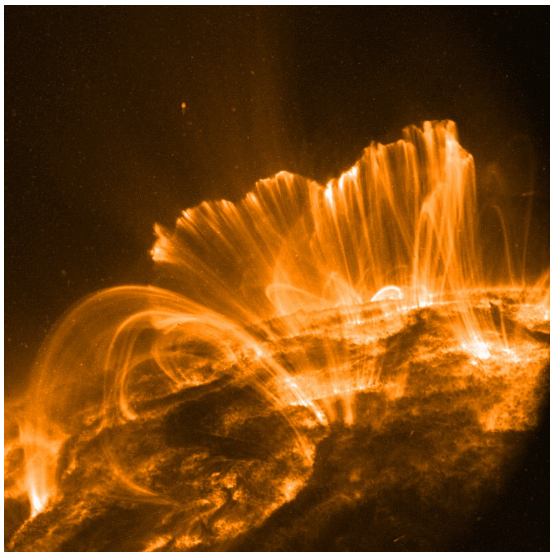

Figure 2.7: Image of a solar flare at 171 Å. Credits: apod.nasa.gov

ena of their configuration: the reconnection region is covered by a large number of points which measure the key plasma parameters [89]. Reconnection evidence will be discussed not only in RFPs, but also in another type of fusion plasmas: tokamaks.

The first example of an astrophysical plasma in which reconnection has been observed is the solar corona. The phenomenon is particularly visible when observing solar flares (illustrated in figure 2.7) in the soft X-rays, characterized by very fast timescales of the topology change of the order of minutes or hours [61] [15]. Magnetic reconnection is thought to be the source of the coronal heating mechanism, as well as being related to Coronal Mass Ejections (CMEs) [78], which are large-scale ejections of mass and magnetic flux from the corona to the interplanetary space [89]. CMEs are likely to be produced after the loss of equilibrium of the coronal plasma magnetic structures which causes a rapid change of the topology. The ejection liberates $\sim 10^{15}$ Wb of flux and 10^{13} kg of plasma [4]. The ejected mass brings along magnetic field lines in magnetic loops out of the solar surface, and the field lines start reconnecting in correspondence of an X point. Eventually, the particles channeled by reconnection in the field lines emit radiation [53]. The evolution of the magnetic arcades has been numerically simulated with a 2D flux-rope model [46] which demonstrated that the equilibrium changes state through the formation of a current sheet in the solar atmosphere. In particular, the proof of particle acceleration processes related to reconnection events is given by the observed hard X-ray emissions resulting as impulsive flares [89]. The energies involved are in the order of GeV for the ions, and 100 MeV for the electrons, measured during solar flares [40], and the resulting spectra present a power-law trend. The estimated total energy related to the particles can reach 50 percent of the total solar flares energy release, which is likely to be a signature of the acceleration of non-thermal particles to high energies during reconnection. In addition, also some Alfvén waves were observed to be energetic enough (speed of 10-25 km/s) to accelerate the solar wind [17]: this is associated with the detected presence of plasma jets from the chromosphere, which is probably heated by small-scale reconnection processes.

Another place where magnetic reconnection is expected to occur is the magnetosphere:

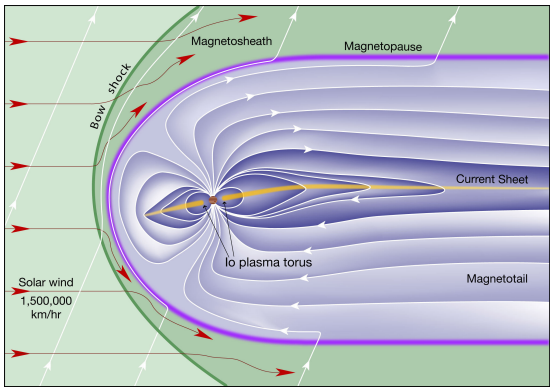

Figure 2.8: Scheme of the magnetosphere with presence of current sheets where reconnection occurs. Credits: https://lasp.colorado.edu/mop/

when the solar wind interacts with planetary magnetic fields, current sheets form as antiparallel field lines meet at the magnetic boundaries, and the magnetic field vanishes at their centre [89]. These current sheets were observed both in the magnetopause and in the magnetotail [79] [36] (shown in figure 2.8), where the Earth dipole field and the solar field interact.

Interesting is the case of the interstellar medium, a highly conductive gas which hosts star formation and dynamo processes which involve fast magnetic line reconnection mechanisms. In particular, reconnection might be associated to the process of ambipolar diffusion: when the ionization factor becomes too low, the magnetic field couples only with charged particles, and a drift of the neutral particles is generated with respect to the field and charged particles [10]. It is possible that the ambipolar drift in weakly ionized gas conditions is the MHD process forming thin current sheets characterized by short resistive timescales, and then the fields in the layer reconnect, given the extremely long ohmic diffusion times of magnetic fields in typical interstellar medium conditions [93].

Another example is given by the role of magnetic reconnection in accretion disks, characterized by a rapid transport of angular momentum required for the observed accretion rates. The magnetic field present in the Keplerian flow plays a crucial role in destabilizing magnetorotational instabilities (MRI), which evolve non-linearly and produce radial flows associated with highly bent magnetic field lines [28] which eventually reconnect. In particular, it was confirmed with 3D numerical simulations [25] that magnetic reconnection plays an important role in accretion disks: it can both saturate the momentum transport, and suppress the MRI. Furthermore, current layers were proved to form in the narrow regions that separate oppositely directed magnetic field lines [66]. In these layers, reconnection occurs in conditions of small magnetic diffusivity.

The last proposed example for astrophysical plasmas is related to magnetospheres of compact objects, i.e. black holes or neutron stars. This is a relativistic and collisionless regime, where the acceleration of relativistic particles occurs during reconnection events. Compact objects, such as pulsars, are characterized by extremely strong magnetic fields and fast rotation: when the magnetic axis is aligned with the rotational axis, a current sheet is formed in the equatorial plane after the opening of the dipole field caused by the radial outflow [55]. In this way, in correspondence of the current sheets, electromagnetic energy is converted into kinetic ultrarelativistic energy resulting as emitted radiation.

Magnetic reconnection phenomena have also been found in fusion plasma experiments, and, as already mentioned, reconnection reveals its-self through a rearrangement of the magnetic field lines. Not only RFP plasmas, but also another kind of plasma, the tokamak, has a toroidal configuration in the MHD regime. The difference between them is given by how their toroidal field is produced: if in RFPs it is mostly internally created, in tokamaks it is induced externally [89]. The study of reconnection in fusion plasmas is crucial, because it has an impact on the magnetic confinement efficiency.

In tokamaks, a typical phenomenon of magnetic reconnection consists in the Sawtooth relaxation oscillations: they appear as a periodic repetition of peaking and consecutive sudden flattening in the profile of the electron temperature [35]. In particular, also in the tokamak case the safety factor q, expressed in 2.33, can be used as a stability parameter. Magnetic reconnection was observed to cause partial mixing of field lines in the Tokamak Fusion Test Reactor, and this was revealed by the small changes detected in the q profile [44] which occurred in a timescale so short that it can be due only to field-line breaking and rearrangement. Similar variations in the q profile were also measured in other sawtoothing tokamak plasmas [44] [73].

As explained in paragraph §2.1.2, the RFP configuration is characterized by self-organization processes which lead the plasma towards a state of force-free field equilibrium at minimum energy and constant helicity. It is during these processes that magnetic reconnection occurs: magnetic energy is stored during a slow adjustment to an external driving force [89]. Then, the magnetic field reconnects and a new MHD equilibrium state is reached. In particular, in the Madison Symmetric Torus (MST), simultaneous reconnection events were detected at multitude radii (see paragraph §2.2.3). In the RFP the ion heating mechanism was found to be particularly strong due to such multiple reconnection events, following a large decrease in the stored magnetic energy which generates a significant magnetic self-organization of the global plasma [18]. However, this process is still being investigated.

Magnetic reconnection was studied in many laboratory plasmas, which were conceived for this purpose. In the Magnetic Reconnection Experiment (MRX) device, for example, reconnection is driven thanks to its flexible toroidal plasma configuration [88] in MHD regime. During some experiments in MRX, a typical 2D Sweet-Parker diffusion region profile was observed [88]. The time evolution of the measured flux contours of the reconnecting field is shown in figure 2.9. Moreover, in MRX the heating mechanisms of electrons have been deeply studied, and a quantitative hypothesis was proposed involving the Hall effect [90], which is the term including $\mathbf{j} \times \mathbf{B}$ present in the generalized version of the Ohm's law (2.9). The process can be observed in figure 2.10, where the motion of the reconnecting field lines into the neutral current sheet is depicted on the right on the (x,z) plane. In particular, the ions (represented by the blue lines) approaching the X point become demagnetized and while flowing they gradually change direction by 90° from the x to the z axis. The electrons (red arrows), instead, follow the magnetic field lines until the X point. According to the experimental results, as they flow through the separatrix regions of the current sheet, the electrons are violently accelerated towards the X point, probably due to a larger $\mathbf{E} \times \mathbf{B} \sim E_y/B_z$ velocity due to the decrease of the reconnection magnetic field at the origin ($B_z \sim 0$), while the electric field (E_y) remains uniform. After this, the electrons are even further accelerated when they flow along the narrow layers around the central separatrix. The consequence of this is that a circular net current pattern is generated in the (x,z) plane by the electron flows which results as an out-of-plane quadrupole

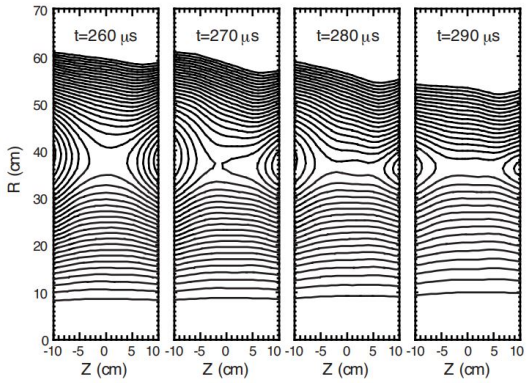

Figure 2.9: Proof of ongoing magnetic reconnection process in MRX device: the time evolution of the reconnecting magnetic field is represented by flux contours. The figure shows a 2D Sweet-Parker model. Credits: [88].

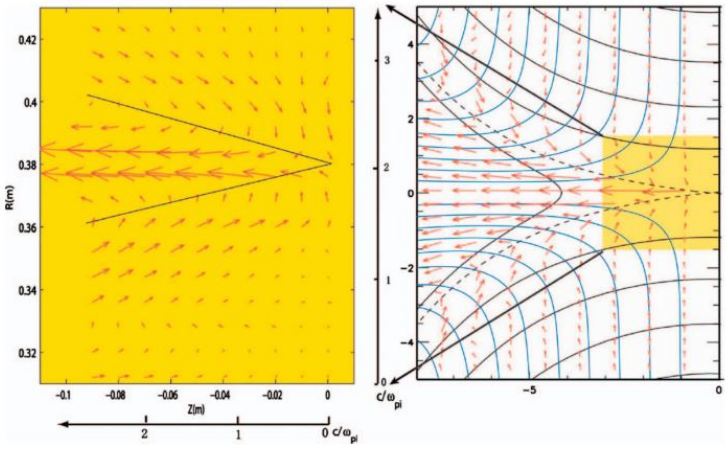

Figure 2.10: 2D profiles of the electron flow vectors detected by the MRX experiment [90] and associated numerical simulation (on the left and right respectively) in the region of the current sheet, where the electron flow (red arrows) and the ion flow (blue lines) are shown. A magnetic field component arises out-of-plane, and presents a quadrupole profile.

profile of the magnetic field [89]. Also in other experiments (such as MST [19]) these kinds of results were observed, and, moreover, the Hall effect was localized in the reconnection layer. As far as heating mechanisms are concerned, instead, they could be caused by electric potential drops aligned to the background magnetic field or it could be produced by plasma waves, like electrostatic waves [57][12][22].

In conclusion, to better understand how magnetic energy is converted into kinetic energy during reconnection, it is necessary to investigate the relationship between the particle acceleration and heating processes with the reconnection rates. In the RFP, reconnection occurs suddenly and with a very fast speed, and it causes a change of the magnetic field flux over a short time in a certain region of the plasma. This generates a large electric field along the magnetic field lines producing the acceleration of the electrons to superthermal energies. In particular, in both the solar flares and RFP relaxation events, a large amount of high energy tail electrons has been observed [89]. This topic will be treated in section §3.1.

2.2.3 RFP framework

Magnetic reconnection determines crucially the dynamics of a RFP plasma, where it is possible that large current sheets become unstable and generate tearing mode instabilities, which break the current sheets into magnetic islands [14]. As already explained in §2.1.2, the safety factor q (equation 2.33) presents a large number of resonant instabilities, as can be seen in 2.35. Therefore, in RFPs magnetic reconnection occurs as a multitude of simultaneous events in correspondence of all the rational surfaces where resonant instabilities (indeed present in the q profile) are triggered at different radii.

Let us enumerate the following kinds of states which describe the different conditions in which the RFP plasma can be found:

- Multiple-helicity (MH) state: a voluminous chaotic region is generated by the big amount of MHD modes resonating on different plasma layers which give rise to overlapping magnetic islands [7]. In this region the magnetic surfaces are destroyed and the confinement is not efficient. In this case the dynamo effect is due to the activity of many tearing modes, which produce the average parallel electrostatic field.

- Quasi-single helicity states (QSH): a single mode dominates the magnetic spectrum over secondary modes with lower amplitude. It was predicted [8] that in principle one single mode (single helicity states, SH) is enough to sustain the magnetic field (laminar dynamo process). This is the transition phase from MH states to SH states and it is characterized by intermittent occurrences of MH states. This transition can be either spontaneous or externally induced and was observed in many RFP devices. There are two kinds of QSH states:

  - Double axis state (DAx): When the dominant component of the magnetic field is up to a few percent of the average magnetic field, there are two O points and two twisted magnetic axes. In particular, the resonant magnetic surface is torn into a magnetic island centered around a secondary magnetic axis (indeed, an O point), while the main magnetic axis is still present and shifted by a certain amount. In addition, there is also an X point ($2.5a$), poloidally symmetric to the O point, related to the

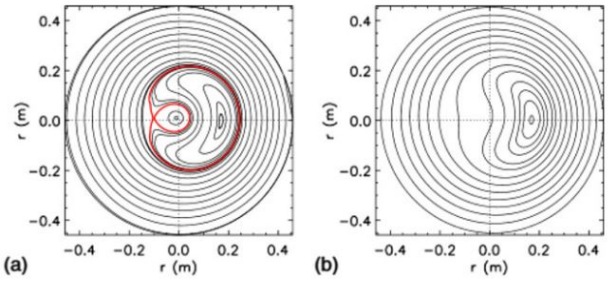

Figure 2.11: Magnetic topology change during the transition from DAx state to SHAx state. The disappearance of the initial small magnetic island, X point and related magnetic axis can be observed. Credits: [47]

island separatrix [48]. Therefore, in this state a well confined magnetic island can be observed and it has the periodicity of the dominant mode, which is associated to the innermost resonant tearing mode [56];

– Single helical axis (SHAx) state: the main magnetic axis, the X point, and the related separatrix have disappeared [48], and a helical structure with a single magnetic axis without X point is observed, which corresponds to the former island O point. This is an equilibrium configuration reached when the amplitude of the dominant mode is higher than a determined threshold.

The transition from DAx to SHAx state is shown in figure 2.11.

In RFPs the generation of toroidal flux, necessary (as explained previously) to sustain the configuration against resistive decay, can occur in discrete events [33]: the dynamo reconnection events or discrete reconnection events (DREs), associated to plasma relaxation. MH states, and the intermittent transitions towards them in QSH states, are associated to rearrangements of the magnetic topology during DREs. In particular, the helical flux is converted into toroidal flux through the reconnection process in this manner: the currents parallel to the magnetic field are reduced at the centre, where the field lines are mostly toroidal, which means reducing the poloidal flux, and, at the same time, these parallel currents are amplified at the edge, where, since the magnetic field is mostly poloidal, the toroidal flux is increased [89]. So, there is a global rearrangement of the plasma currents and of the plasma shape itself through the amplification of parallel currents [56].

This rearrangement of magnetic topology can be observed as a 'crash' in the time trace of the reversal parameter F defined in 2.30: a deeper F indicates the increase (in terms of absolute value) of the toroidal magnetic field, and therefore the generation of the toroidal flux related to parallel currents, namely current sheets where reconnection occurs. The F crash is also accompanied by the crash of the dominant mode and the growth of the secondary modes. Thus, at high plasma current discharges, reconnection lets the system pass from a SHAx state to MH state [56].

Magnetic reconnection is described by a succession of phases. The initial phase is associated to a helical deformation of the plasma column causing a charge separation which produces a spatially modulated electrostatic field, so that the main component of the velocity field is given by an electrostatic drift [92]. The helical deformation is visible after the phase-locking of the resonant tearing modes in the region where the (m=1) modes reach their maximum. Also the

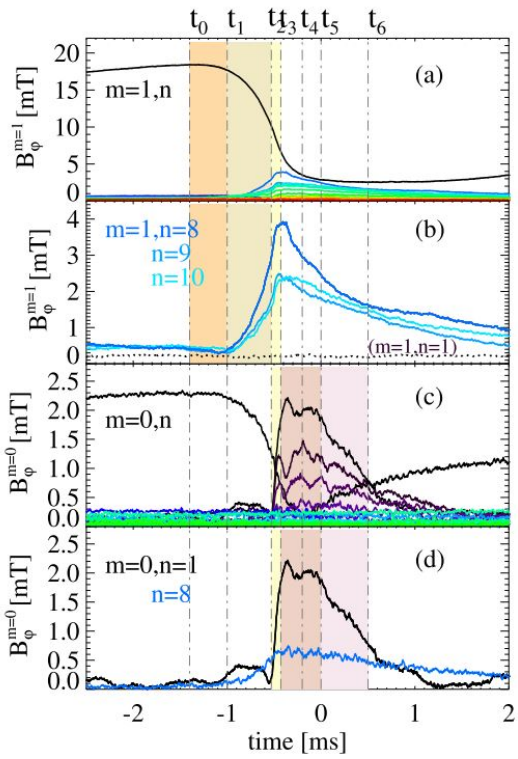

Figure 2.12: Results obtained by Momo et al. [56] for the MHD modes dynamics characterizing the DRE at consecutive time instants. Respectively, the *m=1* modes (a,b), and the *m=0* modes (c,d) are shown.

(*m=0*) modes lock in phase and this causes a deformation which modifies the plasma radius and cross section in the same toroidal region. During this phase, a toroidally localized burst of MHD activity is observed, which leads to the formation of a region where the interaction between the plasma and the wall is enhanced (together with the particle transport) [56]. So a chaotic MH state is reached and the MHD spectrum becomes broader. Let us define t_0 as the instant of time at which the localized magnetic field perturbation is maximum (corresponding to the minimum of F). The temporal sequence of events which characterizes the reconnection process (or equivalently the DRE) is the following (see figure 2.12)[56]:

1. $t = t_0 \simeq -1.4$ ms: The initial stationary helical SHAx state is perturbed by the phase-locking of all the *m=1* modes.

2. $t = t_1 \simeq -1.0$ ms: The $(m = 1, n = 8 - 10)$ modes increase and become resonant in the plasma core, namely the transition to the MH state occurs. The plasma current increases too. This is the beginning of the fast stage of the relaxation process in the core.

3. $t = t_2 \simeq -0.5$ ms: There is a rapid generation of the toroidal flux associated to a current density diffusion towards the edge. The MHD spectra are characterized by $(m = 1, n > 8)$ modes whose amplitude is increasing, with the phase-locking of all the secondary modes. Now also edge resonant modes appear in the layer where the poloidal component is strong.

4. $t = t_3 \simeq -0.4$ ms: An $m = 0$ magnetic structure forms at the edge, while the amplitude of the *m=1* modes starts decreasing. Now a poloidal current sheet exists at the edge

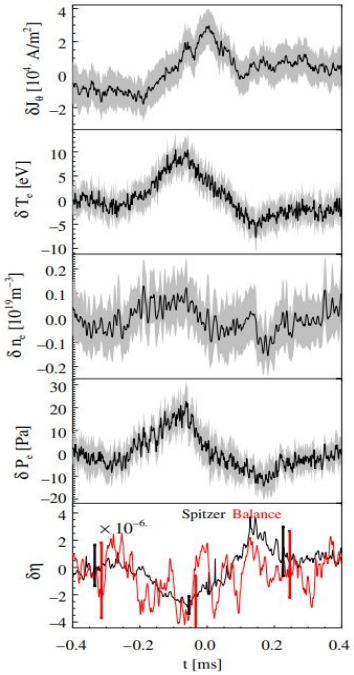

Figure 2.13: Perturbed edge ($r/a \approx 0.9$) plasma profiles for the electron temperature, density, pressure, and plasma resistivity during the propagation of the current sheet obtained by Zuin et al. [92]

(following the q profile), and the so-called "*m=0* reconnection" is now happening there, because the radial fields required to connect field lines at different radii are present [92]. In particular, there is an energy transfer from the *m=1* to *m=0* spectra in the reversal surface, where all the *m=0* modes are resonant.

5. $t = t_4 \simeq -0.2$ ms: While the poloidal current sheet is still forming, the *m=0* modes reach their maximum amplitude.

6. $t = t_5 \simeq 0$ ms: The F parameter reaches its minimum, and the amplitude of the *m=0* modes starts decreasing in the edge. This is the end of the reconnection stage.

7. $t = t_6 \simeq +0.5ms$: The current sheet disappears and also the *m=0* magnetic component.

In summary, the DRE involves a multitude of reconnection events starting in the core at *m=1*, and later propagating towards the edge. Gradually, a *m=0* perturbation (associated to the poloidal current sheet) moves toroidally and perturbs the edge plasma profiles (shown in figure 2.13), accompanied by a localized force balance between the pressure perturbation (originated by the current sheet) and the Lorentz force [92]. Magnetic reconnection is probably triggered by the approaching of the magnetic islands which develop on resonant surfaces and lead to the magnetic chaos [56].

Multiple helicity states have been observed since the first numerical experiments in RFPs, related to several single instabilities with poloidal wavenumber $m = 1$ [58] and a range of toroidal wavenumbers n, which couple and lead to a core of stochastic magnetic field lines and drive the formation of $m = 0$ magnetic islands [69]. Later, the MH state characterized

by several helical modes interacting together and then locking in phase was observed in the MST experiment [2]. Further evidence was given by the OHTE experiment in San Diego where the initial instability in form of a helical perturbation was observed consisting in many helical phase-locked modes with $m = 1$ [29]. Again in MST, an intense discrete dynamo activity was detected, characterized by the coupling of (m=*1,* n=*5–7*) modes followed by an (m=*0,* n=*0*) crash which generates toroidal flux and produces a small increase in the plasma current [30].

2.3 Turbulence

Magnetic reconnection is a turbulent process both in time (intermittent) and space (patchy) [89]. Turbulence is a state of a fluid characterized by velocities changing randomly in space and time, and there is not predictive capability. As a consequence, a statistical theory is needed which analyzes the average properties of turbulence. The quantities, such as the velocity, can be split into two parts:

$$\mathbf{v} = \bar{\mathbf{v}} + \mathbf{v}'$$

where $\bar{v} = \frac{1}{T}\int_0^T v(t)\,dt$ is an ensemble average, i.e. the mean flow, which can be written as [43]

$$\langle v(t)\rangle = \lim_{N\to\infty}\frac{1}{N}\sum_{n=1}^{N} v^n(t)$$

with N being the number of locations at which the quantity is measured at the same time, in order to do an average over different realizations. The fluctuating part is given by $\mathbf{v}'$, namely the turbulent velocity field. The correlation length of turbulence can be defined as [14]:

$$\overline{\mathbf{v}'(\mathbf{x},t)\cdot\mathbf{v}'(\mathbf{x}+\mathbf{r},t)} \tag{2.45}$$

where $\mathbf{r}$ is a distance. In fact, turbulent structures have a finite extension and can become uncorrelated: the typical shape of a correlation function is such that the fluctuating quantities have their maximum when the correlation distance $r = 0$, and they decrease at $r \to \infty$. This suggests that the dynamical properties of turbulence can be studied at different scales making a Fourier analysis. In the hypothesis of

- Incompressibility: $\nabla\mathbf{v} = 0$
- Homogeneity: the correlation function 2.45 is independent on $\mathbf{x}$
- Isotropy: the only dependence of 2.45 is on the magnitude of $\mathbf{r}$

we can define the energy spectrum of turbulence $E(k,t)$ writing [42]:

$$E(t) = \frac{1}{2}\langle v_i(\mathbf{x},t)v_i(\mathbf{x},t)\rangle = \int_0^\infty E(k,t)\,dk$$

which is an integral in the momentum (k) space, with $E(t)$ being the total kinetic energy per unit mass. The turbulent field can be thought as a composition of different Fourier components, of whom $E(k)$ is the energy spectrum, which, once integrated, gives the total energy per unit mass.

If a fluid is kept in isolation, it cannot have an equilibrium distribution because the kinetic energy decreases with time due to viscous dissipation processes. Therefore, the static equilibrium needs to be maintained by external means, which is the case of the stationary open systems where a continuous energy input balances energy dissipation. The turbulent velocity field can be considered as consisting in many eddies of different spatial scale, and the aforementioned input energy is a cascade process which transmits the energy from the larger eddies to the smaller ones. The larger vortices can give rise to the smaller ones: when the separation be-

tween two fluid points forming a tube randomly increases, according to Kelvin's theorem[3], the vorticity must remain constant, so that the cross section of the vortex tube decreases causing a stretching of it (at incompressibility conditions).

It is assumed that to each eddy a univocal Reynolds number lv/ν is associated, with a precise size l, typical velocity v, and viscosity ν. In particular, the larger vortices are not subjected to viscous dissipation of energy, so that the Reynolds number results larger for them. The intermediate eddies are able to transmit the energy, which finally arrives to the smaller ones, at whose scale the energy is dissipated, balancing the energy input. We can define the inertial range as the interval between k_d and k_L, which are respectively the wavenumbers at the dissipation scale and at the larger scale. In this interval the Kolmogorov's law describes the energy spectrum dependence on the momentum:

$$E(k) = C\epsilon^{2/3}k^{-5/3} \tag{2.46}$$

with ϵ being the energy transmission rate $\epsilon \sim \frac{v^3}{l}$. In particular, according to the theory, in the inertial range the energy flux through the wavenumber k does not depend on k, but rather corresponds to ϵ, which is a constant and controls the energy flux [82]. Two useful definitions are:

- the velocity increments:
$$\delta\mathbf{v}(\mathbf{r},\mathbf{l}) \equiv \mathbf{v}(\mathbf{r}+\mathbf{l}) - \mathbf{v}(\mathbf{r}) \tag{2.47}$$
where the velocity fluctuations δv_l are associated to the lifetime of scale l fluctuations $\tau_l \simeq \frac{l}{\delta v_l}$.

- the p-order structure function:
$$S_p(\mathbf{l},t) = \langle(\delta v(\mathbf{l},t))^p\rangle \tag{2.48}$$

Later Kolmogorov derived an exact relation ("Four-fifths law" [38]) for the third order longitudinal structure function given in terms of the mean energy dissipation for l lower than the integral scale [39]. This led to the law for the generic p-order structure function:

$$S_p(\mathbf{l},t) = C_p(\epsilon l)^{p/3} \tag{2.49}$$

where C_p is a constant which depends only on p. To summarize, a good representation of the energy spectrum can be seen in figure 2.14.

Therefore, turbulence consists in an energy transport from large fluid-scale structures to smaller scales, through a turbulent cascade of non-linear interactions. During such a process, also the energization of the particles is possible. In particular, when the energy reaches the ion and electron scales, some kinetic processes can convert the turbulent fluctuations energy into particle heating and acceleration. Two examples of these kinetic processes are the non-linear damping of waves or dissipation in coherent structures, which are structures localized in space and time, and include thin current sheets, magnetic islands, isolated flux-tubes, or small-scale

[3]Kelvin's theorem states that $\frac{d}{dt}\int_s \omega \cdot d\mathbf{S} = 0$, implying that the flux of the vorticity $\omega = \nabla \times \mathbf{v}$ is conserved and the vortex lines move with the fluid [14]

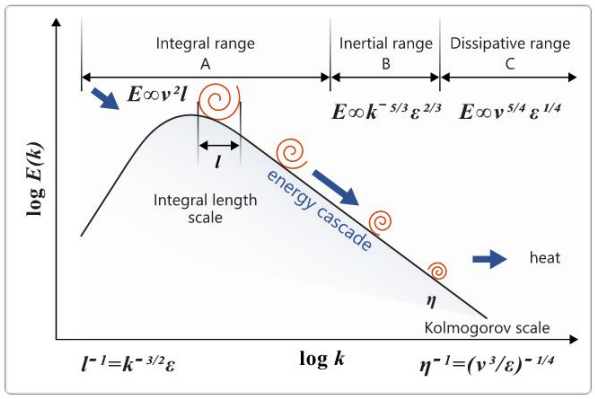

Figure 2.14: Typical spectrum of turbulence, including the different scales and ranges. Image credits: `https://help.altair.com/hwcfdsolvers/acusolve/topics/acusolve/training_manual/turb_scales_energy_cascasde_r.htm`

vortices [65]. From the observations, a strong energy dissipation and particle energization result in kinetic-scale regions, associated with strong electron currents and non-maxwellian distribution functions of the particles. In the case of the thin current sheets, the particle energization is also connected to small scale reconnection: these were observed in the turbulent magnetosheath, together with coherent structures at the electron scale like magnetic holes and vortices. Another example is the Kelvin-Helmholtz waves generated in boundary layers associated to a flow shear between adjacent plasmas, such as the magnetopause of the Earth [65].

In toroidally confined plasmas, a phenomenon occurs called anomalous transport which may be due to either magnetic or electrostatic turbulence [45]. The first possibility concerns the fluctuations of the radial component of the magnetic field δB_r which can distort the magnetic surface. The second possibility refers to fluctuations of the perpendicular electric field $\tilde{E}_\perp$ due to plasma instabilities, which might lead to the formation of vortex-like structures causing energy losses. Magnetic fluctuations play a fundamental role in the dynamics of an RFP plasma. If they are described by the form:

$$\tilde{b}_r = \sum_{m,n} b_{m,n}(r) e^{i(n\phi + m\theta)} \tag{2.50}$$

the stationary magnetic fluctuations are able to resonate on the rational surfaces producing magnetic islands [67]. In the condition of island overlap (given by the so-called overlap parameter), the magnetic field lines can pass from one island to the other transporting particles which end up being no longer confined. This stochastic transport due to magnetic fluctuations governs the energy transport in the core of RFP plasmas [75].

In conclusion, the two kinds of particle energization processes mentioned in this chapter, magnetic reconnection and turbulence, are not necessary independent, but they are often combined in a complex way. In particular, there is evidence of small scale reconnection in turbulence, as well as turbulence in large scale reconnection. Such a combination could further improve the efficiency of the energization mechanisms [65]. In order to better investigate these combined processes, multi-scale measurements are required: in some spacecraft obser-

vations [65] the reconnection diffusion regions (including magnetic islands, thin current sheets and other intermittent structures) were found to be turbulent and associated with a strong energization of the particles, like, for example, in the solar corona.

Chapter 3

Current experimental results and procedures

3.1 Superthermal electron flows

As explained in paragraphs §2.1.2 and §2.2.3, the dynamics of RFP plasmas are characterized by an intense MHD activity. Several experimental evidences confirm that the MHD activity is also correlated with the presence of fast particle flows, including both electrons and ions, observed in the periphery as well as in the core region of the plasma [87]. These electrons have typical energies exceeding the thermal velocity [31] pertaining to the tail of the energy distribution, and therefore are often dubbed as *superthermal*. The study of superthermal electrons in the experimental devices is essential because they can cause a large power loss when intersecting any obstacle coming out of the vacuum vessel surface and they can damage the materials in contact with the plasma. In particular, the radial diffusive velocity of these electrons results to be of order 10^3 m sec^{-1} [31], which means they reach the walls in a very short time causing the loss of all the power they bring from the walls. As a consequence, fast electrons may represent a crucial channel of energy loss.

As far as astrophysical plasmas are concerned, according to the observations of the WIND spacecraft [21], the electron acceleration process giving rise to the superthermal electrons resides in the diffusion region where magnetic reconnection occurs. In this region the power-law spectra appear more energetic than in the outflow region, and the preferential direction is the parallel or antiparallel one with respect to the guiding field. On the other hand, in the case of toroidally confined plasmas such as the RFP, the presence of the superthermal electrons is connected with the observation of bursts in the soft X-ray regime and subsequent crashes corresponding to the relaxation phases of the typical dynamo (see note [1] at page 10) events. Experimental observations obtained in the MST RFP experiment [21] revealed an anisotropic electron energization, but in this case the preferential direction is perpendicular to the mean magnetic field. This anisotropy results indeed as a non-thermal tail in the X-ray energy spectrum of the electrons in the core region during the reconnection events. In figure 3.1 it can be seen how the X-ray flux changes in time during magnetic reconnection: at energies higher than 20 keV it increases indicating the moment when fast electrons are produced. When the event

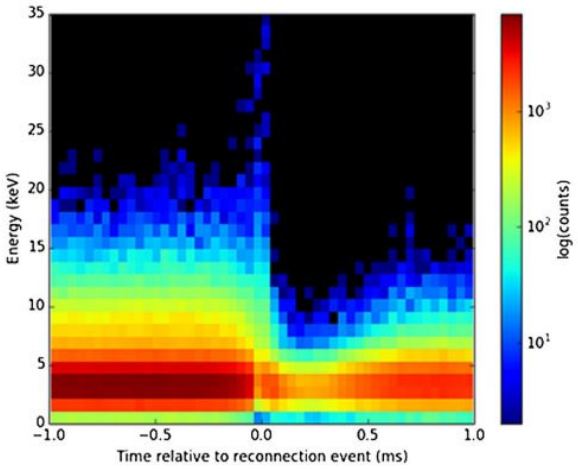

Figure 3.1: Evolution in time of the X-ray flux during magnetic reconnection in the MST RFP plasma. Dark red indicates high flux and dark blue no flux. Results obtained by DuBois et al. [21]

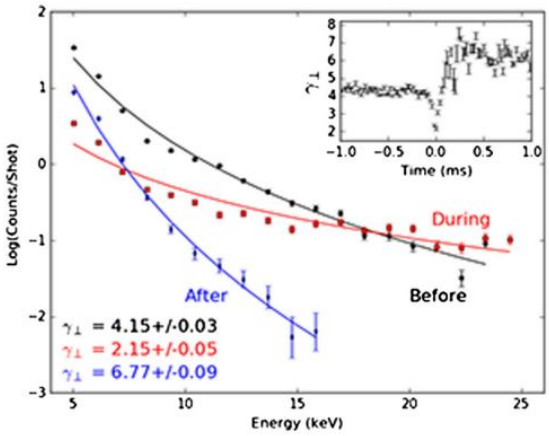

Figure 3.2: Spectra obtained by DuBois et al. [21] fitted with a power-law $\Gamma(E) \propto E^{-\gamma}$ with the tail spectral index γ changing with the different phases of magnetic reconnection.

ends there is a rapid decay of the flux. Also a spectrum is shown in figure 3.2 before, during, and after magnetic reconnection: during the event a flattening of the high energy tail is observed. This kind of dynamics for the X-ray tail is compatible with the dynamics of the RFP tearing modes and the magnitude of the energy released by magnetic reconnection, resembling in some way the WIND spacecraft results. This suggests that the origin of the anisotropic tails in the energy distribution of the electrons is also connected with the occurrence of MHD turbulent processes. Also another experiment, the PLT tokamak, has focused on this phenomenon and has found an anisotropic velocity distribution when studying the Brehmsstrahlung emission of runaway electrons [21].

The electron drift side can be defined as the surface along the same direction as the local current density vector characterizing the RFP configuration [86]. As far as the electrons in the edge plasma region are concerned, the typical temperature T_h of the tail on the electron drift side (namely the side from which most of the superthermal electrons come) is comparable to

(or greater than) the central electron temperature, and in the TPE-1RM20 experiment [87] it results that $T_h = 220$ eV, much higher than the bulk edge electron temperature $T_e \simeq 30$ eV. In this experiment, it was observed that outside the reversal surface fast electrons flow along the magnetic field lines. In particular, we can distinguish three candidates for the driving force:

1. The externally applied toroidal electric field accelerates electrons in the core region, and then a radial diffusion process [32] occurs: the accelerated electrons may start migrating radially along stochastic magnetic field lines to later become runaway electrons [86];

2. the dynamo electric field $\mathbf{v} \times \mathbf{B}$ driving the poloidal current which sustains the RFP configuration. It is produced by the non-linear interaction among the tearing modes and in principle it is able to enhance the poloidal loop voltage [87];

3. the force caused by wave-particle interactions: low-frequency Alfvén waves (definition in 2.15) interact with electrons and induce diffusion producing a superthermal electron beam parallel to the field in the edge region [91].

Furthermore, in a plasma a large enough electric field can overcome the collisional damping caused by the friction of a beam of accelerated electrons towards the bulk plasma. The consequence is that the electrons are accelerated to relativistic speeds, i.e. they become runaway electrons [74]. Such an electric field is called the critical electric field

$$E_c = n_e e^3 ln\Lambda / 4\pi\epsilon_0^2 m_e c^2$$

where ln Λ is the Coulomb logarithm [16]. In RFP plasmas the ratio E/E_c, where E is the electric field able to drive electrons, is large enough (till 0.1 in the TPE-1RM20 device [87]) for it to be plausible that the electron energy distribution function presents an high energy component.

In the TPE-1RM20 experiment [87], it was found that the fast electron current density profile may be subjected to a modulation caused either by the rotation of the MHD modes, or by the local magnetic field perturbation (toroidal and radial components), but the latter seems to be the dominant cause. Figure 3.3 shows the coherence[1] found between the fast electron current (j_{col}) and B_t, which is statistically meaningful at frequencies lower than 50 kHz. Similar results were obtained for the correlation between fast electrons and the $\mathbf{v} \times \mathbf{B}$ dynamo electric field which increases for the higher-energy portion of fast electrons. It can be stated that fast electrons are accelerated by the $\mathbf{v} \times \mathbf{B}$ field, which is mostly active near the reversal region [87].

In the RFX device, it can be assumed that superthermal electrons carry almost all the edge current density [84] (and the same applies also for the results obtained by Ingraham et al. [31]), and some currents were observed to be associated with the phase-locking of the MHD modes which induces the distortion of the plasma column and lets the superthermal flux intercept the first wall. In this experiment, the profile of the collected current presents a flat-top phase, and such a constancy gives a clue about the time behavior of the electron current density and temperature: the generation process of superthermal electrons and the distortion of the electron energy distribution function are stationary [84].

[1] In the article [87] coherence corresponds to the ratio of the square root of the power spectrum of a quantity $b(t)$ that has a linear relation with a quantity $a(t)$.

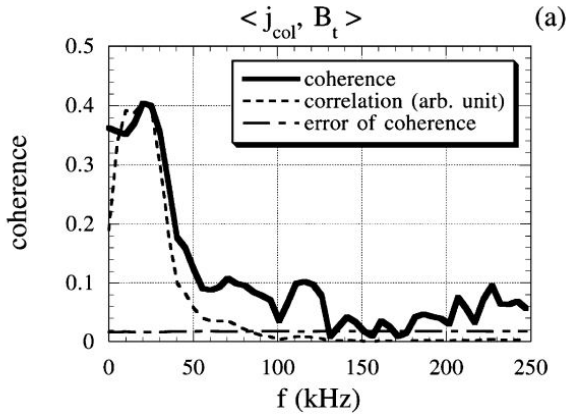

Figure 3.3: Coherence between the fast electron current j_{col} and the toroidal component of the magnetic field B_t. Results obtained by Y. Yagi et al. [87]

In conclusion, according to the experimental results, in the RFP configuration there are different possible mechanisms for the production of fast electrons:

1. the electrons are accelerated during the reconnection process of the magnetic field lines occurring in the RFP plasma.

2. the dynamo electric field $\mathbf{v} \times \mathbf{B}$ accelerates the electrons along the magnetic field lines which stochastically reach the edge region

3. the electron current density diffuses from the core to the boundary region according to the kinetic dynamo theory: the superthermal electrons are produced in the core plasma and then are transported to the edge. This is supported both by the values found for the fast electron temperature comparable to the core temperature, and by the fact that these electrons seem to be collisionless and coexist with the cold plasma component at the edge which is a rather kinetic mechanism [31].

Hard X-ray emissions were detected in the case of astrophysical plasmas as a signature of electron acceleration, for example in the case of solar flares [89] in which very energetic electrons were detected, associated to a high-energy component in the distribution function tail. In this case, it was proved that the process able to accelerate so efficiently the particles is related to the termination shock, which is a shock produced by super-magnetosonic reconnection outflows impinging upon dense, closed magnetic loops [13].

In astrophysical plasmas, the presence of accelerated charged particles which contain a high energy component in the energy distribution tail is very common. According to the observations, these particles exceeding thermal energy obey this kind of power law distribution:

$$4\pi f(v)dv \propto v^{-\alpha}dv$$

for $|v| > v_{th}$ [50]. In solar flares, for example, protons and electrons are accelerated by shock waves and reach MeV energies in the corona and interplanetary space [1]. Non-thermal particle populations are often associated to shocks, another example is the heliosphere, where shocks are seen to produce superthermal particles as part of their own formation process [34]. The

acceleration process, which is still not completely understood, leads to power-law particle spectra. Additional observations concern particle velocity distributions in the high speed solar wind, where the shape of the electron distribution function differs from simple bi-Maxwellians because a hot, strongly beamed, high energy electron component is present in addition to a distinct low energy electron component along the magnetic field directed away from the sun [24].

Finally, particle energization is often associated to the dissipation of plasma waves and turbulent fluctuations [65]. In the magnetosheath, superthermal electrons were detected by Cluster presenting a power-law distribution of whom the slope was computed: it was found to decrease as the ratio between local electron plasma and cyclotron frequencies ω_{pe}/Ω_e increases [49], which suggests that the power-law distribution derives from a process of wave scattering.

3.2 MHD turbulence and intermittency

Every kind of magnetized plasma in the universe is characterized by MHD turbulence, which develops when the magnetic Reynolds number 2.13 is large enough. Indeed, the properties of MHD turbulence can be studied in laboratory plasmas as well, including the RFP configuration, characterised, as already explained, by a very high level of fluctuations.

It is possible to consider small scale turbulence as an ensemble of Alfvén waves propagating along the average magnetic field, and the possible interactions are those between modes travelling in opposite directions [6]. It is assumed that $\mathbf{k}, \mathbf{p}, \mathbf{q}$ wave vectors interact satisfying $\mathbf{k}+\mathbf{p}+\mathbf{q}$=0. In the case of non-magnetized turbulent fluids described in section §2.3, the energy spectrum is described by the Kolmogorov's law 2.14, and it is possible to define a similar law in the MHD case, in which the energy decay spectrum is influenced by the presence of the magnetic field, the so-called Alfvénic effect, which slows down the energy transfer process, as will be explained hereafter.

Let us now use the Elsasser variables $\mathbf{z}^{\pm} = \mathbf{v} \pm \mathbf{B}$, which represent pure Alfvén wave perturbations propagating either in the direction of the background magnetic field $\mathbf{B}_0$ or opposite to it [51], to rewrite the MHD equations (section §2.1.1) in this way [23]:

$$\frac{\partial \mathbf{z}^{\pm}}{\partial t} \mp (\mathbf{v}_A \cdot \nabla)\mathbf{z}^{\pm} + (\mathbf{z}^{\pm} \cdot \nabla)\mathbf{z}^{\pm} = -\nabla P + \frac{\nu+\lambda}{2}\nabla^2 \mathbf{z}^{\pm} + \frac{\nu-\lambda}{2}\nabla^2 \mathbf{z}^{\pm} \tag{3.1}$$

where $P = p + B^2/2$ is the total pressure, and $\mathbf{v}_A$ the Alfvén velocity 2.15. Now, let us consider the two invariants in ideal 2D MHD [23]: the total energy

$$E = \frac{1}{2}\int (v^2 + B^2)\, d^3x = \frac{1}{2}\sum_{\mathbf{k}} (|v_{\mathbf{k}}|^2 + |B_{\mathbf{k}}|^2) = E_V + E_M$$

and the cross helicity

$$K = \frac{1}{2}\int \mathbf{v}\cdot\mathbf{B}\, d^3x = \frac{1}{2}\sum_{\mathbf{k}} (\mathbf{v}_{\mathbf{k}} \cdot \mathbf{B}_{-\mathbf{k}})$$

which measures the imbalance between interacting waves. Using the Elsasser variables these two equations can also be written in form of the so-called pseudo energies [23]:

$$E^{\pm}(t) = \frac{1}{2V}\int |\mathbf{z}^{\pm}(\mathbf{r}, t)|^2 d^3x \tag{3.2}$$

It is possible now to make a dimensional analysis by considering the interaction between Alfvénic fluctuations (eddies) of the same scale $l \sim k^{-1}$, assuming the fluctuations are local in the wavenumber space [20]. Two different timescales are involved: the one related to the transport velocity, which is v_A in this case,

$$\tau_A \simeq \frac{l}{v_A}$$

and the lifetime of the fluctuating eddies

$$\tau_l^{\pm} \simeq \frac{l}{\delta z_l^{\mp}}$$

Considering that $\tau_A << \tau_l^{\pm}$, the variation in amplitude $dz^{\pm}$ of a given vortex $\delta z^{\pm}$ caused by its interaction with another one in one interaction time τ_l can be computed taking equation 3.1 without considering the last two dissipative terms (in the inertial range), obtaining [20]:

$$dz^{\pm} \sim \tau_l \delta z^{\pm} \delta z^{\mp} / l \tag{3.3}$$

If the number of stochastic interactions between similar eddies is N, the amplitude variation is $\Delta z^{\pm} \sim \sqrt{N} \cdot dz^{\pm}$. This leads to the number of interactions necessary for an eddy to obtain a variation $\Delta z^{\pm}$ equal to its initial amplitude $\delta z^{\pm}$:

$$N^{\pm} \sim \frac{l^2}{\left(\delta z^{\mp}\right)^2} \cdot \frac{1}{\tau_l^2} \sim \left(\frac{\tau_l^{\pm}}{\tau_l}\right)^2$$

Taking the time of one interaction τ_l, the total time for the modification of the amplitude $\delta z^{\pm}$ at the scale l for $N^{\pm}$ interactions is

$$T^{\pm} = N^{\pm} \cdot \tau_l \sim (\tau_l^{\pm})^2 / \tau_l$$

In the case of fully developed turbulence, τ_l corresponds to the Alfvénic time τ_A defined above, so we obtain

$$T^{\pm} \sim v_A l / \left(\delta z^{\mp}\right)^2$$

Let us now consider the stationary symmetric case $|\delta z_l^+| \sim |\delta z_l^-| \sim |\delta z_l|$ [20] such that the transferred energy flux Π between the vortices corresponds to a value ε independent on l, so that $\Pi \sim \left(\delta z\right)^2 / T$, where T for brevity corresponds to the time $T^{\pm}$ previously defined. Substituting we get $\varepsilon \sim \left(\delta z\right)^4 / v_A l$. If we then write $(\delta z)^2 \sim kE(k)$ [20], where $E(k)$ is the energy density in mode k, the Iroshnikov-Kraichnan power-law can be derived:

$$E(k) \sim (\varepsilon v_A)^{1/2} k^{-3/2} \tag{3.4}$$

which represents the energy spectrum in the MHD turbulence case.

The main difference with respect to Kolmogorov's law is that the MHD spectrum not only depends on ε, but also on the large scale quantity v_A related to the fluctuations along the mean magnetic field. The presence of this preferential direction, namely the fact that the interaction time (above called τ_l) corresponds to the Alfvénic time in turbulent MHD, means that the energy transfer time is

$$T^{\pm} \sim \tau_l^{\pm} \cdot \left(\frac{\tau_l^{\pm}}{\tau_A}\right) >> \tau_l^{\pm}$$

because in this case $\frac{\tau_l^{\pm}}{\tau_A} >> 1$. Therefore, the 2D spectrum ($E(k) \sim k^{-3/2}$) results to be less steep, namely the energy transfer process is slower than in the case of non-magnetized fluids ($E(k) \sim k^{-5/3}$) where $T^{\pm} \sim \tau_l^{\pm}$.

Let us put back the attention to Kolmogorov's law 2.14: it establishes a well defined shape for the energy spectrum $E(k)$, which was explained also with the "Kolmogorov 1941 theory" (K41) [39]. This theory is connected with the symmetry properties of the Navier-Stockes

equation 2.11 [38], one of which is the h rescaling:

$$(t, \mathbf{x}, \mathbf{u}) \rightarrow (\lambda^{1-h} t, \lambda \mathbf{x}, \lambda^h \mathbf{u})$$

for arbitrary λ and h. As mentioned in paragraph §2.3, the energy transmission rate is $\epsilon \sim v^3/l$, where v and l are the scales (velocity and size) of the eddy. If the scale variation is $l \rightarrow l' = \lambda l$, then all the variables are scaled in the following way [82]:

$$\begin{aligned} \mathbf{v} \rightarrow \mathbf{v}' &= \lambda^h \mathbf{v} \\ P \rightarrow P' &= \lambda^\chi P \\ \rho \rightarrow \rho' &= \lambda^\mu \rho \end{aligned} \tag{3.5}$$

Respecting the scaling transformation invariance, these can be substituted in the expression for the energy flux:

$$\epsilon \rightarrow \epsilon' = \lambda^{3h-1} \epsilon$$

Since, as seen in §2.3, according to Kolmogorov's theory the energy flux must be a constant in the inertial range, then h=1/3. This unique value determines the scaling law of the p-order structure function 2.48 seen in section §2.3, which becomes $\langle (\delta v(r))^n \rangle \approx r^{\zeta(n)}$ with $\zeta(n) = n/3$.

Therefore, h=1/3 is the Hoelder exponent[2] with whom the following definition for the two-point increments is valid:

$$\delta v_x(l) = |\mathbf{v}(\mathbf{x} + \mathbf{r}) - \mathbf{v}(\mathbf{x})| \sim l^h$$

where $\mathbf{v}$ is a generic turbulent field, $\mathbf{x}$ is a position, and $\mathbf{r}$ corresponds to the scale ($|\mathbf{r}| = l$). Actually, both in the case of ordinary fluids and MHD flows, the energy cascade process is inhomogeneous, because the energy transfer is favoured where gradients are larger. In particular, as the energy cascade proceeds towards the smaller scales, the energy becomes concentrated on precise regions of space, so that some intermittent energetic structures emerge from the fluctuation background [52] as local discontinuities or sudden bursts. Therefore, by the term "intermittent" it is meant that turbulent energy dissipation is strongly localized in temporal and spatial sense, namely the statistical properties of plasma fluctuations are scale-dependent. As a consequence, the probability distribution function (PDF) of $\delta v_x(l)$ is scale-dependent too: it is gaussian at large scales because the fluctuations are mostly independent one on the other, while approaching the dissipation scales the formation of small-scale energetic structures makes the tails of the distribution non-gaussian, because the stronger events have a higher probability of occurrence. This phenomenon consisting in the change in the shape of the PDF of the velocity difference for different scales is known as anomalous scaling [59] or intermittency, and basically it involves an uneven distribution of the turbulent energy dissipation rate. Quantitatively, the scaling of the structure function can be written as

$$S_l^{(q)} \sim l^{\zeta_q}$$

[2]The Hoelder exponent allows to characterize locally irregular functions. The Holder exponent of a function f measures how irregular f is at each point. The higher the exponent at a point, the more regular the function at that point [72]. A mathematical definition is enunciated in [72].

where $S_l^{(q)}$ are higher order momenta, and $\zeta(q)$ is a non linear function of q characterized by a lower profile with respect to Kolmogorov's linear law [82]. In particular, the structure function, which can be considered as a spatial average of δv_l weighted on the exponent q, increases as a power-law of the scale. The anomalous scaling effect is more visible for $q > 3$, when higher fluctuations have a higher impact. Intermittency can be studied with a multifractal approach in order to account for the variation of the Hoelder exponent h at different points of the fluid.

The fluctuations can also be intended as magnetic field fluctuations across the turbulent structures such as the stochastic variables $\delta B(\tau) = B(t+\tau) - B(t)$, where τ is the scale, and the scaling law is $\delta B(\tau) \sim \tau^h$ [9].

In the RFP configuration, intermittency is mostly present in the plasma edge region near the external wall, where the difference between the scaling exponent ζ_p and $p/3$ is larger. Therefore, it can be stated that the anomalous scaling laws of the PDFs depend on the position in the plasma [9]. The deviation increases in conditions of anisotropy and it is likely to be associated to passages of coherent structures. This is also possibly connected to the bursting events which have been observed in the turbulent boundary layers. So, it is crucial to understand the relation between bursting events detected in the time tracks of the plasma signals and small scale intermittency. In particular the intermittent structures may be influenced either by walls or by the current sheets at the edge. This highlights the importance of studying intermittent events, also to have an idea of the nature of the magnetic fluctuations to better constrain the confinement process in the RFP plasmas, which is also part of the targets of this thesis project.

Let us now introduce the mathematical tools and methods which were implemented in this work in order to relate anomalous scaling, intermittency and bursting events. At this point, it is crucial to introduce the concept of wavelet coefficients, which can be obtained conducting a wavelet decomposition of the velocity signals acquired in the experiments. Mathematically, the wavelet coefficients are defined as [59]:

$$w(r,x) = \frac{1}{r}\int \psi^*((x'-x)/r)u(x')\,dx'$$

where ψ^* is the complex coniugate of the wavelet function ψ, $u(x)$ is the analyzed signal, and r is a scale. The existence of a correspondence between the velocity difference and the wavelet coefficients is fundamental, because it makes the wavelet transform the analytical instrument allowing for the study of the PDF of the wavelet coefficients at different scales and distances from the walls. The wavelet transform keeps the locality present in the signal and consequently allows for its local reconstruction, so it takes into account the local properties of the turbulent field by correlating the signal with a family of waveforms well concentrated in time and frequency. The benefit is the wavelet transform is an indicator of the scaling laws: when the structure function of a signal scales as a power-law, so do the wavelet coefficients, such that

$$\langle w(r,x)\rangle_x \ \sim r^\alpha$$

with α being the scaling exponent and $\langle ...\rangle_x$ an average over the positions x.

The wavelet coefficients build the indicators of intermittency currently used. The first to be defined is the measure of intermittency, also known as *Local Intermittency Measurement*, *I*

[59]:

$$I(r,x) = \frac{|w(r,x)|^2}{\langle |w(r,x)|^2 \rangle_x} \tag{3.6}$$

which represents the local activity of the fluctuating field at different scales. The second fundamental indicator is the 4th order momentum of the PDF, known as flatness F, which in terms of wavelet coefficients can be defined as:

$$F(r) = \frac{\langle w(r,x)^4 \rangle}{\langle w(r,x)^2 \rangle_x^2} \tag{3.7}$$

which is related to I in the following way:

$$F(r) = \langle I(r,x)^2 \rangle_x$$

In particular, it can be assumed that the value of F for a gaussian distribution is equal to 3. The I parameter is used as a threshold to select a portion of the signal of a given scale r_0 which physically corresponds to select the instant of passage of coherent structures in the signals obtained in form of times series. The method consists in computing the flatness F at different wavelet scales. There are two possible results [59]:

- F is greater than 3: a threshold on I is imposed and F is re-computed excluding the regions where I overcomes the threshold mentioned above. If, after this, F is still greater than 3, the threshold is lowered and the process is repeated till F reaches a value lower than 3 at all the scales
- F is lower than 3 at a certain scale: this is the limit at which the events are not detected

For each of the analysed temporal scales, this method allows to disentangle in the signal those fluctuations which are responsible for the departure from gaussianity caused by higher tails in the PDF. At smaller scales a lower threshold on the I parameter is required.

Castaing [11] introduced a method to describe the PDF of the increments defined in Kolmogorov's theory, which is based on the fact that at each scale the energy transmission rate ϵ between fluctuations does not possess an homogeneous scaling property [81]. Inside the multifractal description, each region of space can be assumed to be characterized by the same distribution P_0 of field fluctuations with a variable width σ. The field fluctuations depend on the cascade efficiency and on the fraction of space through a weight $L(\sigma)$. Therefore, the PDF consists in the continuous superposition of all these distributions of different weight associated to the distribution function of the widths σ. Given the scale λ, assuming that the energy transfer is associated to a multiplicative hierarchy of energetic structures [81], the PDF of fluctuation variances is [11]:

$$L_\lambda(\sigma_l) = \frac{1}{\lambda_l \sqrt{2\pi}} exp\left(\frac{ln^2 \sigma_l/\sigma_{0,\lambda}}{2\lambda_l^2}\right) \tag{3.8}$$

with $\sigma_{0,\lambda}$ the most probable value of σ_l. Like the local energy transfer rate, the variances follow a log-normal distribution due to the random distribution of the local efficiency of the energy

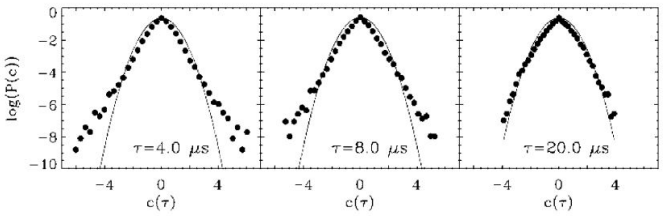

Figure 3.4: Probability density function (PDF) of the wavelet coefficients computed at different scales τ. Results obtained by Antoni et al. [3]

cascade. Then, we consider P_0 as a gaussian distribution of the form:

$$P_0(\delta\psi_l, \sigma_l, a_s) = \frac{1}{\sqrt{2\pi}\sigma} exp\left[-\frac{\delta\psi_l^2}{2\sigma^2}\left(1 + a_s \frac{\delta\psi_l/\sigma}{\sqrt{1+\delta\psi_l^2/\sigma^2}}\right)\right] \tag{3.9}$$

including the scaling law $\delta\psi_l \sim l^h$ and the correction term $\exp\left(-\frac{\delta\psi_l^2}{2\sigma^2} a_s \frac{\delta\psi_l/\sigma}{\sqrt{1+\delta\psi_l^2/\sigma^2}}\right)$, and, finally, for each time scale we obtain the probability distribution function

$$P(\delta\psi_l) = \int_0^\infty L_\lambda(\sigma_l) P_0(\delta\psi_l, \sigma_l)\, d\ln\sigma_l \tag{3.10}$$

In particular, it can be seen that if $\lambda_l^2 = 0$ equation 3.8 takes the form of a δ-function $\delta_a(x) = \frac{1}{\sqrt{\pi}|a|} e^{-(x/a)^2}$ where $a = \sqrt{2}\lambda_l$ and $x = \ln\frac{\sigma_l}{\sigma_{0,\lambda}}$, and consequently 3.10 becomes a gaussian of width $\sigma_{0,l}$. Therefore, as λ_l^2 increases, more values of σ_l are included (as a increases, the width σ of $\delta_a(x)$ increases, and vice-versa), and the PDF tails increase [81]. That is the reason why intermittency is studied analysing the scaling behaviour of the exponent λ_l^2 at different scales l. Similar λ_l^2 values imply similar degrees of intermittency.

The statistical properties of the fluctuations of the floating potential (which is a signal depending on the plasma potential and electron temperature, as will be seen in the following chapter) and the phenomenon of intermittency were studied in the RFP plasma of the RFX device [3]. Figure 3.4 shows an example at different scales τ of the PDF of wavelet coefficients $c(\tau)$. It can be seen how at larger scales (like $\tau = 20.0\mu$s in the figure) we have a quasi-gaussian distribution, while going towards smaller scales ($\tau = 4.0, 8.0\mu$s) the tails gradually deviate in a more visible way towards a non-gaussian distribution. The selected events consist in strong gradients present at all the scales, which are generated by the dynamics of coherent structures [59]. Therefore, the deviation from gaussianity, which in this case indicates small-scale intense fluctuations in the potential (involving a relevant energy fraction of the signal), can be characterized through the generation of these coherent structures [3]. Similar results come from the statistical analysis carried out in the TPE-1RM20 device [64], where the electron current PDF exhibits the same deviation from gaussianity at higher energies. As already explained above, in the experiment [59] it was found that intermittency increases at decreasing distances from the wall, observing gradually stronger ζ_p anomalies. Figure 3.5 shows this decrease in the intermittency parameter $\mu = 2 - \zeta_6^*$, with ζ_6^* being the scaling exponent ζ_p of the sixth order structure function. μ gives the anomaly with respect to Kolmogorov's law.

Additional evidence of intermittency is inferred from the observations by Voyager 1 of the

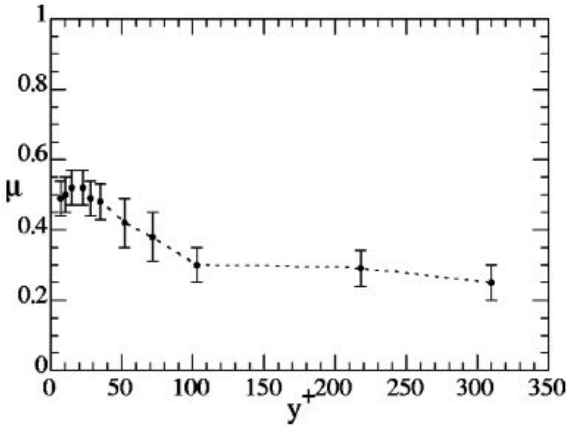

Figure 3.5: Intermittency parameter μ as a function of the distance from the wall expressed by the vertical coordinate y^+. Results obtained by Onorato et al. [59]

local interstellar medium (LISM) corresponding to the heliospheric boundary layer (HBL), which is the region adjacent to the heliopause [26]. In this case, magnetic field distributions exhibit presence of intermittency in high frequency data, associated to coherent-fine scale structures and weak current sheets. The associated measured magnetic field fluctuations have an amplitude reaching 10 percent of the magnetic field strength, and the timescales involved are in the order of seconds up to one hour. Analysing the magnetic field increments $\Delta_\tau \mathbf{B}(t;\tau) = \mathbf{B}(t) - \mathbf{B}(t+\tau)$ high-shear events were observed, which are signature of the presence of small-amplitude discontinuities compatible with filamentary structures [26]. Finally, the small-scale magnetic field was found to be intermittent, as indicated by the resulting PDFs of the magnetic field increments, shown in figure 3.6, which were fitted using the q-gaussian distribution, composed of a gaussian core and power-law tails. Also in the case of the solar wind [54], the presence of coherent structures was detected. In particular, the PDF of the distance between observed events (i.e., the waiting times, described later) in the solar wind data resemble pretty well the distribution resulting from simulated 3D MHD turbulence.

Furthermore, in addition to be associated to structures like current sheets in astrophysical plasmas, intermittency results to be related to the relaxation events in laboratory experiments. For example, the detection of the intermittent events in TPE-1RM20 [64] is associated to bursts of electron current which, apart from involving half the total current and belonging to the non-gaussian tail of the PDF, tend to cluster in time during relaxation events. Similar considerations apply in the RFX-device [3] for the coincidence of the local minima of the fluctuating potential with relaxation events.

Therefore, in the end, the purpose is to understand if a correlation of the intermittent events with magnetic reconnection exists: we would expect that this kind of events are correlated also with the phases of the reconnection process. In particular, as explained in section §2.2.3, at the instant of generation of the toroidal flux we assist to the formation of an electromotive force in the poloidal direction, which alters the toroidal current and impedes the flux generation [56]. This is supposed to be visible on the time series of the reversal parameter F 2.30 with a minimum. Here comes the aim of the thesis: finding the correspondence between the presence of the coherent structures and all the events described in chapter §2.2, including, for example:

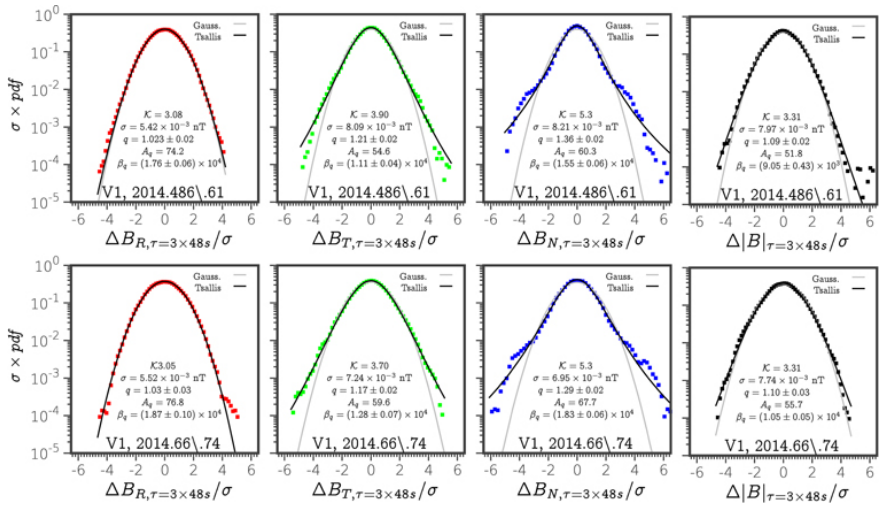

Figure 3.6: PDFs of magnetic field increments out of the data measured by Voyager 1. Two time intervals are considered (up and down rows) for three components of the magnetic field from left to right involving different directions with respect to the Sun position, equatorial plane and rotation, plus the field strength. Credits: [26].

- the decrease in the edge toroidal magnetic field resulting as the minima in F
- the slight peak in the toroidal plasma current I_p
- the increase in the toroidal flux
- the MHD activity involving the dominant and secondary modes

which occur progressively during magnetic reconnection in RFP plasmas and can be observed in the fluctuations of the signals like in figure 3.7.

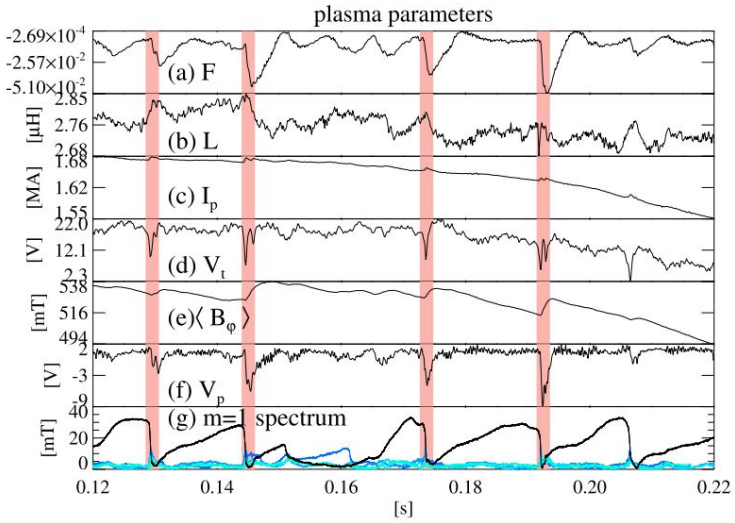

Figure 3.7: Times series of the signals from the RFX-mod RFP plasma which are subjected to modifications and fluctuations due to magnetic reconnection. We can focus on the reversal parameter (a), the plasma current (c), the averaged toroidal magnetic field (e), and the MHD modes (g). The discrete relaxation events are indicated by the pink vertical lines. Results obtained by Momo et al. [56]

Chapter 4

Data Analysis

As extensively emphasized above, the aim of this thesis project is to find a correlation between the acceleration of the particles during magnetic reconnection and MHD turbulence in a toroidal RFP plasma. The data analysis has been carried out on signals collected in form of time series by the RFP plasma device TPE-1RM20 at the Electrotechnical Laboratory [87] in Tsukuba, Japan. This experiment, as already mentioned previously had the aim of studying the fast electrons detected at the edge plasma region. In support of the thesis, the results have been compared with those obtained analysing the signals of the RFX-mod RFP device at Consorzio RFX, in Padua, Italy.

4.1 Diagnostics

4.1.1 TPE-1RM20 device

TPE-1RM20 is a toroidal configuration, whose geometry can be visualized in figure 2.2 with the toroidal angle ϕ, the poloidal angle θ and the radial coordinate. The toroidal direction is along the toroidal field on the axis, the poloidal field along the local poloidal field, and the radial direction points outwards [87].

TPE-1RM20 has a major radius of 0.75 m and minor radius of 0.192 m. Its operating gas is deuterium. It can reach a maximum plasma current of 280 kA and pulse duration time of 17 ms, and it is characterized by a triple-layered shell structure consisting in a thin double-layered copper shell and a thick copper shell. For the plasma to remain stable the shell proximity b/a, where b is the inner minor radius of the innermost shell and a is the minor radius of the plasma, is equal to 1.12. The shells are conductive and are such that the penetration time for the vertical field B_V[1] is much longer than the current duration time [85]. There are four operating parameters: $I_p, F/\Theta, B_V$ and p_{d2}. The former two, where F and Θ are the reversal and pinch parameters (2.30,2.28) and I_p the plasma current, scan the majority of the database, while B_V is used for equilibrium control, and p_{d2}, the filling pressure of deuterium gas, scans the electron density n_e. TPE-1RM20 [87] is monitored by an optimized equilibrium control such that the centre of the last closed flux surface corresponds to the centre of the vacuum

[1]The DC vertical field B_V (Direct Current electromagnetic field) consists in a constant or static DC field emission at a frequency of 0 Hz.

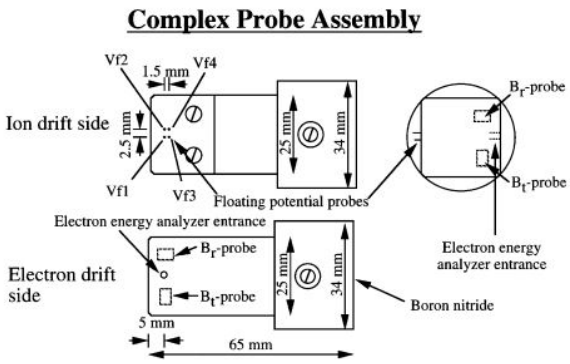

Figure 4.1: Scheme of the complex probe structure with all of its components: an Electron Energy Analyzer measuring the electron flux, four tungsten pins for the floating potential (namely the electric field), and two magnetic coils for the magnetic field. Image credits: [87]

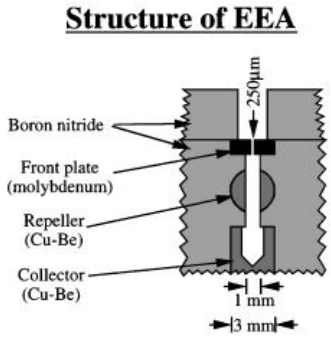

Figure 4.2: Scheme of the structure of the Electron Energy Analyzer (EEA) composed of a front plate, a repeller, and a faraday cup. Image credits: [87]

vessel. The first wall is made of stainless steel and/or molybdenum [85].

This experiment involves the use of a complex probe in order to investigate the correlation at the same plasma radius between the current density of fast electrons and other quantities, such as the local dynamo electric field $\mathbf{v} \times \mathbf{B}$. Figure 4.1 shows a scheme of the complex probe with all of its components: the Electron Energy Analyzer (EEA), four tungsten pins, and two magnetic coils. The complex probe is inserted inside a small boron-nitride case having a cross section of 25 × 25 mm. It is fixed on a manipulator, which can be driven linearly towards the plasma and rotated around its axis, and it is installed in correspondence of an outer horizontal porthole in the equatorial plane. The tip of the probe was set at a plasma depth of 25 mm ($r/a = 0.87$). Not to cause damages, lower plasma current discharges are used, with the maximum I_p around 50 kA. As the intensity of the discharge decreases, the shorter is the discharge duration because the reversal of the toroidal field is shallow.

The first component of the complex probe to be described is the EEA, an analyzer with an electrostatic retarding potential which allows for a direct measure of the energy distribution function of the electrons and the flux. The centre of its entrance hole is suspended 5 mm from the tip of the probe. The structure of the EEA is shown in figure 4.2, and it consists in:

- a front plate (1 mm-thick molybdenum) with a pinhole of 250 μm which reduces the

fast electron current limiting the Larmor radius of the incoming electrons: this reduces the damages to inner electrodes due to the high heat flux and eliminates the bulk of ions at the plasma edge. Since here the magnetic field is mostly poloidal, at constant perpendicular velocity the electron radius changes with the plasma current I_p;

- a repeller made of Cu-Be (1 mm internal diameter, 3 mm thickness) which imposes a threshold to the energy of fast electrons. The repeller voltage applied is -300 V;
- a faraday cup made of Cu-Be (1.5 mm internal diameter): the collector of the electron current j_{col} which has an angular distribution profile with full-width-at-half-maximum corresponding to the angular resolution related to the electrodes.

Both the front plate and repeller voltages are controlled by a voltage-divider. The output from the voltage-dividers is fed into electro-optical converters for the data acquisition. The data acquisition is based on a Computer Automated Measurement And Control system using analog-to-digital converters.

Secondly, the four tungsten pins, characterized by a diameter of 0.5 mm and plasma protrusion of 2 mm, measure a floating potential. They are appropriately protected from the fast electron flow being located at the opposite side with respect to the EEA entrance hole, and extend

- to 1.5 mm in the radial direction to measure the radial component of the electric field E_r;
- to 2.5 mm in the respective normal direction to obtain the component E_n. This corresponds to the toroidal electric field, E_t, when the EEA entrance hole is directed along the poloidal direction.

Only the floating potential V_f is used for the calculation of the local electric field, which satisfies

$$V_p = V_f + \alpha T_e \tag{4.1}$$

with V_p being the plasma potential, α a constant number around 3, and T_e the local electron temperature. The toroidal and poloidal components are obtained from $\mathbf{E} = -\nabla\phi$ taking the difference between the floating potential measured by the pins in each direction, for example [87] $E_t = -((V_{f2} + V_{f4})/2 - (V_{f1} + V_{f3})/2)/d$, where f1,2,3,4 are the numbers identifying the four pins visible in figure 4.1 and d is the distance between the pins.

Finally, the two magnetic coils are necessary for the radial component of the magnetic field, B_r, and its normal component B_n, which, again similarly to E_n, eventually becomes the toroidal component B_t. To be more precise, no absolute values of the magnetic field are measured, but rather flux fluctuations in time, so that the unit of measurement is volt per second.

Apart from the complex probe, a triple probe is also used in order to measure the local electron temperature and density, T_e and n_e, in the edge plasma. It is independent on the complex probe and it situated towards the downstream of fast electrons. It has the same poloidal cross section, and consists of four tungsten pins too. In order to obtain accurate plasma parameters, there is a calibration of the optical links.

Some examples of the typical values for T_e and n_e [87] are respectively $T_e = 17 \pm 3$ eV and $n_e = (0.4 \pm 0.1) \times 10^{19} m^{-3}$ at a distance from the core given by r/a=0.95, and $T_e = 29 \pm 3$ eV and $n_e = (0.8 \pm 0.1) \times 10^{19} m^{-3}$ at r/a=0.92. In the core region, instead, the temperature T_{e0} (measured by a Thompson scattering system) reaches a maximum of 930 ± 280 eV, and it was observed [85] to increase with the plasma current I_p till a critical value (I_{crit}) at which it saturates. In TPE, T_e is large and so is the Magnetic Reynolds number S, which depends strongly on it [85]: it can be defined as the ratio between τ_R and τ_A, which are respectively the resistive and Alfvén timescales, and it results to be equal to $2.18 \times 10^7 I_p[MA] \langle T_e \rangle [keV]^{1.5} \langle n_e \rangle [10^{19} m^{-3}]^{-0.5}$. Also the streaming parameter, i.e. the normalized electron drift velocity, which is $\xi_d = v_{ed}/v_{eth}$ (where v_{ed} and v_{eth} are the electron drift and thermal velocities) is high, of the order of 1.49 $\times 10^{-2} a[m]^{-2} I_p[MA] \langle n_e \rangle \times [10^{19} m^{-3}]^{-1} \langle T_e \rangle [keV]^{-2}$. Such an high ξ_d in principle is able to drive the runaway electrons which are typically observed in the edge region. As far as the length dimensions in the TPE database are concerned, the electron and ion Larmor radii normalized to a correspond respectively to ρ_e^* between 3×10^{-4} and 3×10^{-3} and ρ_i^* between 3×10^{-2} and 3×10^{-1} in units of $\langle T_e \rangle [keV]^{0.5} I_p[MA]^{-1}$. The shot-averaged value of the plasma-β for the poloidal field lies between 0.05 and 0.3.

4.1.2 RFX-mod RFP device

RFX-mod can operate as a RFP device. It is a toroidal configuration with major radius R=2 m, and minor radius a=0.459 m [92]. It has been operated at a plasma current I_p in the range 0.2-2 MA with on-axis electron temperature T_e between 200 and 1000 eV and electron density n_e of (2-10)$\times 10^{19}$ m^{-3}. The discharge duration reaches 0.4 s. The plasma is ohmically heated with a loop voltage of 20-50 V, needed to sustain the poloidal currents through the dynamo process. The operating gas is hydrogen. The magnetic boundary corresponds to a thin Cu shell, characterized by penetration time of the vertical field of 50 ms. The system consists in 192 saddle coils which cover the whole area to efficaciously control the MHD activity related to the radial field.

The electrostatic and magnetic probes are located inside the vacuum vessel, in the so-called Integrated System of Internal Sensors (ISIS), able to acquire high-frequency data and study the fluctuations of the various quantities at the plasma edge. Similarly to TPE-1RM20, the time derivative of the magnetic field is measured. The first wall of the machine is covered by graphite tiles, behind whom the probes are distributed in the toroidal direction and on two 48-coils arrays in correspondence of two opposite poloidal locations.

The signals were acquired in experimental conditions of low I_p, i.e. lower than 400 kA, using a probe called U-Probe (figure 4.3) which is inserted into the vacuum chamber till $r/a \approx 0.9$. The probe consists of two 5 cm toroidally spaced boron nitride cases containing 40 electrostatic pins each combined in eight triple probes of 5 pins. In addition, each of the case contains a radial array of 7 three-axial magnetic coils measuring the three components of the magnetic field. The U-Probe allows for a high frequency estimate of the plasma potential, electron density and temperature [81].

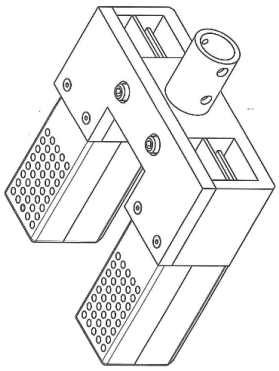

Figure 4.3: Schematic image of the U-Probe in the RFX-mod device.

4.2 Available data and signals

The available data from the TPE-1RM20 device consist in a total of nine signals acquired with a sampling frequency of 2 μs [87]. The data are collected in shots divided into windows containing 100 time points (200 μs) each. Every window is separate and statistically equivalent, and they are associated to the same time interval so that each sample is characterized by similar experimental conditions. The total number of windows is N_{sam} = *number windows per shot* $\times$ *shot number*. To each window the linear trend is subtracted, and then they are multiplied by the Hanning window (A=3/8). The available kinds of shots containing the signals are divided into four independent datasets:

1. At high theta
2. At high density
3. At high current
4. Additional "ground" dataset

By "theta" the plasma Θ parameter 2.29 is meant. In table 4.1 some estimates are shown of the principal plasma parameters: the plasma current I_p, the reversal parameter F 2.30, and the Θ parameter (explained in §2.1.2). In figure 4.4, the typical collected signals are shown.

High theta	High density	High current	ground
$I_p = 52 \pm 3$ kA	$I_p = 61 \pm 2$ kA	$I_p = 80 \pm 4$ kA	$I_p = 52 \pm 4$ kA
$F = -0.35 \pm 0.2$	$F = -0.2 \pm 0.08$	$F = -0.15 \pm 0.08$	-0.22 ± 0.05
$\Theta = 1.85 \pm 0.15$	$\Theta = 1.70 \pm 0.075$	$\Theta = 1.62 \pm 0.05$	$\Theta = 1.70 \pm 0.06$

Table 4.1: Average values for the most useful plasma parameters: the plasma current I_p, the reversal parameter F 2.30 and the Θ parameter 2.29.

We can see that the plasma current (up on the left) can be assumed constant between 1.5 ms and 4 ms and so an average value can be established. The interval covered by the flat-top phase of I_p is the reference time interval for all the other samples. The signal obtained from the EEA describes the electron motion, and a low-pass filter (from the scipy package) at 250 kHz was later applied to it.

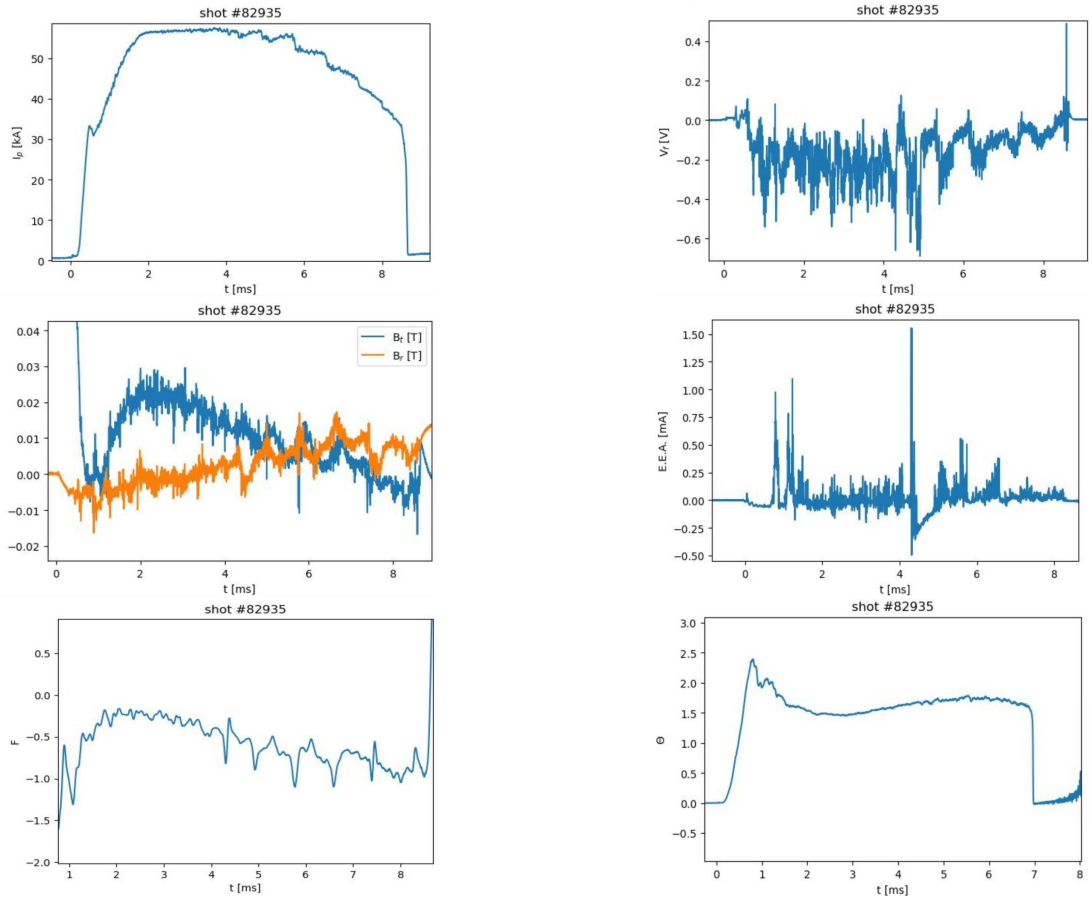

Figure 4.4: Example showing how the signals collected by TPE-1RM20 appear. First line: plasma current I_p and floating potential V_f, second line: radial and toroidal components of the magnetic field (B_r and B_t) and EEA signal, third line: reversal parameter F and Θ parameter.

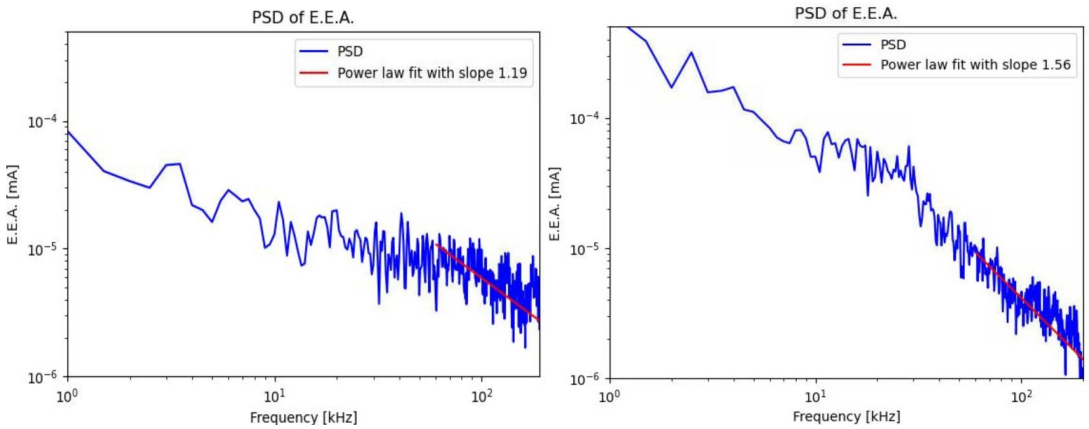

Figure 4.5: Power spectra of the complete signals of the EEA obtained combining all signals contained in the high theta dataset and high density dataset. A power-law trend results.

As mentioned previously, the signals obtained from RFX-mod were obtained in low-current discharges with a value of the safety factor q 2.33 at the boundary around -0.006. This corresponds to a multiple helicity (MH) regime, which was theoretically discussed in paragraph §2.2.3. The sampling frequency corresponds to 2 MHz, and the measurement bandwidth is between 300 and 400 kHz. The reversal parameter F 2.30 lies between -0.3 and -0.05. The current j_p parallel to the magnetic field and the signals of the radial and toroidal magnetic field as derived from the pick-up coils embedded into the U-probe are considered. They have been previously numerically integrated so that this analysis was performed on the integrated data.

The power spectrum has been extrapolated and fitted in the range of frequencies of interest, namely after the MHD mode and the subsequent drop. The power spectral density (PSD) of the E.E.A. current is shown for comparison at high theta and high density in figure 4.5. The PSD of the toroidal and radial magnetic field was plotted with respect to the ratio f/Ω_{c_i}, where f is the scale frequency in kHz, and Ω_{c_i} the cyclotron frequency of the ions $\Omega_{c_i} = \frac{|q_i|B}{2\pi m_i}$, where B is the poloidal magnetic field at the plasma surface which in the RFP plasma of TPE-1RM20 is equal to 0.13 T [85], which leads to $\Omega_{c_i} = 1$ MHz. The same was done for the magnetic field signals of RFX-mod, whose plasma is characterized by $\Omega_{c_i} = 2.3$ MHz . The results are shown in figure 4.6. In all these cases, the PSD reveals a power-law trend, as it can be deduced from the linear fits in the logarithmic plots in figures 4.6. The slope is also indicated. The range of values f/Ω_{c_i} fitted by the power-law is nearly the same for TPE and RFX, and it can be observed that in the TPE spectra there is a stronger MHD activity which modifies the energy cascade at higher frequencies. In particular, a large amount of MHD modes is present in the power spectrum around 40 kHz.

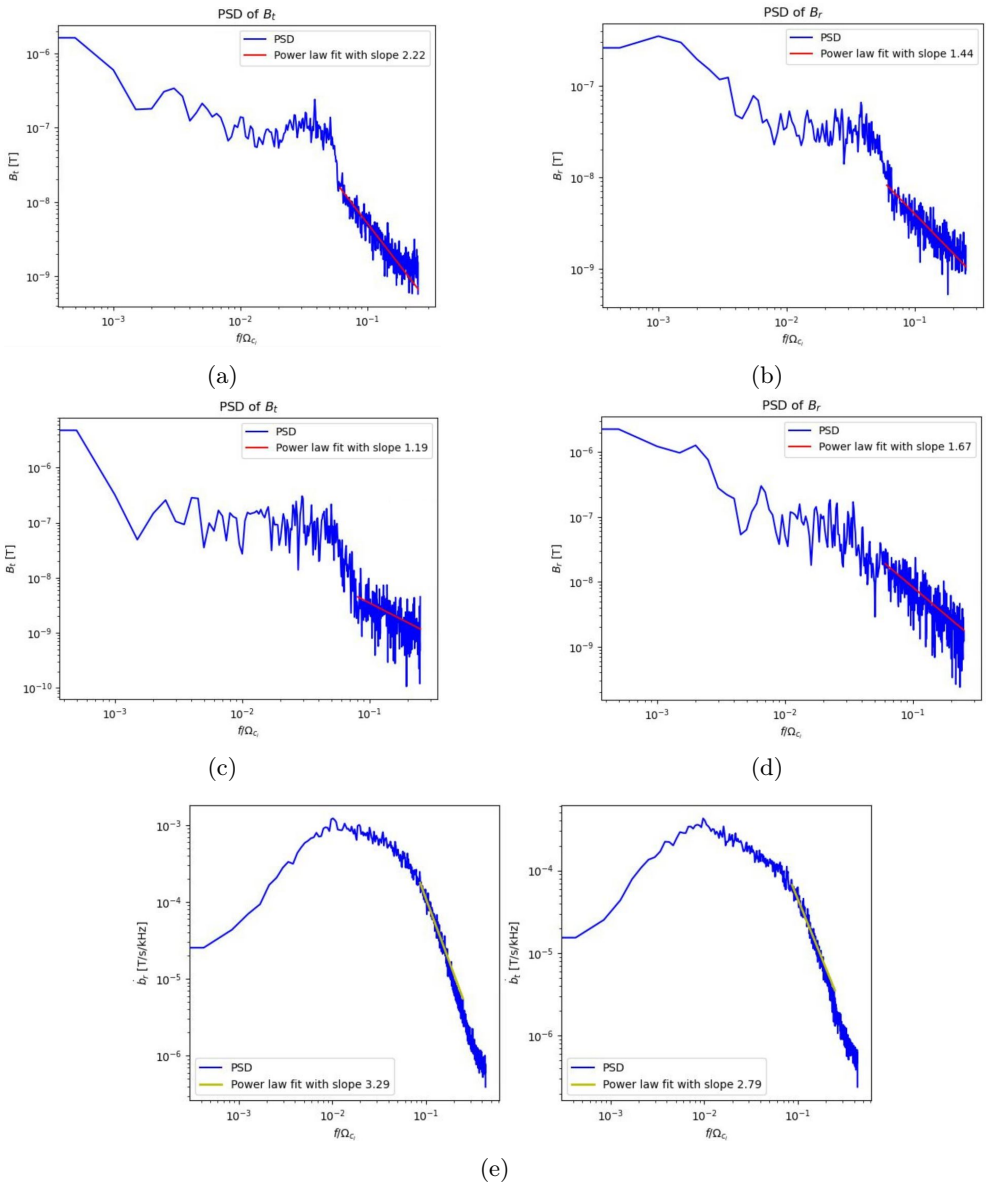

Figure 4.6: Power spectra of the signals of the magnetic field measured by the two experiments: complete signal of the toroidal and radial magnetic field obtained with TPE-1RM20 at high theta 4.6a 4.6b, at high density 4.6c 4.6d, and the numerically integrated signals of the magnetic field obtained with RFX-mod, radial and toroidal component 4.6e.

4.3 Data analysis and discussion

4.3.1 LIM method and probability distribution function

The first analysis focused on the single shots of the signal measured by the EEA of TPE-1RM20, which was appropriately filtered as mentioned before. The Local Intermittency Measure (LIM) (see definition 3.6) technique was implemented as explained in §3.2: the flatness factor F 3.7 is used as indicator of intermittency and the selected events are those regions (where the signal overcomes a determined threshold) whose effect is to make the Probability Distribution Function of the signal fluctuations (represented by the wavelet coefficients) strongly non-gaussian [59]. The implemented algorithm allows to localize in time the peaks (or valleys) on the signal for a given sampling frequency, which indeed correspond to increased energies of the collected electrons caused by the non-thermal acceleration of the particles (eventually due to reconnection events). Three characteristic time scales were chosen, all within the region of power law decay of the EEA signal: 50, 100 and 150 kHz, which in units normalized to the ion cyclotron frequency Ω_{c_i} correspond respectively to 0.05, 0.1 and 0.15. It is possible to plot the time instants associated to the fluctuations at the corresponding scale which have been identified as non-gaussian fluctuations versus a time basis which is the same as that of the signal. Figure 4.7 gives an example of the identified maxima: the continuous lines indicate the occurrences of the selected fluctuations, namely the intermittent events.

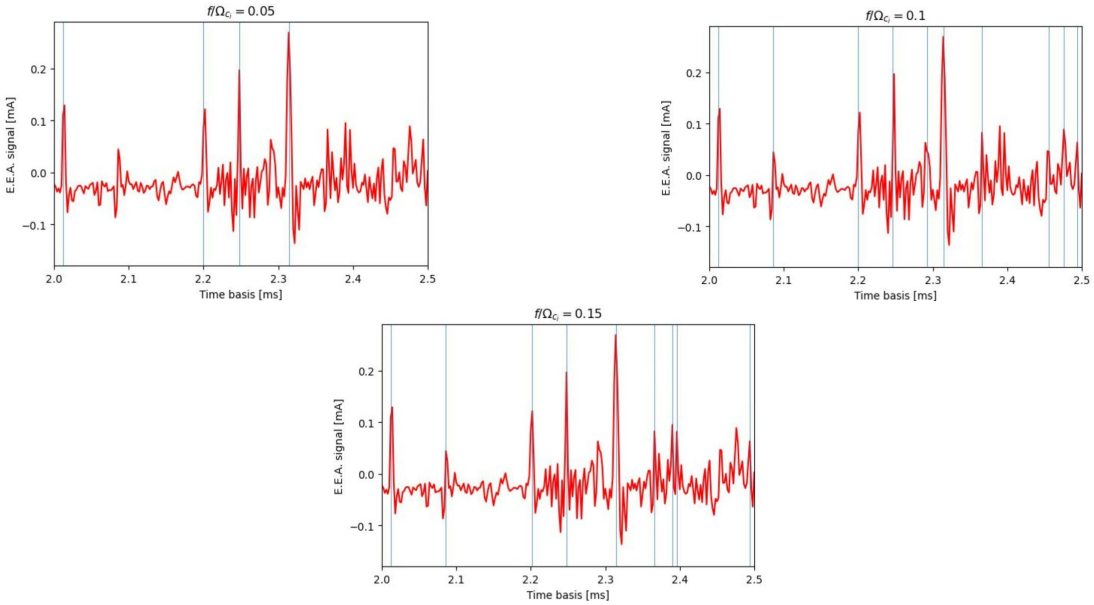

Figure 4.7: Identification at three sampling frequencies of the intermittent structures resulting as maxima on the EEA signal, implementing a LIM code. The occurrences of intermittent events are marked with continuous lines.

As explained in paragraph §3.2, studying the probability density function (PDF) of fluctuations gives valuable insights about the properties of intermittency. Therefore, the PDF of the normalized fluctuations of the form $\frac{\delta\psi - \langle\delta\psi\rangle}{\sigma_{\delta\psi}}$ of the perpendicular magnetic field $\delta b_\perp$, radial component, was computed using the Castaing's model 3.10 on the data of both TPE-1RM20 and RFX-mod, as done also in [81], and it is shown in figure 4.8. In this case $\sigma_{b_\perp}$ is the width

of the distribution. We can observe how towards higher frequencies (maximum scale in the plots 4.8) the deviations from gaussianity are larger with enhanced tails of the distributions, consistent with the typical effects caused by intermittency and with previous results listed in section §3.2 (see for example figure 3.6). In order to further characterize the intermittency properties and see how the energy cascade is at different scales, λ^2 (see equation 3.8) was plotted with respect to the timescale τ in the cases at high theta and density of TPE-1RM20 and RFX-mod displayed in figure 4.9. The results are consistent for RFX-mod and TPE-1RM20 at high theta showing a power-law relation of type $\lambda_\tau = \mu\tau^{-\gamma}$, whereas in the case at high density no homogeneous scaling is found: this might be related to the presence of MHD modes visible in figure 4.6 which influence the energy cascade at wider tails. Unfortunately, the TPE device is limited in the frequency range, and it is not possible to attain statistics at frequencies as high as in the case of RFX, making the modification of the behaviour of the energy cascade hard to understand at smaller (time) scales. However, the very fact that the PDF alters at smaller scales suggests additional evidence of the intermittent nature of the system.

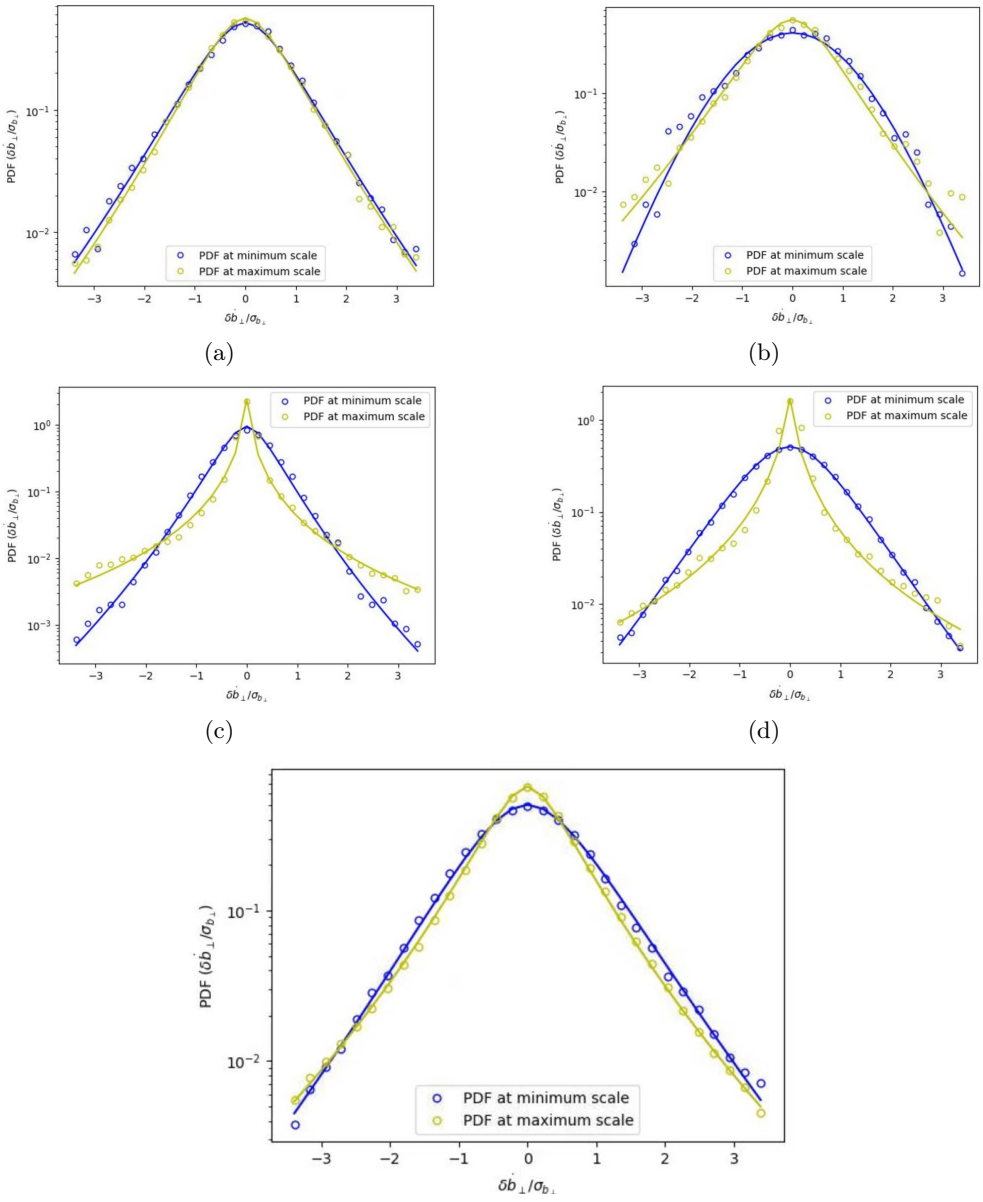

Figure 4.8: PDFs of the normalized fluctuations of the radial magnetic field measured by TPE-1RM20 at high theta 4.8a, high density 4.8b, high current 4.8c and for the ground dataset 4.8d, and RFX-mod 4.8e.

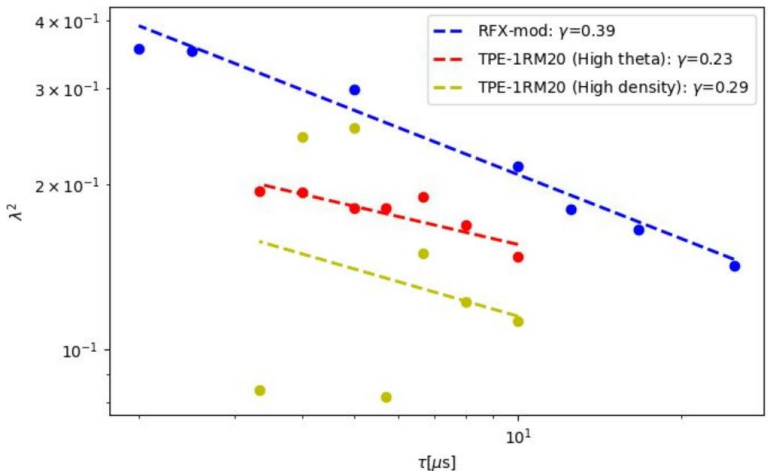

Figure 4.9: Scaling of λ^2 at different timescales τ fitted by a linear trend for the radial magnetic field fluctuations in the case of TPE-1RM20 and RFX-mod.

4.3.2 Conditional average sampling

The aforementioned code implements the so-called conditional average sampling (c.a.s.), which is a tool to separate the coherent component of a fluctuating signal from the random component [71]. By conditional averaging, it is possible to extract the average shape of a burst, assuming that all the intermittent events in a signal have a similar shape. The identification of coherent structures is possible imposing a specific condition on the amplitude of the fluctuation. After the condition is imposed on the whole time series, N identified events are obtained at times t_j for $j = 0, 1, ..N-1$. Then, a segment $\tilde{X}(T_j)$ is selected around each of the selected points, i.e. in the range $T_j \in [t_j - \tau, t_j + \tau]$ [71], where τ is of the order of the correlation time of the signal [77]. In the end, the coherent part of the signal is obtained by averaging on these segments. Practically, this translates into using two probes which record simultaneously two time series: a reference probe (RP) kept at a fixed position, and a movable probe (MP) scanning the area of interest [77]. The identification of the structures occurs (imposing the aforementioned condition) on the time series of the RP, and the relative segment is extracted out of the time series of the MP. The sample sequences are independent one from the other as long as $t_{j+1} - t_j < 2\tau$.

Initially, the c.a.s. was made on the single signals of the EEA and the magnetic field of TPE-1RM20. In particular, it was necessary to detrend the signal of the magnetic field before the procedure. The code returns, for the chosen scale frequency, the adimentional c.a.s. coefficients building the average shape of the fluctuations, resulting as a peak illustrated in figure 4.10. A shot at high theta is given as an example. Logically, as the sampling frequency increases, the time interval to be analyzed decreases and the peaks become steeper.

After this, the amplitude of the detected intermittent structures was computed to see how it changes with the different frequencies appearing in the plots 4.10. The results are shown in figure 4.11. The amplitude was calculated subtracting from the maximum value an average of the first ten minimum values of the c.a.s. coefficients. Also the errors were computed using the standard theory of the error propagation, starting from the errors on the c.a.s. coefficients

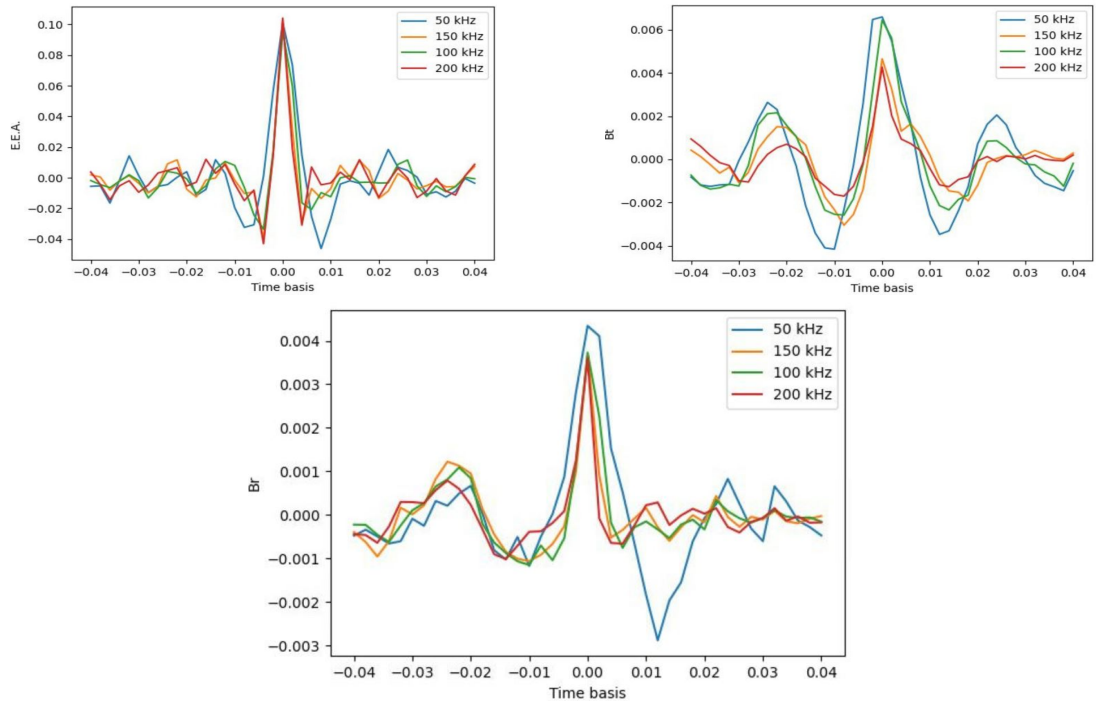

Figure 4.10: Results obtained after the conditional average sampling (c.a.s.) of the single signals of the EEA and toroidal magnetic field (above) and radial magnetic field (below) for different sampling frequencies. On the y and x axis respectively the adimentional c.a.s. coefficients and the associated time basis. These correspond to a high theta shot.

given by the code. While no clear trend can be recognized on the scaling of the EEA amplitude (4.11a), both components of the magnetic field (4.11b, 4.11c) exhibit a decreasing amplitude with the scale, with a sort of saturation above 100 kHz.

Following these results, the same analysis involving the conditional average sampling and the LIM method was applied for a multiple signal containing the EEA signal, plus the four available signals of the magnetic field (including the measurements of the two perpendicular components by both separated coils, indicated with subscripts 1 and 2), plus the four signals of the floating potential (obtained from each probe indicated with subscripts 1,2,3,4). To increase the statistical significance all the different shots have been considered together as a part of a single ensemble of a stationary process. Again the same code contains a function which makes the c.a.s. of multiple signals by taking as reference a signal, which in the case of TPE is the signal of the E.E.A. current, so that it is possible to verify how all the other signals behave in the same time interval. First, the c.a.s. of the magnetic field signals is plotted at different sampling frequencies (written in units of kHz in the titles of the plots) in figure 4.12. In this case the structures are valleys: we assist to a minimum in the toroidal component of the magnetic field at the edge. As it can be seen in the figure, the relevant results are those obtained from the magnetic coil n°2. Another thing to be noted is that the two perpendicular components are $\pi/2$ out of phase: when there is a minimum of B_r, there is a maximum variation of B_t and vice versa. Moreover, it can be observed that as the frequency increases, the two components of the magnetic field seem to be less out of phase. The fluctuating components can be better visualized in figure 4.13 zooming on a time interval around zero. Such a $\pi/2$-phase relationship

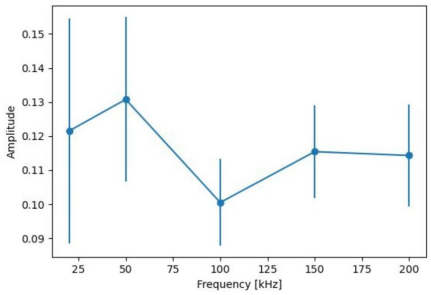

(a) EEA

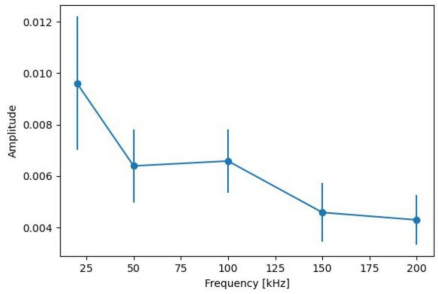

(b) Toroidal magnetic field B_t

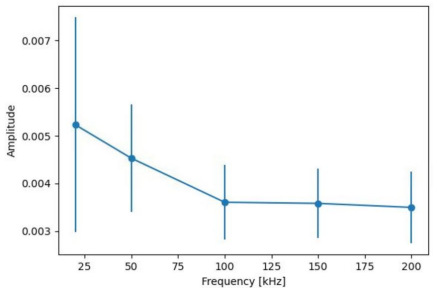

(c) Radial magnetic field B_r

Figure 4.11: Amplitudes of the c.a.s. structures plotted with the frequency. Results obtained for the single signals of the EEA (4.11a), toroidal magnetic field (4.11b), and radial magnetic field (4.11c).

is typical for current sheet-like structures.

In particular, the current topology can be inferred looking at the hodogram, namely the trajectory of the two perpendicular field components in the (B_t, B_r) plane (in this case) during the passage of a current filament [80]. The hodogram exhibits a closed orbit having the shape of a cardioid if the field-aligned current is bipolar, and of an ellipse if the current is monopolar, which is common for magnetically-confined plasmas. The signals in figure 4.13 are pretty similar to those in [80], and therefore an elliptic shape would be expected. In the case of TPE, the resulting hodograms are shown in figure 4.14 for a time interval centered in zero (i.e. around the main valley structure shown in figure 4.13). We cannot see any ellipse, which is the ideal solution to numerical simulations, but closed orbits in the plane (r, ϕ) are found anyway. The non perfect elliptical shape could be due to the fact that we are considering a current structure moving in a spurious plane, i.e. not perfectly aligned with respect to the considered coordinates (r and ϕ), causing the presence of a spurious component in the current trajectory leading to a distorted ellipse. Different is the case of RFX-mod, figure 4.15: the hodogram seems to have a cardioid-like shape with the cusp at the origin suggesting the shape could be associated to a bipolar current distribution structure [80]. It is worth clarifying that, since, as explained previously, the RFX signals are already numerically integrated, their derivative has been considered in the hodograms to make a fair comparison with the TPE case. Conversely, it was not possible to integrate the TPE signals, because of the missing information about the effective area of the probes.

Now, the real target of this work is actually to demonstrate that at the same instant of time we have:

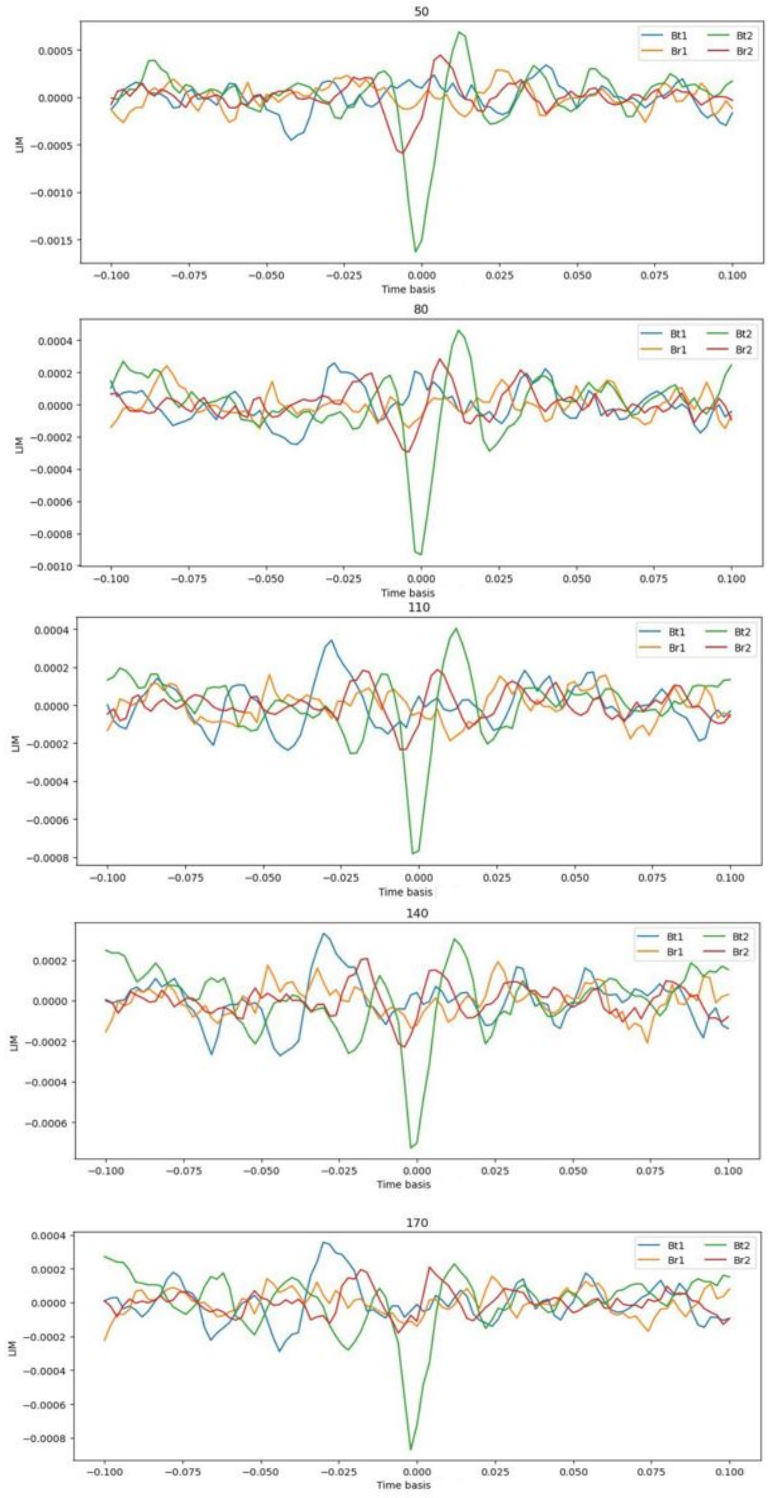

Figure 4.12: Intermittent structures resulting as valleys from the c.a.s. of the multiple signal of the magnetic field (toroidal and radial components from both coils) for different sampling frequencies in kHz specified in the titles of the plots. On the y and x axis respectively the adimentional LIM coefficients and the associated time basis.

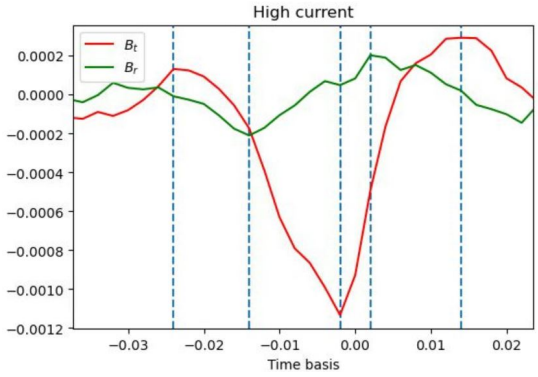

Figure 4.13: Phase relationship between toroidal and radial field. The picture shows a zoom on the magnetic fluctuations: the dashed lines indicate the time instant of minimum/maximum of the field components.

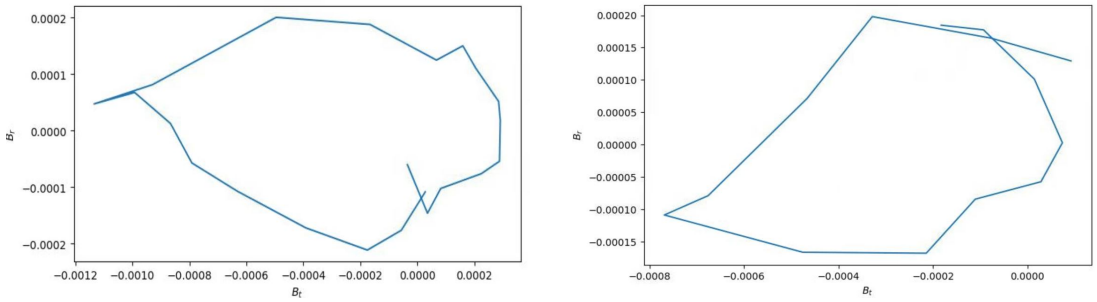

Figure 4.14: Hodograms of radial and toroidal magnetic field fluctuations (c.a.s. coefficients) of TPE-1RM20 at high theta and high current respectively.

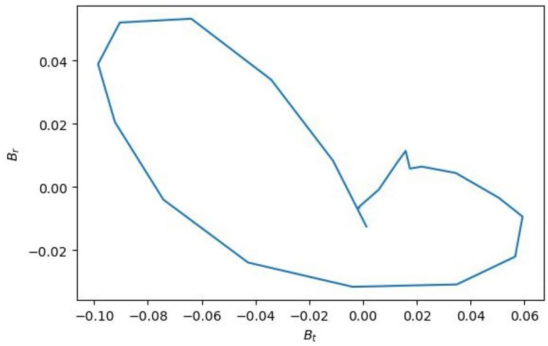

Figure 4.15: Hodogram of radial and toroidal magnetic field fluctuations (c.a.s. coefficients) of RFX-mod.

1. The fluctuation of the two magnetic field components as obtained above;
2. An electron acceleration, which can be inferred from the EEA signal, and results as a current discharge, i.e. as a positive peak centered in zero;
3. A variation of the electric field, which can be inferred from the measurements of the floating potential: if it exhibits a rapid variation, this corresponds to a peak in the electric field.

Therefore, a comparison was made among the conditional average of the EEA signal, magnetic field (B_t and B_r), and the four available shots of the floating potential V_f of TPE-1RM20. In addition, an analogous analysis was carried out on the signals of the parallel current j_p and magnetic field of RFX-mod. The reason is that there is no possibility to measure in the same experiment both the electron acceleration (possible with the EEA of TPE-1RM20) and the parallel current (with RFX-mod), and therefore a comparison between the statistics from the two complementary devices is needed to understand if a correspondence actually exists between the electron acceleration processes and the increase of the parallel current.

Let us start by showing the results obtained from the statistics regarding TPE-1RM20 and the EEA: in figure 4.16 the LIM coefficients building the resulting intermittent structures of the multiple signals of all the quantities are shown in the case at high theta. Again, the same three sampling frequencies (in fractions of Ω_{c_i}) were considered. The obtained results provide a confirmation of the existence of a correspondence among the magnetic fluctuations in the form of current sheets (as shown in figure 4.13), the acceleration of the electrons and the variation of the electric field. In addition, analogous results were achieved considering also the high density and "ground" datasets, which are shown respectively in figures 4.17 and 4.18. In the latter case, the more evident magnetic fluctuations are measured by coil n°1, differently from the previous cases, and the radial magnetic field from coil 2 B_{r2} was amplified in order to see its very small variations with more clarity. Anyway, in all these cases we can see a positive peak in the EEA current, a valley in the magnetic fluctuations, and a rapid variation in the floating potentials. However, when analyzing the case at high current, a kind of peculiar situation is found, shown in figure 4.19. We cannot assert that there is a correspondence with the magnetic fluctuations at the time instant of the current discharge: there is a sort of minimum in the toroidal component B_{t1}, but the same does not apply for B_{t2} and in general it cannot be said that there is a valley structure. Also in this case the B_{r2} component was amplified in the plot.

Finally, as mentioned previously, the c.a.s. was made on the multiple signal composed by the radial and toroidal magnetic field measured by RFX-mod with the parallel current j_p as reference signal. The results are shown in figure 4.20. The same three scales were considered. It is worth repeating that, in the case of RFX-mod, the signals have been numerically integrated, and therefore the resulting shape visible in figure 4.20 is consistent with the valleys appearing in the case of the TPE signals in figures 4.16, 4.17 and 4.18, which in this case are connected to a peak in the parallel current, and so we can assume again the presence of a $\pi/2$ phase shift between the toroidal and radial component of the magnetic field. These results confirm that indeed there is a correspondence between the electron acceleration and the increase of the parallel current, associated to the presence of current sheets.

Successively, in the case of TPE-1RM20, the amplitude of the intermittent structures resulting from the c.a.s. of the multiple signals of the EEA and magnetic field (considering only

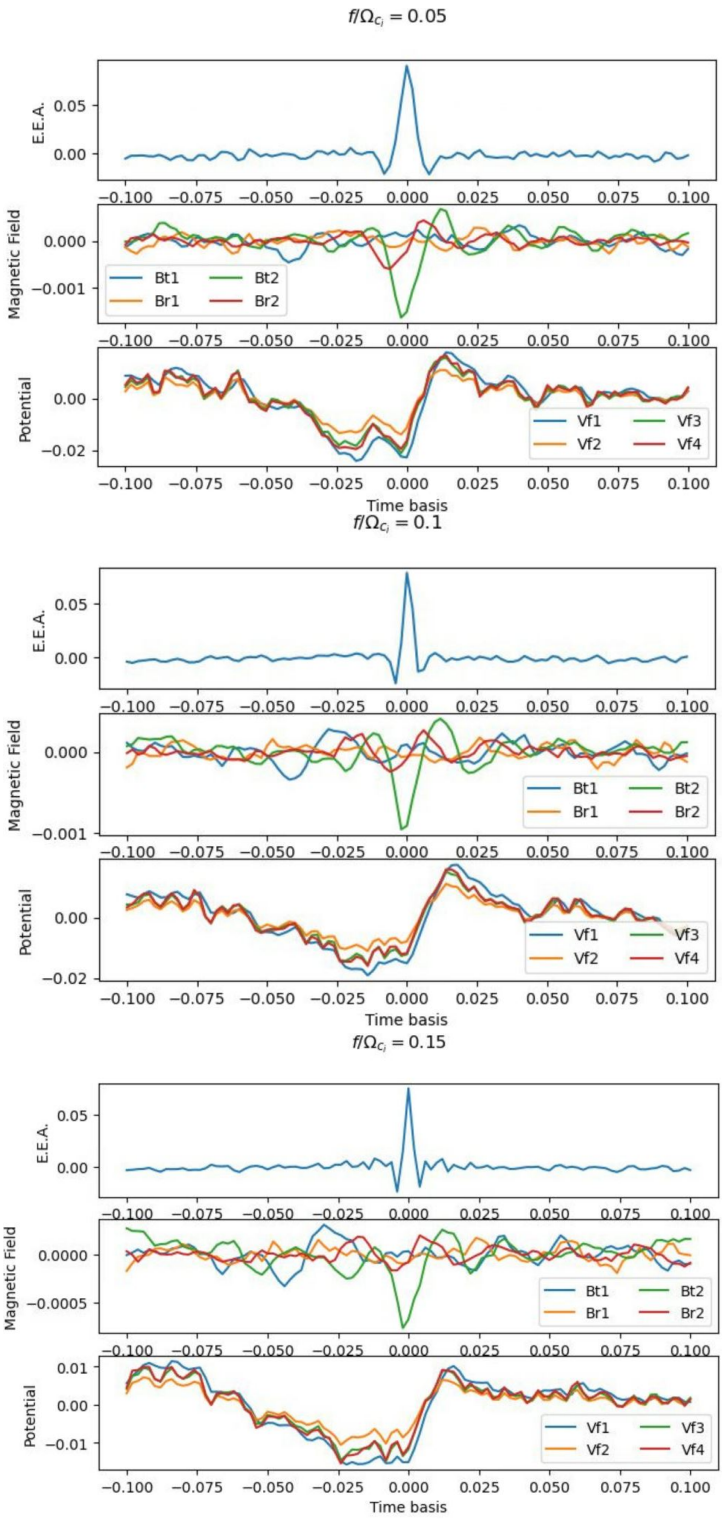

Figure 4.16: Intermittent structures resulting from the c.a.s. of the TPE multiple signals of the EEA, magnetic field (toroidal and radial component B_t and B_r by both coils 1 and 2), and floating potentials $V_{f[1,2,3,4]}$ for different sampling frequencies [kHz] specified in the titles of the plots. On the y and x axis respectively the adimensional LIM coefficients and the associated time basis. This is the case at high theta.

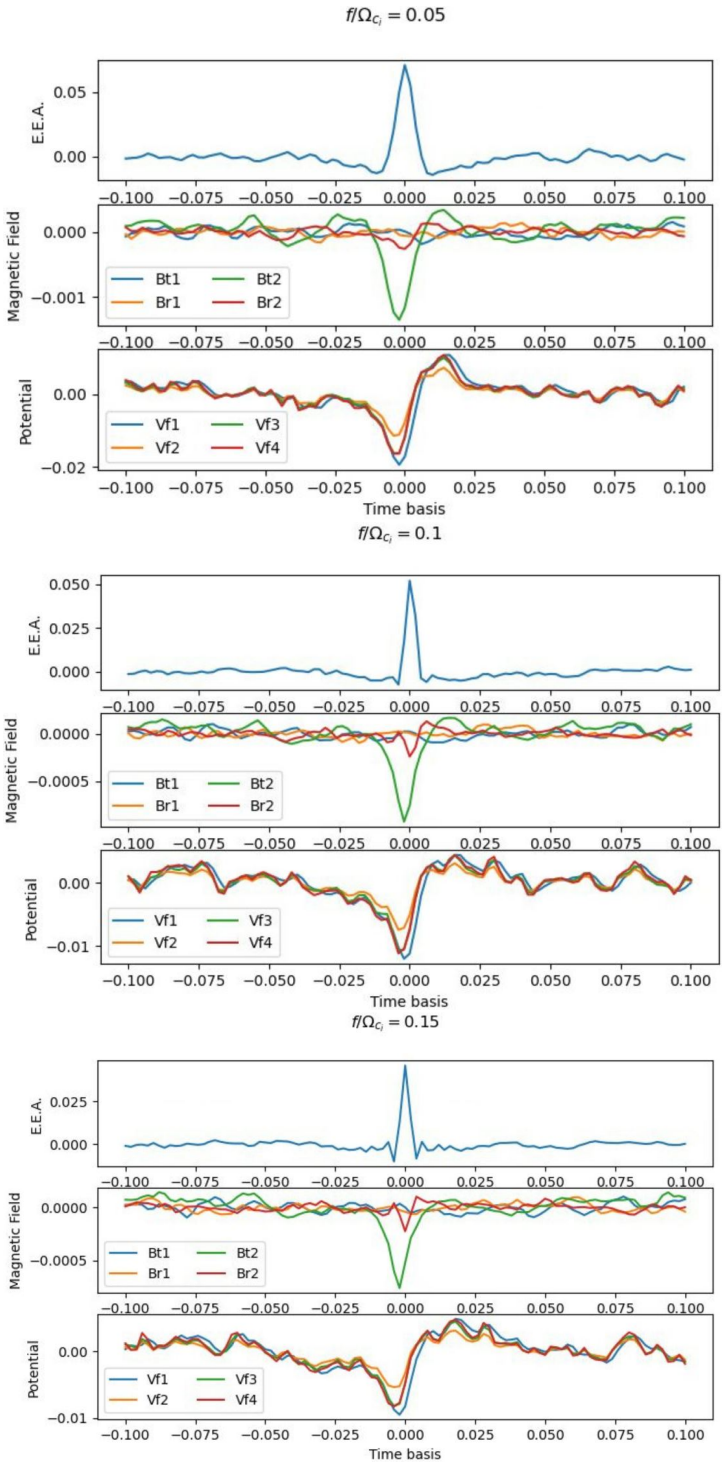

Figure 4.17: Intermittent structures resulting from the c.a.s. of the TPE multiple signals of the EEA, magnetic field (toroidal and radial component B_t and B_r by both coils 1 and 2), and floating potentials $V_{f[1,2,3,4]}$ for different sampling frequencies [kHz] specified in the titles of the plots. On the y and x axis respectively the adimentional LIM coefficients and the associated time basis. This is the case at high density.

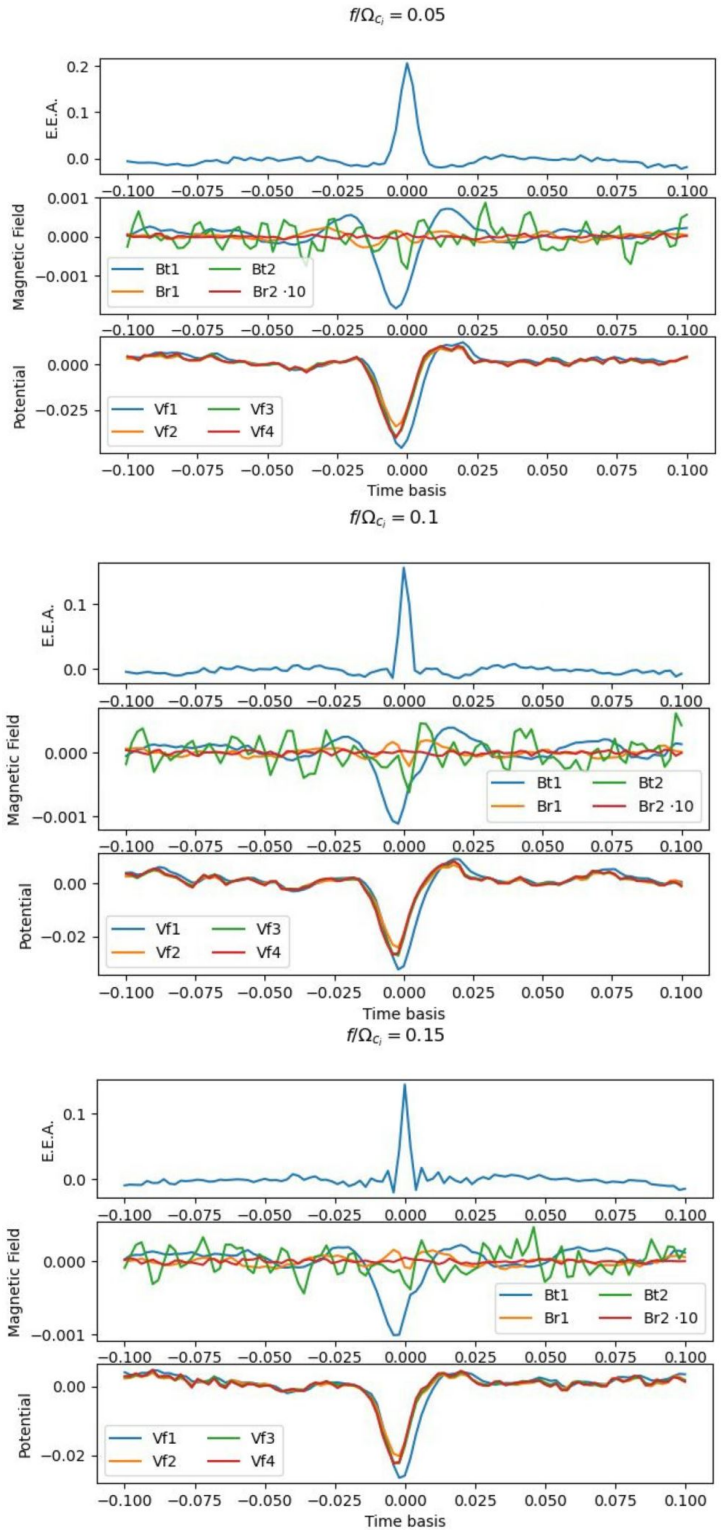

Figure 4.18: Intermittent structures resulting from the c.a.s. of the TPE multiple signals of the EEA, magnetic field (toroidal and radial component B_t and B_r by both coils 1 and 2), and floating potentials $V_{f[1,2,3,4]}$ for different sampling frequencies [kHz] specified in the titles of the plots. On the y and x axis respectively the adimentional LIM coefficients and the associated time basis. This is the case of the "ground" dataset.

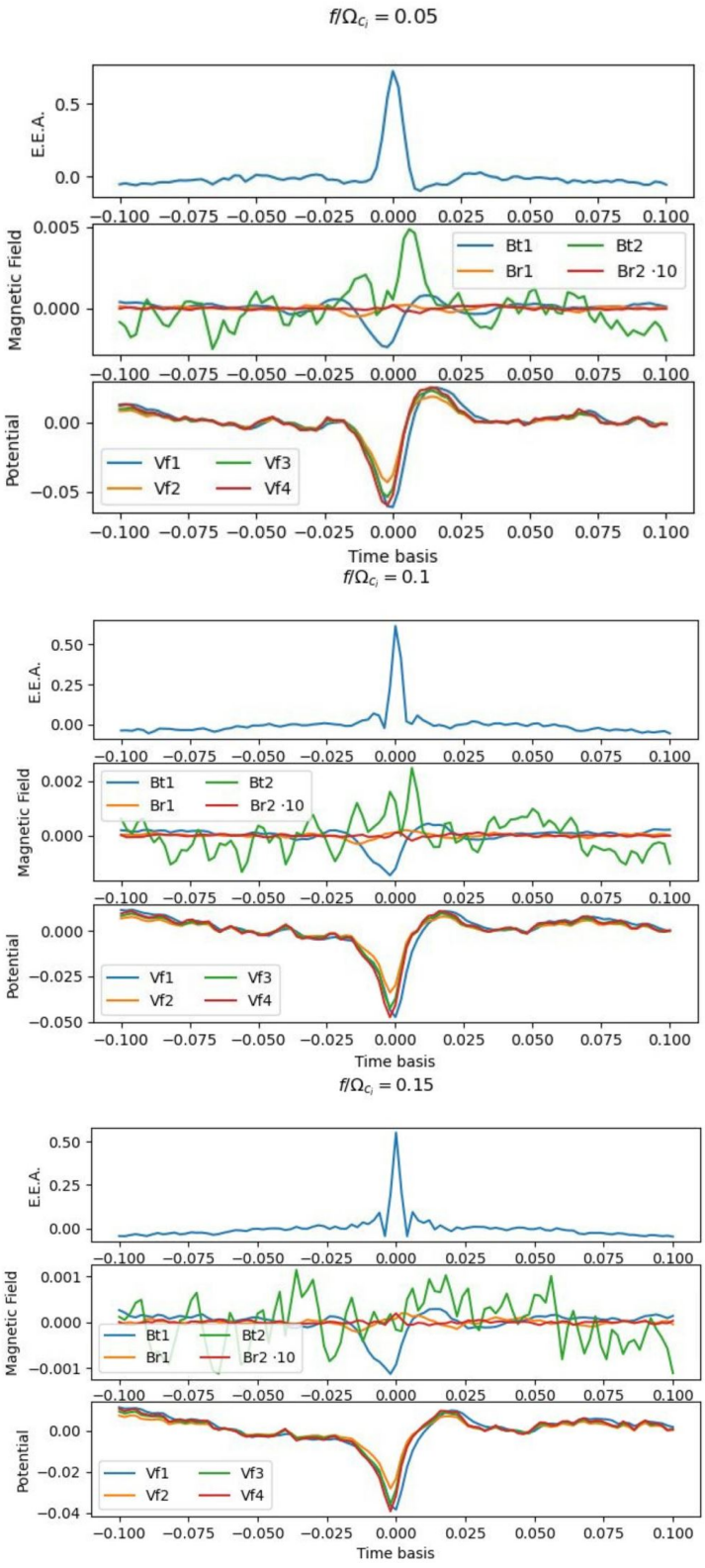

Figure 4.19: Intermittent structures resulting from the c.a.s. of the TPE multiple signals of the EEA, magnetic field (toroidal and radial component B_t and B_r by both coils 1 and 2), and floating potentials $V_{f[1,2,3,4]}$ for different sampling frequencies [kHz] specified in the titles of the plots. On the y and x axis respectively the adimentional LIM coefficients and the associated time basis. This is the case at high current.

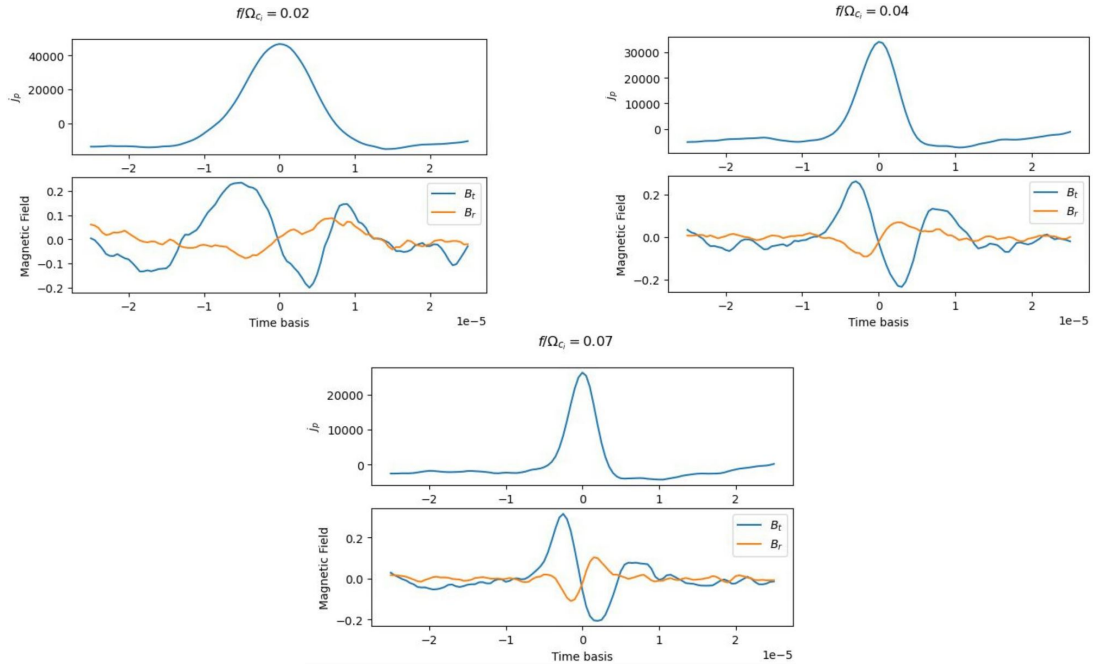

Figure 4.20: Intermittent structures resulting from the c.a.s. of the RFX multiple signal of the parallel current and magnetic field (toroidal and radial component B_t and B_r) for different normalized frequencies. On the y and x axis respectively the adimentional LIM coefficients and the associated time basis.

the signals from one coil) was computed, in the same way as done previously in the single shot analysis. This was done at different sampling frequencies and using all the four types of datasets: high theta (figure 4.21), high density (figure 4.22), high current (figure 4.23), and "ground" (figure 4.24). Looking at the figures, we cannot say there is a linear relation between the amplitude of the structures and the frequency either in the case of multiple signals. The amplitude often decreases at larger frequencies, but this is not even always true, so we cannot state that there is some dependence on the scale.

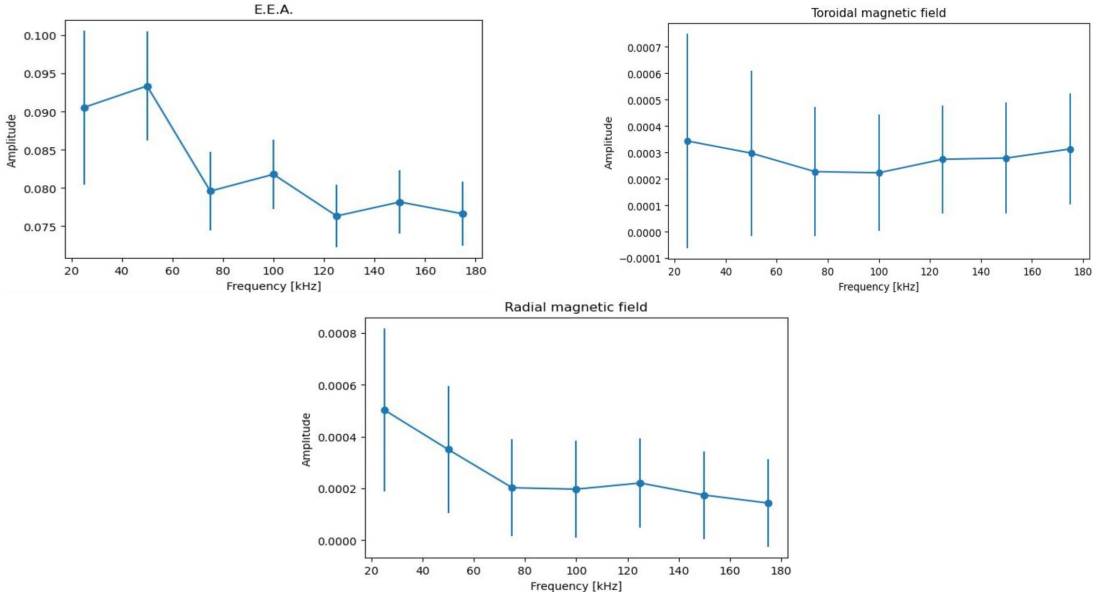

Figure 4.21: Amplitudes of the c.a.s. structures plotted with the frequency. Results obtained for the multiple signals of the EEA and toroidal magnetic field (above) and radial magnetic field (below) at high theta.

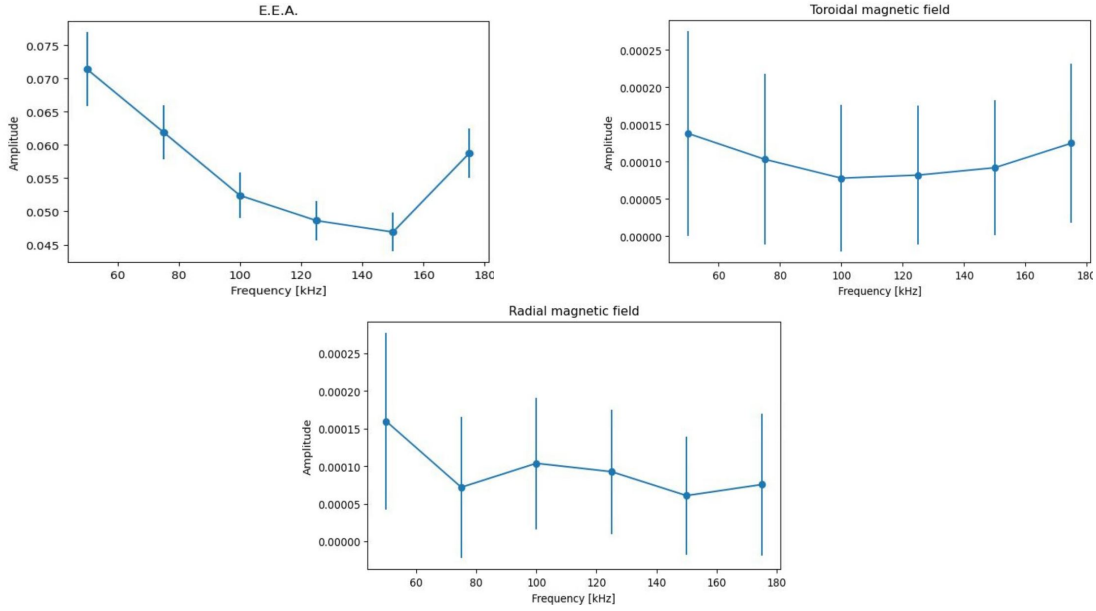

Figure 4.22: Amplitudes of the c.a.s. structures plotted with the frequency. Results obtained for the multiple signals of the EEA and toroidal magnetic field (above) and radial magnetic field (below) at high density.

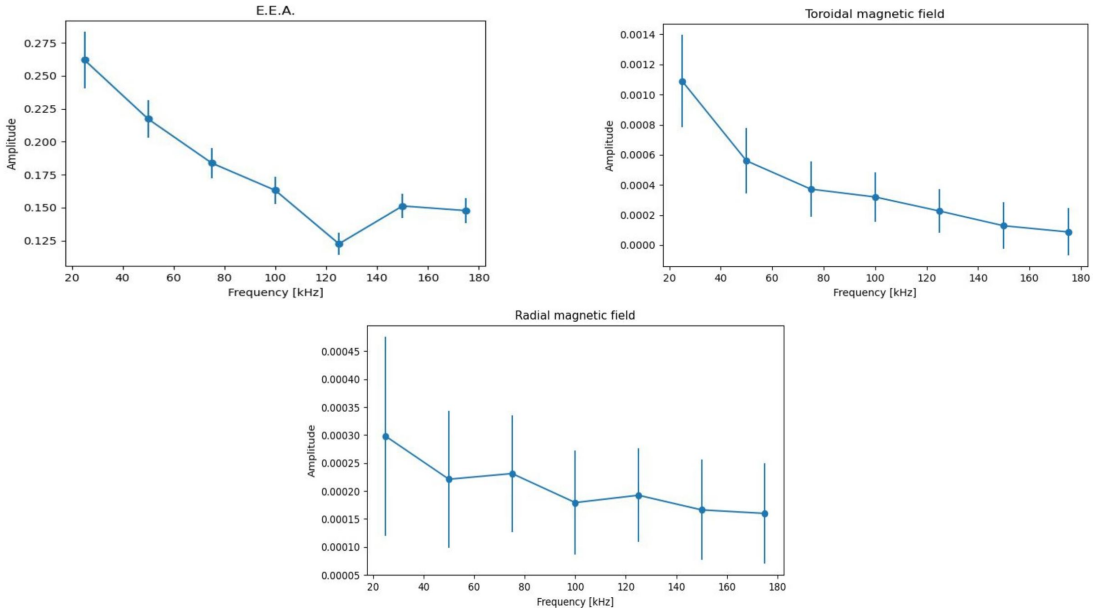

Figure 4.23: Amplitudes of the c.a.s. structures plotted with the frequency. Results obtained for the multiple signals of the EEA and toroidal magnetic field (above) and radial magnetic field (below) considering the "ground" dataset.

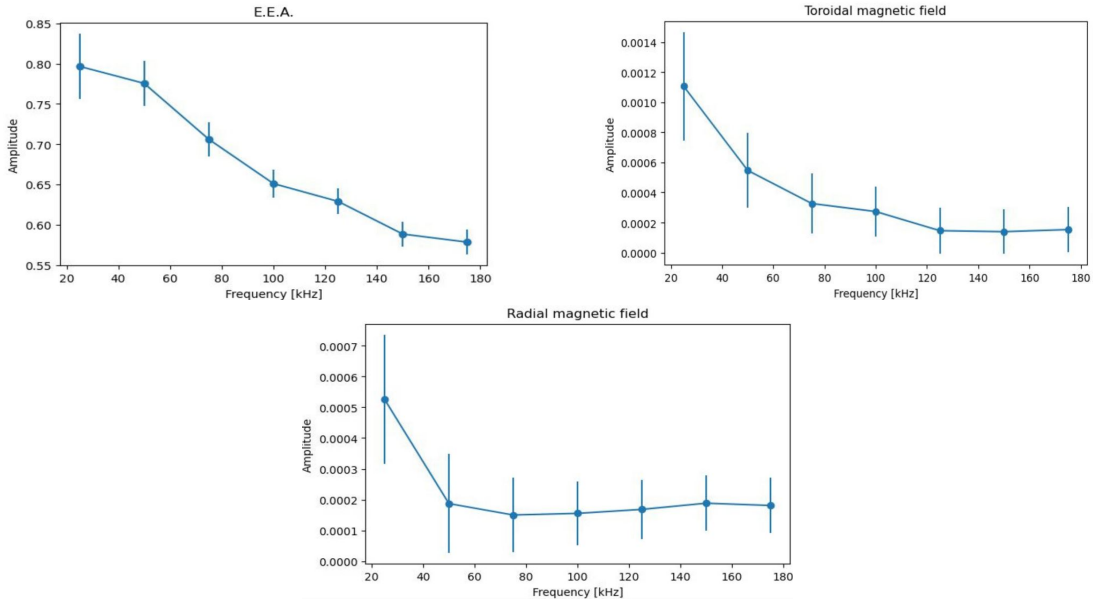

Figure 4.24: Amplitudes of the c.a.s. structures plotted with the frequency. Results obtained for the multiple signals of the EEA and toroidal magnetic field (above) and radial magnetic field (below) at high current.

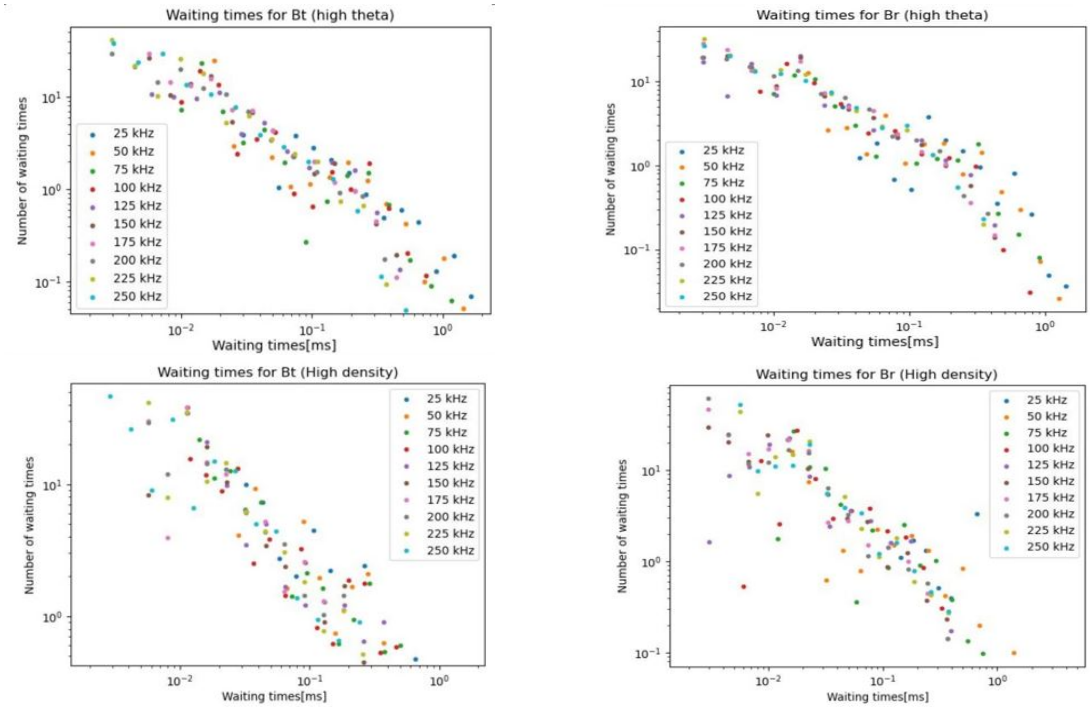

Figure 4.25: Histograms of the waiting times as a function of the frequency. Results obtained for the multiple signals of TPE-1RM20 of the toroidal magnetic field B_t (left) and radial magnetic field B_r (right) at high theta (above) and high density (below).

4.3.3 Study of the distribution of the waiting times

After these results the analysis continued, initially focusing on the TPE signals of the two perpendicular magnetic field components containing all the available high theta (and high density) shots. The scope of this part was to extrapolate the waiting times (using the same LIM code), which are defined as the times running between one detected peak of the LIM and the following one. The waiting times give important insights about the statistical properties of the acceleration process: if their distribution $P(\Delta t)$ exhibits an exponential behaviour, namely is a convolution of an exponential function describing a Poisson process [41], it means that the process is merely random, whereas a power-law trend implies that a memory is present in the process, and suggests that it depends on the frequency, and so it is somehow correlated with time.

The waiting times are organized in histograms to investigate how their distribution changes for different frequencies in order to find some correlation with the scale. The results are illustrated in figure 4.25: a kind of power law distribution is found, whose index changes with the frequency. Therefore, it can be asserted that the waiting times, i.e. the time between consecutive occurrences of the bursting events, depend on the scale. Similar results are obtained in the case of the waiting times between the events detected in the signal of the E.E.A. current measured by TPE-1RM20, and the parallel current j_p measured by RFX-mod, shown in figure 4.26. To better visualize the possible power-law trend a fit for each scale frequency was done and it was found that the waiting times distribution actually follows a power law with an

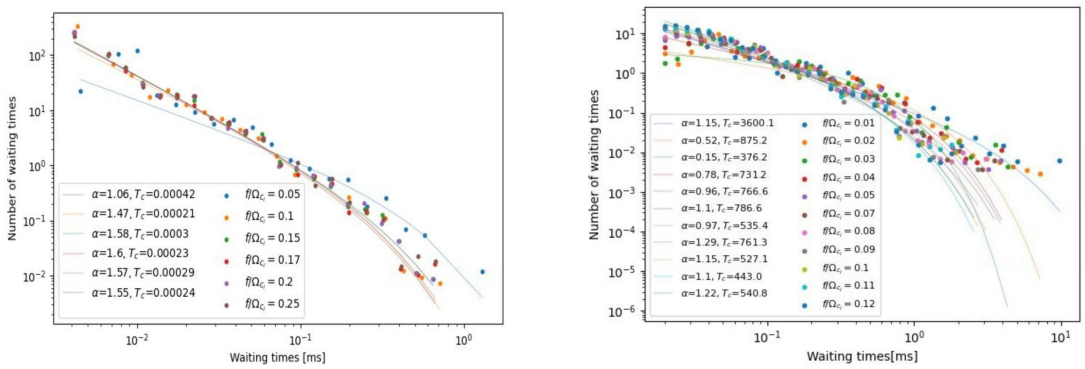

Figure 4.26: Histogram of the waiting times as a function of the frequency. Results obtained for the signal of the EEA measured by TPE-1RM20 (left) and parallel current measured by RFX-mod (right). The distribution was fitted with a power law plus exponential cut-off.

exponential cut-off of the form [81]:

$$P(\Delta t) = A\Delta t^{-\alpha} \exp -\Delta t/T_c \tag{4.2}$$

The slope α of the power law and the cut-off exponent T_c of the scaling are shown too in figure 4.26. The fact that at each time scale the distribution follows the same kind of profile suggests that the statistical properties of the events are similar at any scale (self-similarity in time). Furthermore, additional confirmation of the dependence of the waiting times distribution on the scale has been provided by plotting the variation of the T_c exponent and power-law slope α in the frequency range of the power spectrum affected by the power-law decay, namely at the higher frequencies where turbulence is completely developed. In particular, in figure 4.27, T_c seems to decrease with the frequency, but the trend of the power-law slope stands out: it is possible to see clearly how it increases with the frequency.

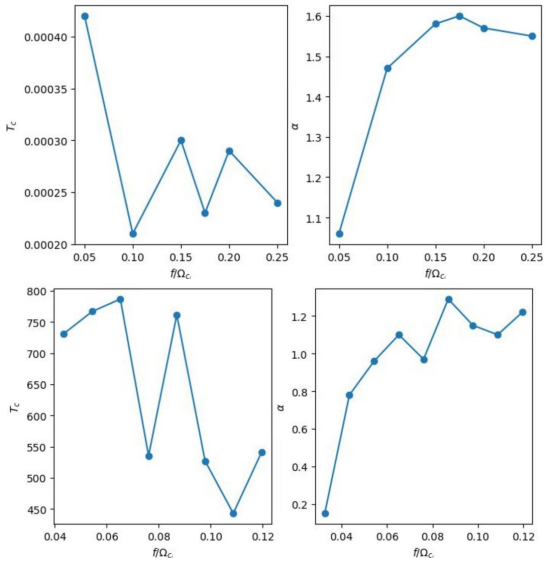

Figure 4.27: Variation of the coefficients of the fits of the waiting times distribution with the frequency in the case of TPE (above) and RFX (below): cut-off exponent (left) and power law slope (right).

4.3.4 Correlation with the reversal parameter

In order to further study the correlation among all the involved phenomena, the reversal parameter F (definition 2.30) measured by TPE-1RM20 was introduced in the analysis. The intermittent structures detected by the LIM were plotted again to see how they dislocate in time with respect to the trace of the F parameter. In fact, as mentioned in paragraph §3.2, a minimum in its time trace indicates a decrease in the toroidal component of the magnetic field at the edge plasma region, which is one of the subsequent phases characterizing magnetic reconnection. In this case, the analysis was limited to single shots and not multiple signals, and it was carried out for different sampling frequencies (again 50, 100, and 150 kHz). Only the high theta shots were considered because the variation of the flux is more significant and the events result to be more important at high values of theta. Figure 4.28 gives an example of the detected maxima, which are identified on the time series of the F parameter as vertical dashed lines. In particular, clusters of the detected intermittent structures are expected close to the minima of the F fluctuations: more exactly in the decreasing phases, and this is in agreement with what is seen in figure 4.28. However, we can also observe that some structures are detected in the regions where the signal increases: this makes sense because it may indicate the reconnection event occurring after the current discharge (i.e. the peak in the electron current).

In the end, the aim was to quantify the number of intermittent structures in a shot by looking at how their average frequency (namely the frequency of the time delay between the peaks) changes or rather increases when there is the minimum of the reconnection event (corresponding to a minimum in the F parameter). Working with different sampling frequencies, it is possible to notice any difference in the characteristic scales, and infer if some coherent structures are privileged at a precise location. In order to get this information, the waiting times were used: by plotting them with respect to the F parameter it is possible to see if min-

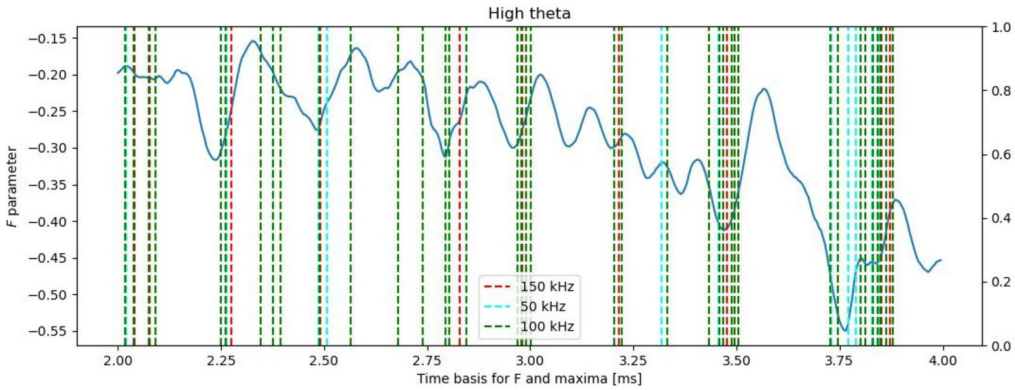

Figure 4.28: Time trace of the adimentional reversal parameter F 2.30 on which the detected maxima are plotted as vertical dashed lines at 50, 100, and 150 kHz. This is a high theta shot. The F parameter trace and the maxima array share the same time basis on axis x.

imum values of the waiting times, that is, maximum values of the frequency of occurrence of the reconnection events, correspond (in time) to minima of the F fluctuations. A first attempt was to plot together the waiting times and the F parameter creating a fictitious time array for the waiting times which corresponds to the time intervals between two consecutive detected maxima, but by eye it was hard to discriminate if the two signals were in phase. Therefore, the cross correlation method was used which measures the similarity between two time series as a function of the relative displacement between them. The function *numpy.correlate* returns the values of the correlation parameter

$$R_{ij} = \frac{C_{ij}}{\sqrt{C_{ii}C_{jj}}}$$

with C being the covariance matrix, as a function of the time lag, i.e., the number of periods separating the two series, shifting one signal with respect to the other. The time basis is fictitious and centered in zero, and the correlation coefficients are normalized such that they run from -1 to +1, where the negative values indicate an anti-correlation, whereas a relevant correlation exhibits positive enough values. In order to make this operation, the two functions to be correlated need to have the same time basis, thus an interpolation was made on F. The expected result is a bell-shaped function and the characteristic time can be inferred from the distance which covers the decreasing and increasing region with respect to the central peak. The output is an array with double dimension with respect to the initial time basis. We can plot this function for different cases to see if there is a dependence on the characteristic frequency. The presence of a clear peak is a confirmation of the existence of a correlation between the two quantities. These statistics were applied to arbitrary shots contained in all the available kinds of datasets, but only the relevant results are reported. The first example is given in figure 4.29 by a shot at high current where the correlation even exceeds 0.7 in correspondence of the peak at 50 and 100 kHz. The correlation is found also at high theta in figure 4.30 where the peak is clear enough at all frequencies. Different is the situation at high density and in the case of the "ground" dataset, for whom a well defined peak was not observed at 50 kHz. Therefore, in figures 4.31 and 4.32 only the results at 100 and 150 kHz are shown.

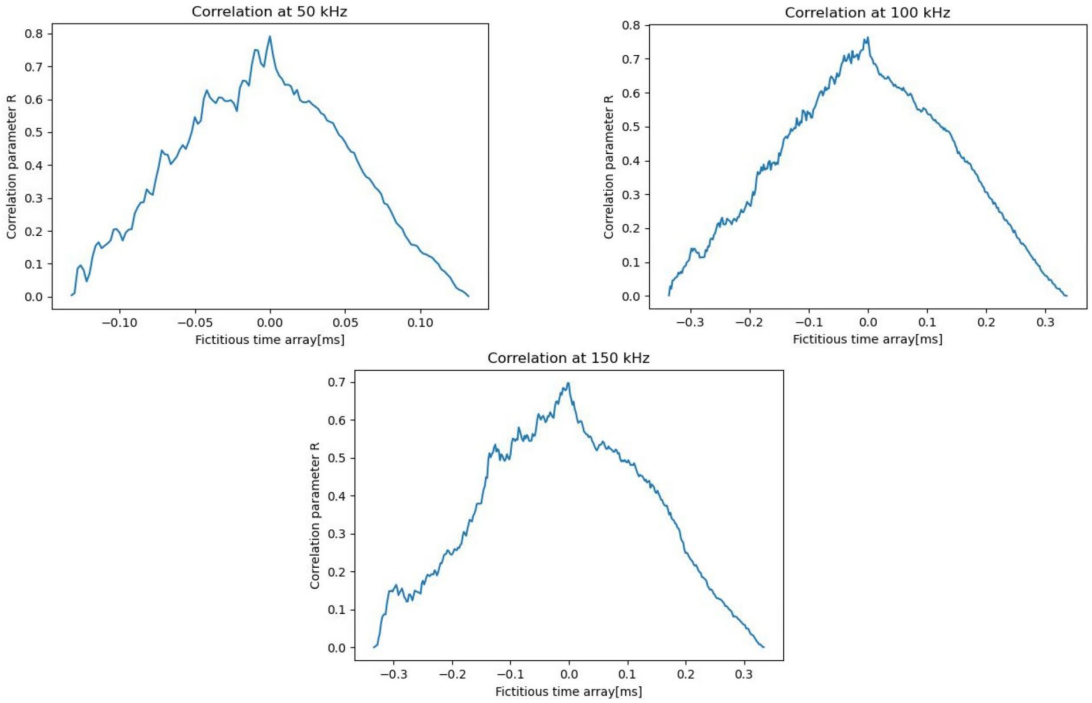

Figure 4.29: Results obtained after the cross correlation between the reversal parameter F and the frequency of the intermittent events corresponding to the inverse of the waiting times. This is a single arbitrary shot at high current.

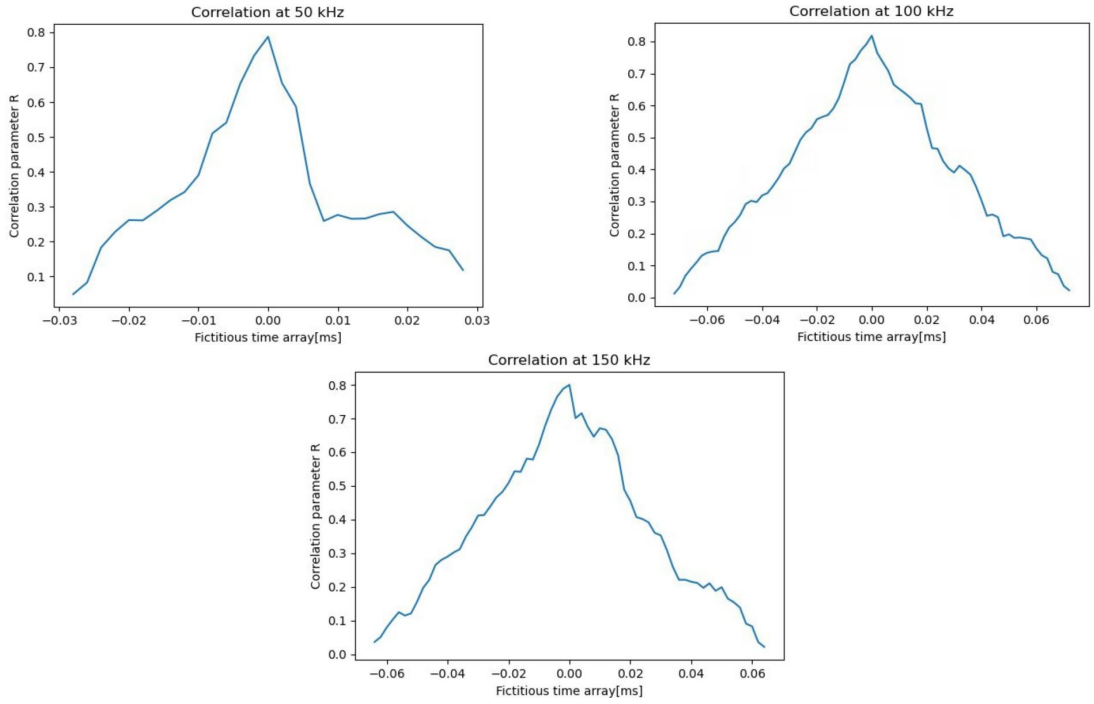

Figure 4.30: Results obtained after the cross correlation between the reversal parameter F and the frequency of the intermittent events corresponding to the inverse of the waiting times. This is a single arbitrary shot at high theta.

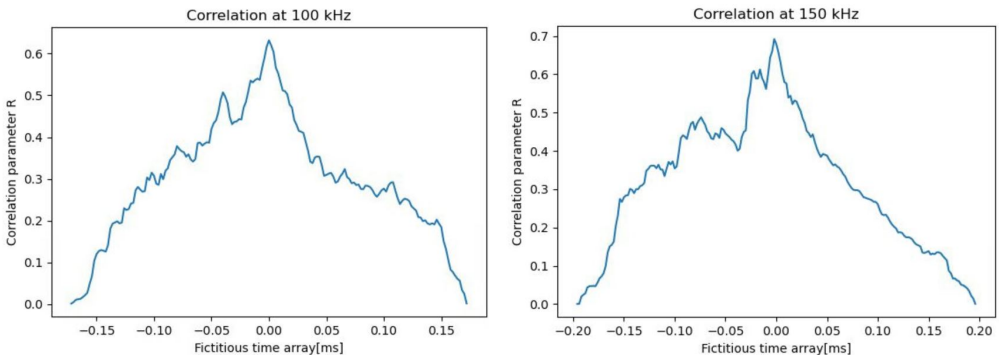

Figure 4.31: Results obtained after the cross correlation between the reversal parameter F and the frequency of the intermittent events corresponding to the inverse of the waiting times. These are arbitrary shots at high density. Only the relevant results (at 100 and 150 kHz) are reported.

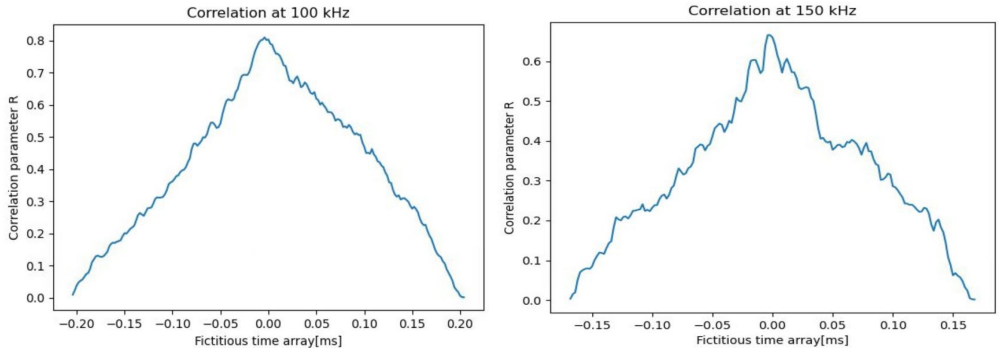

Figure 4.32: Results obtained after the cross correlation between the reversal parameter F and the frequency of the intermittent events corresponding to the inverse of the waiting times. These are arbitrary shots of the "ground" dataset. Only the relevant results (at 100 and 150 kHz) are reported.

In conclusion, we can confirm that a correlation exists between the inverse of the waiting times and the reversal parameter which means that the frequency of the turbulent events increases when there is the minimum of the F parameter, namely, during the reconnection events.

4.4 Results

Hereafter a brief summary follows of the principal results achieved with the data analysis. First, it has been proved that the signal of the electron current (measured by the EEA of TPE-1RM20) and magnetic field present an intermittent nature, since bursting events have been detected (fig. 4.7), and their typical effect on the PDFs has been observed (fig. 4.8), which exhibit larger deviations from the gaussian distribution and enhanced tails at higher frequency. The bursting events result on the signals of TPE as a peak in the electron current and a rapid variation in the electron potential revealing the presence of fast electrons (fig. 4.16, 4.17, 4.18, 4.19), and, on the other hand, they are associated to parallel currents measured by RFX (fig. 4.20). In particular, both electron current and parallel current are associated with magnetic fluctuations presenting the typical phase quadrature relation between radial and toroidal field consistent with current sheet structures (fig. 4.13) and closed orbits in the hodogram (fig. 4.14, 4.15). The distribution of the waiting times follows a power-law (plus an exponential cut-off) with respect to the frequency (fig. 4.25), meaning that the process is time-correlated and self-similar. In particular, the power-law slope clearly increases with the frequency (fig. 4.27). Moreover, the waiting times distribution is highly correlated with the time evolution of the reversal parameter, indicating the generation of the macroscopic toroidal flux accompanied by the decrease in the edge of the toroidal magnetic field, typical phenomena occurring during magnetic reconnection.

In conclusion, the effects of magnetic reconnection on RFP plasmas have been revealed: it causes the formation of current structures associated to the formation of a population of fast electrons and an intense MHD activity observed in the boundary region, making the spectrum turbulent and intermittent.

Chapter 5

Conclusion

In this thesis the burst phenomena associated to electron accelerations occurring in turbulent magnetized plasmas have been investigated, with particular focus on their relation to magnetic reconnection. Many examples of astrophysical plasmas where these processes occur have been proposed (see §3.1), but the environment in which such hypotheses have been tested during this work is laboratory plasmas in the Reversed Field Pinch configuration. For this aim, a review has been first provided of the principal concepts regarding the theory of magnetohydrodynamics (§2.1.1), magnetic confinement of fusion-oriented toroidal plasmas (§2.1.2), and magnetic reconnection (§2.2), which has been identified as the cause for particle acceleration. Successively, an overview about turbulence in MHD flows has been presented (§3.2), in order to offer all the necessary background to understand the tools used in the data analysis, mainly wavelet transforms, Probability Distribution Function of the fluctuations, and Local Intermittency Measurement method. Finally, the diagnostics of the devices used to collect the data for the analysis has been described in §4.1.

The data analysis provided satisfying results. The enhanced tails in the PDFs (figure 4.8) revealed the intermittent nature of the acceleration events identified as non-gaussian fluctuations, while the Power Spectral Density unveiled the impact of an intense MHD activity on the spectrum at lower frequency (see figure 4.6), which can also impact our understanding of the dynamics at smaller timescales. As can be observed in figure 4.28, the events are correlated in time with the variations in the reversal parameter describing the phases of a reconnection process. Figures 4.16, 4.17, 4.18, 4.19 and 4.20 confirm that the peak in both electron acceleration and parallel current is associated to magnetic fluctuations, which exhibit features attributable to current sheet structures, in addition to a specific pattern in the floating potential showing the electric field variation. For all these reasons, it can be concluded that actually there exists a correlation between electron accelerations causing the observed bursting events and magnetic reconnection in magnetized plasmas affected by turbulence.

However, the investigation does not end here, since subsequent developments from a numerical point of view are planned: it is possible to numerically simulate a plasma characterized by conditions similar to those of toroidal RFP plasmas on which this analysis has been conducted. Such a model could include the presence of current sheets in the MHD regime, in order to verify what kind of influence they exert on acceleration mechanisms. In the end, the findings could be applicable even to astrophysical plasmas. This will be part of a future work.

Furthermore, the issue of the correlation between fast electrons and magnetic reconnection will also be addressed in another experiment, RFX-mod2, which will be started again in 2025, in collaboration with a group of researchers of the Mullard Space Science Laboratory (UCL). The device will be adapted with the aim of building new diagnostics to determine and study the distribution function of electrons and ions which could offer more detailed information about the acceleration processes and their relation to reconnection.

In conclusion, there is still a lot of uncertainty about the fundamental and frequent acceleration processes occurring both in laboratory and astrophysical plasmas, which can make the particles reach very high energies, leading to important consequences on the environment they are part of. Moreover, such studies acquire a much more general relevance when considering that they could provide us with useful insights into processes, like magnetic reconnection, occurring in all the diverse kinds of magnetic fields permeating our universe, unveiling the complexity of the underlying physics.

Bibliography

[1] A Achterberg and CA Norman. Particle acceleration by shock waves in solar flares. *Astronomy and Astrophysics, vol. 89, no. 3, Sept. 1980, p. 353-362. Research supported by the Nederlandse Organisatie voor Zuiver-Wetenschappelijk Onderzoek.*, 89:353–362, 1980.

[2] AF Almagri, S Assadi, SC Prager, JS Sarff, and DW Kerst. Locked modes and magnetic field errors in the madison symmetric torus. *Physics of Fluids B: Plasma Physics*, 4(12):4080–4085, 1992.

[3] V Antoni, Vincenzo Carbone, E Martines, G Regnoli, G Serianni, N Vianello, and Pierluigi Veltri. Electrostatic turbulence intermittency and mhd relaxation phenomena in a rfp plasma. *Europhysics Letters*, 54(1):51, 2001.

[4] Joachim Birn, John T Gosling, Michael Hesse, Terry G Forbes, and Eric R Priest. Simulations of three-dimensional reconnection in the solar corona. *The Astrophysical Journal*, 541(2):1078, 2000.

[5] Dieter Biskamp. Magnetic reconnection. *Physics Reports*, 237(4):179–247, 1994.

[6] Dieter Biskamp and Dieter Biskamp. *Nonlinear magnetohydrodynamics*. Number 1. Cambridge University Press, 1997.

[7] S Cappello and D Biskamp. Reconnection processes and scaling laws in reversed field pinch magnetohydrodynamics. *Nuclear Fusion*, 36(5):571, 1996.

[8] S Cappello and DF Escande. Bifurcation in viscoresistive mhd: The hartmann number and the reversed field pinch. *Physical review letters*, 85(18):3838, 2000.

[9] Vincenzo Carbone, L Sorriso-Valvo, E Martines, V Antoni, and Pierluigi Veltri. Intermittency and turbulence in a magnetically confined fusion plasma. *Physical Review E*, 62(1):R49, 2000.

[10] Giovanni Carraro. *Astrophysics of the Interstellar Medium*. Springer International Publishing, 2021.

[11] B Castaing, Y Gagne, and EJ Hopfinger. Velocity probability density functions of high reynolds number turbulence. *Physica D: Nonlinear Phenomena*, 46(2):177–200, 1990.

[12] H Che, JF Drake, and M Swisdak. A current filamentation mechanism for breaking magnetic field lines during reconnection. *Nature*, 474(7350):184–187, 2011.

[13] Bin Chen, Timothy S Bastian, Chengcai Shen, Dale E Gary, Säm Krucker, and Lindsay Glesener. Particle acceleration by a solar flare termination shock. *Science*, 350(6265):1238–1242, 2015.

[14] Arnab Rai Choudhuri. *The physics of fluids and plasmas: an introduction for astrophysicists*. Cambridge University Press, 1998.

[15] RM Close, Clare Elizabeth Parnell, DW Longcope, and Eric Ronald Priest. Recycling of the solar corona's magnetic field. *The Astrophysical Journal*, 612(1):L81, 2004.

[16] JW Connor and RJ Hastie. Relativistic limitations on runaway electrons. *Nuclear fusion*, 15(3):415, 1975.

[17] B De Pontieu, SW McIntosh, M Carlsson, VH Hansteen, TD Tarbell, CJ Schrijver, AM Title, RA Shine, S Tsuneta, Y Katsukawa, et al. Chromospheric alfvénic waves strong enough to power the solar wind. *science*, 318(5856):1574–1577, 2007.

[18] DJ Den Hartog, J-W Ahn, AF Almagri, JK Anderson, AD Beklemishev, AP Blair, F Bonomo, MT Borchardt, DL Brower, DR Burke, et al. Recent improvements in confinement and beta in the mst reversed-field pinch. *Nuclear fusion*, 47(9):L17, 2007.

[19] WX Ding, V Mirnov, A Almagri, DL Brower, D Craig, BH Deng, D Den Hartog, G Fiksel, C Hegna, S Prager, et al. Hall dynamo and plasma relaxation in mst reversed field pinch. In *APS Division of Plasma Physics Meeting Abstracts*, volume 46, pages NP1–055, 2004.

[20] M Dobrowolny, A Mangeney, and Pierluigi Veltri. Fully developed anisotropic hydromagnetic turbulence in interplanetary space. *Physical Review Letters*, 45(2):144, 1980.

[21] Ami M DuBois, Abdulgader F Almagri, Jay K Anderson, Daniel J Den Hartog, John David Lee, and John S Sarff. Anisotropic electron tail generation during tearing mode magnetic reconnection. *Physical Review Letters*, 118(7):075001, 2017.

[22] Jan Egedal, W Daughton, and A Le. Large-scale electron acceleration by parallel electric fields during magnetic reconnection. *Nature Physics*, 8(4):321–324, 2012.

[23] Walter M Elsasser. The hydromagnetic equations. *Physical Review*, 79(1):183, 1950.

[24] WC Feldman, B Abraham-Shrauner, JR Asbridge, and SJ Bame. The internal plasma state of the high speed solar wind at 1 au. *Physics of Solar Planetary Environments*, 1:413, 1976.

[25] Timothy P Fleming, James M Stone, and John F Hawley. The effect of resistivity on the nonlinear stage of the magnetorotational instability in accretion disks. *The Astrophysical Journal*, 530(1):464, 2000.

[26] Federico Fraternale, Nikolai V Pogorelov, and Leonard F Burlaga. Signatures of intermittency and fine-scale turbulence in the very local interstellar medium. *The Astrophysical Journal Letters*, 897(2):L28, 2020.

[27] Jeffrey P Freidberg. *Ideal magnetohydrodynamics*. Plenum Press, New York, NY, 1987.

[28] Jeremy Goodman and Guohong Xu. Parasitic instabilities in magnetized, differentially rotating disks. *Astrophysical Journal, Part 1 (ISSN 0004-637X), vol. 432, no. 1, p. 213-223*, 432:213–223, 1994.

[29] Gunnar Hedin. Mhd behaviour in a resistive-shell reversed-field pinch. *Plasma physics and controlled fusion*, 40(8):1529, 1998.

[30] S Hokin, A Almagri, S Assadi, J Beckstead, G Chartas, N Crocker, M Cudzinovic, D Den Hartog, R Dexter, D Holly, et al. Global confinement and discrete dynamo activity in the mst reversed-field pinch. *Physics of Fluids B: Plasma Physics*, 3(8):2241–2246, 1991.

[31] JC Ingraham, RF Ellis, JN Downing, CP Munson, PG Weber, and GA Wurden. Energetic electron measurements in the edge of a reversed-field pinch. *Physics of Fluids B: Plasma Physics*, 2(1):143–159, 1990.

[32] Abram R Jacobson and Ronald W Moses. Nonlocal dc electrical conductivity of a lorentz plasma in a stochastic magnetic field. *Physical Review A*, 29(6):3335, 1984.

[33] H Ji, AF Almagri, SC Prager, and JS Sarff. Time-resolved observation of discrete and continuous magnetohydrodynamic dynamo in the reversed-field pinch edge. *Physical review letters*, 73(5):668, 1994.

[34] Frank C Jones and Donald C Ellison. The plasma physics of shock acceleration. *Space Science Reviews*, 58(1):259–346, 1991.

[35] Boris B Kadomtsev. Disruptive instability in tokamaks. *Fizika plazmy*, 1:710–715, 1975.

[36] Margaret G Kivelson and Christopher T Russell. *Introduction to space physics*. Cambridge university press, 1995.

[37] Frederike Kneer, Eckehard Schöll, and Markus Dahlem. Nucleation of reaction-diffusion waves on curved surfaces. *New Journal of Physics*, 16:053010, 05 2014.

[38] Andreĭ Nikolaevich Kolmogorov. *Turbulence: the legacy of AN Kolmogorov*. Cambridge university press, 1995.

[39] Andrey Nikolaevich Kolmogorov. The local structure of turbulence in incompressible viscous fluid for very large reynolds. *Numbers. In Dokl. Akad. Nauk SSSR*, 30:301, 1941.

[40] Säm Krucker, GJ Hurford, and RP Lin. Hard x-ray source motions in the 2002 july 23 gamma-ray flare. *The Astrophysical Journal*, 595(2):L103, 2003.

[41] Fabio Lepreti, Vincenzo Carbone, and Pierluigi Veltri. Solar flare waiting time distribution: varying-rate poisson or lévy function? *The Astrophysical Journal*, 555(2):L133, 2001.

[42] Marcel Lesieur. *Turbulence in fluids: stochastic and numerical modelling*, volume 488. Nijhoff Boston, MA, 1987.

[43] David Clement Leslie. Developments in the theory of turbulence. *(No Title)*, 1973.

[44] FM Levinton, Steven H Batha, M Yamada, and MC Zarnstorff. q-profile measurements in the tokamak fusion test reactor. *Physics of Fluids B: Plasma Physics*, 5(7):2554–2561, 1993.

[45] Paulett C Liewer. Measurements of microturbulence in tokamaks and comparisons with theories of turbulence and anomalous transport. *Nuclear Fusion*, 25(5):543, 1985.

[46] J Lin, TG Forbes, ER Priest, and TN Bungey. Models for the motions of flare loops and ribbons. *Solar Physics*, 159:275–299, 1995.

[47] R Lorenzini, Matteo Agostini, A Alfier, V Antoni, L Apolloni, F Auriemma, O Barana, M Baruzzo, Paolo Bettini, D Bonfiglio, et al. Improvement of the magnetic configuration in the reversed field pinch through successive bifurcations. *Physics of Plasmas*, 16(5), 2009.

[48] R Lorenzini, D Terranova, A Alfier, P Innocente, E Martines, R Pasqualotto, and P Zanca. Single-helical-axis states in reversed-field-pinch plasmas. *Physical review letters*, 101(2):025005, 2008.

[49] Quanming Lu, Lican Shan, Chenlong Shen, Tielong Zhang, Yiren Li, and Shui Wang. Velocity distributions of superthermal electrons fitted with a power law function in the magnetosheath: Cluster observations. *Journal of Geophysical Research: Space Physics*, 116(A3), 2011.

[50] RL Mace and MA Hellberg. A dispersion function for plasmas containing superthermal particles. *Physics of Plasmas*, 2(6):2098–2109, 1995.

[51] N Magyar, T Van Doorsselaere, and M Goossens. The nature of elsässer variables in compressible mhd. *The Astrophysical Journal*, 873(1):56, 2019.

[52] Raffaele Marino and Luca Sorriso-Valvo. Scaling laws for the energy transfer in space plasma turbulence. *Physics Reports*, 1006:1–144, 2023.

[53] S Masuda, T Kosugi, H Hara, S Tsuneta, and Y Ogawara. A loop-top hard x-ray source in a compact solar flare as evidence for magnetic reconnection. *Nature*, 371(6497):495–497, 1994.

[54] Willam H Matthaeus, Minping Wan, Sergio Servidio, Antonella Greco, Kareem T Osman, Sean Oughton, and Pablo Dmitruk. Intermittency, nonlinear dynamics and dissipation in the solar wind and astrophysical plasmas. *Philosophical Transactions of the Royal Society A: Mathematical, Physical and Engineering Sciences*, 373(2041):20140154, 2015.

[55] FC Michel. Coherent neutral sheet radiation from pulsars. *Comments on Astrophysics and Space Physics, Vol. 3, p. 80*, 3:80, 1971.

[56] B Momo, H Isliker, R Cavazzana, M Zuin, L Cordaro, D Lopez-Bruna, E Martines, I Predebon, C Rea, M Spolaore, et al. The phenomenology of reconnection events in the reversed field pinch. *Nuclear Fusion*, 60(5):056023, 2020.

[57] PA Muñoz and Jörg Büchner. Kinetic turbulence in fast three-dimensional collisionless guide-field magnetic reconnection. *Physical Review E*, 98(4):043205, 2018.

[58] RA Nebel, EJ Caramana, and DD Schnack. The role of m= 0 modal components in the reversed-field-pinch dynamo effect in the single fluid magnetohydrodynamics model. *Physics of Fluids B: Plasma Physics*, 1(8):1671–1674, 1989.

[59] Miguel Onorato, Roberto Camussi, and Gaetano Iuso. Small scale intermittency and bursting in a turbulent channel flow. *Physical Review E*, 61(2):1447, 2000.

[60] S Ortolani. Reversed field pinch confinement physics. *Plasma Physics and Controlled Fusion*, 31(10):1665, 1989.

[61] EN Parker. Acceleration of cosmic rays in solar flares. *Physical Review*, 107(3):830, 1957.

[62] Eugene N Parker. The solar-flare phenomenon and the theory of reconnection and annihiliation of magnetic fields. *Astrophysical Journal Supplement, vol. 8, p. 177 (1963)*, 8:177, 1963.

[63] Harry E Petschek. 50 magnetic field annihilation. *NASA SP.*, (50):425, 1964.

[64] G Regnoli, N Vianello, Y Yagi, E Martines, G Serianni, V Antoni, et al. Fast electrons and intermittent events in the rfp device tpe-1rm20. In *Proceedings of the 31st EPS Conference on Plasma Physics*, volume 28, pages 1–4, 2004.

[65] Alessandro Retinò, Yuri Khotyaintsev, Olivier Le Contel, Maria Federica Marcucci, Ferdinand Plaschke, Andris Vaivads, Vassilis Angelopoulos, Pasquale Blasi, Jim Burch, Johan De Keyser, et al. Particle energization in space plasmas: towards a multi-point, multi-scale plasma observatory. *Experimental Astronomy*, pages 1–45, 2021.

[66] MM Romanova, GV Ustyugova, AV Koldoba, VM Chechetkin, and RVE Lovelace. Dynamics of magnetic loops in the coronae of accretion disks. *The Astrophysical Journal*, 500(2):703, 1998.

[67] MN Rosenbluth, RZ Sagdeev, JB Taylor, and GM Zaslavski. Destruction of magnetic surfaces by magnetic field irregularities. *Nuclear Fusion*, 6(4):297, 1966.

[68] K Schindler, M Hesse, and J Birn. General magnetic reconnection, parallel electric fields, and helicity. *Journal of Geophysical Research: Space Physics*, 93(A6):5547–5557, 1988.

[69] DD Schnack, EJ Caramana, and RA Nebel. Three-dimensional magnetohydrodynamic studies of the reversed-field pinch. *The Physics of fluids*, 28(1):321–333, 1985.

[70] W Shen and JC Sprott. Modified polynomial function model for reversed-field pinches. *Physics of Fluids B: Plasma Physics*, 3(5):1225–1231, 1991.

[71] P Simon, M Ramisch, AA Beletskii, A Dinklage, M Endler, S Marsen, B Nold, U Stroth, P Tamain, and R Wilcox. Scaling and transport analyses based on an international edge turbulence database. *Plasma Physics and Controlled Fusion*, 56(9):095015, 2014.

[72] Sisworo Sisworo. On holder exponents. *Matematika & Sains*, 4:244–249, 01 1999.

[73] H Soltwisch. Measurement of current-density changes during sawtooth activity in a tokamak by far-infrared polarimetry. *Review of Scientific Instruments*, 59(8):1599–1604, 1988.

[74] Adam Stahl, Eero Hirvijoki, Joan Decker, Ola Embréus, and Tünde Fülöp. Effective critical electric field for runaway-electron generation. *Physical Review Letters*, 114(11):115002, 2015.

[75] MR Stoneking, SA Hokin, Stewart C Prager, G Fiksel, Hantao Ji, and DJ Den Hartog. Particle transport due to magnetic fluctuations. *Physical review letters*, 73(4):549, 1994.

[76] SI Syrovatskii. Formation of current sheets in a plasma with a frozen-in strong magnetic field. *Sov. phys. JETP*, 33(5):933–940, 1971.

[77] I Teliban, D Block, A Piel, and F Greiner. Improved conditional averaging technique for plasma fluctuation diagnostics. *Plasma Physics and Controlled Fusion*, 49(4):485, 2007.

[78] Saku Tsuneta. Structure and dynamics of magnetic reconnection in a solar flare. *Astrophysical Journal v. 456, p. 840*, 456:840, 1996.

[79] Vytenis M Vasyliunas. Theoretical models of magnetic field line merging. *Reviews of Geophysics*, 13(1):303–336, 1975.

[80] N Vianello, V Naulin, R Schrittwieser, HW Müller, M Zuin, C Ionita, JJ Rasmussen, F Mehlmann, V Rohde, R Cavazzana, et al. Direct observation of current in type-i edge-localized-mode filaments on the asdex upgrade tokamak. *Physical review letters*, 106(12):125002, 2011.

[81] N Vianello, M Spolaore, M Agostini, R Cavazzana, G De Masi, E Martines, B Momo, P Scarin, S Spagnolo, and M Zuin. On the statistics and features of turbulent structures in rfx-mod. *Plasma Physics and Controlled Fusion*, 58(4):044009, 2016.

[82] Nicola Vianello. *Fenomeni di auto organizzazione e generazione di strutture coerenti indotte da turbolenza elettrostatica in plasmi magnetizzati*. PhD thesis, Università degli studi di Padova, 2002.

[83] John Wesson and D. J. Campbell. *Tokamaks*. OUP Oxford, 2011.

[84] Y Yagi, V Antoni, M Bagatin, Daniele Desideri, E Martines, G Serianni, and F Vallone. Measurement of superthermal electron flow and temperature in a reversed-field pinch experiment by an electrostatic electron energy analyser. *Plasma physics and controlled fusion*, 39(11):1915, 1997.

[85] Y Yagi, Y Maejima, Y Hirano, T Shimada, I Hirota, S Sekine, H Sakakita, and H Koguchi. Characteristics of global confinement properties in tpe-series reversed-field pinch devices. *Nuclear fusion*, 43(12):1787, 2003.

[86] Yasuyuki Yagi, Yoichi Hirano, Toshio Shimada Toshio Shimada, and Yoshiki Maejima Yoshiki Maejima. Measurement of fast electron velocity distribution function in a reversed field pinch plasma. *Japanese journal of applied physics*, 35(7R):4064, 1996.

[87] Yasuyuki Yagi, Gianluigi Serianni, Hantao Ji, and Yoshiki Maejima. Correlation studies on fast electrons and dynamo-related activities in a reversed-field pinch plasma. *Japanese journal of applied physics*, 38(7R):4213, 1999.

[88] Masaaki Yamada, Hantao Ji, Scott Hsu, Troy Carter, Russell Kulsrud, Norton Bretz, Forrest Jobes, Yasushi Ono, and Francis Perkins. Study of driven magnetic reconnection in a laboratory plasma. *Physics of Plasmas*, 4(5):1936–1944, 1997.

[89] Masaaki Yamada, Russell Kulsrud, and Hantao Ji. Magnetic reconnection. *Reviews of modern physics*, 82(1):603, 2010.

[90] Masaaki Yamada, Yang Ren, Hantao Ji, Joshua Breslau, Stefan Gerhardt, Russell Kulsrud, and Aleksey Kuritsyn. Experimental study of two-fluid effects on magnetic reconnection in a laboratory plasma with variable collisionality. *Physics of Plasmas*, 13(5), 2006.

[91] Z Yoshida, A Hasegawa, and M Wakatani. Production of superthermal electrons and ion cyclotron waves in a reversed-field-pinch plasma. *Physics of Fluids B: Plasma Physics*, 5(9):3261–3266, 1993.

[92] M Zuin, N Vianello, M Spolaore, V Antoni, T Bolzonella, R Cavazzana, E Martines, G Serianni, and D Terranova. Current sheets during spontaneous reconnection in a current-carrying fusion plasma. *Plasma Physics and Controlled Fusion*, 51(3):035012, 2009.

[93] Ellen G Zweibel and Axel Brandenburg. Current sheet formation in the interstellar medium. *The Astrophysical Journal*, 478(2):563, 1997.